UNIVERSIDAD NACIONAL AUTÓNOMA DE MÉXICO

LICENCIATURA EN CIENCIA DE MATERIALES SUSTENTABLES

Escuela Nacional de Estudios Superiores,
Unidad Morelia

DESARROLLO DE TRANSISTORES HÍBRIDOS ORGÁNICO-INORGÁNICOS PARA LA DETECCIÓN DE GLIFOSATO

T E S I S

QUE PARA OBTENER EL TÍTULO DE

LICENCIADA EN CIENCIA DE CIENCIA DE MATERIALES SUSTENTABLES

P R E S E N T A

PAULINA ABRIL VILLAGÓMEZ MONDRAGÓN

DIRECTORA DE TESIS: DRA. ALEJANDRA CASTRO CARRANZA

MORELIA, MICHOACÁN, MÉXICO **OCTUBRE, 2022**

UNIVERSIDAD NACIONAL AUTÓNOMA DE MÉXICO

LICENCIATURA EN CIENCIA DE MATERIALES SUSTENTABLES

Escuela Nacional de Estudios Superiores,
Unidad Morelia

DESARROLLO DE TRANSISTORES HÍBRIDOS ORGÁNICO-INORGÁNICOS PARA LA DETECCIÓN DE GLIFOSATO

T E S I S

QUE PARA OBTENER EL TÍTULO DE

LICENCIADA EN CIENCIA DE CIENCIA DE MATERIALES SUSTENTABLES

P R E S E N T A

PAULINA ABRIL VILLAGÓMEZ MONDRAGÓN

DIRECTORA DE TESIS: DRA. ALEJANDRA CASTRO CARRANZA

MORELIA, MICHOACÁN, MÉXICO **OCTUBRE, 2022**

MTRA. IVONNE RAMÍREZ WENCE
DIRECTORA
DIRECCIÓN GENERAL DE ADMINISTRACIÓN ESCOLAR
P R E S E N T E

Por medio de la presente me permito informar a usted que en la **sesión ordinaria 04** del **H. Consejo Técnico** de la Escuela Nacional de Estudios Superiores (ENES) Unidad Morelia celebrada el día **23 de febrero de 2022**, acordó poner a su consideración el siguiente jurado para la presentación del Trabajo Profesional de la alumna **Paulina Abril Villagómez Mondragón** adscrita a la Licenciatura en **Ciencia de Materiales Sustentables** con número de cuenta **418125874,** quien presenta el trabajo titulado: **"Desarrollo de transistores híbridos orgánico-inorgánicos para la detección de glisofato"** bajo la dirección como **tutora** de la **Dra. Alejandra Castro Carranza.**

El jurado queda integrado de la siguiente manera:

Presidente:	Dr. Orlando Hernández Cristóbal
Vocal:	Prof. Dr. Lucio Colombi Ciacchi
Secretario:	Dra. Alejandra Castro Carranza
Suplente 1:	Prof. Dr. Jürgen Gutowski
Suplente 2:	Dra. Susan Köppen

Sin otro particular, quedo de usted.

A t e n t a m e n t e
"POR MI RAZA HABLARA EL ESPIRITU"
Morelia, Michoacán a 24 de agosto de 2022.

DRA. YUNUEN TAPIA TORRES
SECRETARIA GENERAL

Institutional acknowledgements

I would like to thank the *Univesidad Nacional Autónoma de México (UNAM)*, the *Escuela Nacional de Estudios Superiores Unidad Morelia (ENES-Morelia),* and the *Ciencia de Materiales Sustentables* bachelor program for the opportunity to be part of this institution.

It is acknowledged the funding support received through the following projects and institutions through which the development of this research was possible:

- *Programa de Apoyo a Proyectos de Investigación e Innovación Tecnológica* (PAPIIT-UNAM), project **TA101221** "*Puesta en marcha del proceso de fabricación de sensores ambientales de bajo costos basados en transistores (TFTs) de óxidos semiconductores para la detección de contaminantes en agua y aire en la región de Morelia*",
- *Programa de Apoyo a Proyectos para Innovar y Mejorar la Educación* (PAPIME-UNAM), project **PE109421** *"Educación a distancia en ciencias aplicadas en el área de nanotecnología y ciencias atmosféricas: desarrollo de un programa híbrido internacional ENES Morelia UNAM - Universidad de Bremen*". 2021,
- *Consejo Nacional de Ciencia y Tecnología* (CONACYT) for funding through the **CF19-263955** Frontier Science project "Study of the electronic interaction between toxic molecules in the environment with organic semiconductors and oxides for the design of food, air and water sustainable sensors",
- *Laboratorio Nacional de Computo de Alto Desempeño (**LANCAD-UNAM-DGTIC-420**)* for funding the *"Simulaciones de dinámica molecular de la interración entre agroquímicos tóxicos y semiconductores para el diseño de sensores sustentables*" project, March-December 2020.
- German Academic Exchange Service (DAAD-IVAC): "Digital Teaching in Atmospheric Sciences and Nanotechnology, Germany (2020-2022),
- *Dirección General de Cooperación e Internacionalización (UNAM-DGECI)* for granting me with the *"Iniciación a la investigación Verano-otoño 2021"* scholarship, and the
- DAAD organization for funding my academic research stay at the University of Bremen, since it allowed me to generate results presented in this work.

I want to express my gratitude to Dr. Alejandra Castro Carranza, head of the International Laboratory for Environmental Electronic Devices (LAIDEA-UNAM), for this work's supervision and direction. Major thanks for contacting me in the scientific environment and managing my research stay abroad.

I thank Ph.D. candidate Maria von Einem and B.Sc. Andrés Castro Chacón for their contributions, discussions and effort put into developing this project.

I thank Prof. J. Gutowski and Prof. G. Callsen for hosting my research stay at the Semiconductor Optics Research Group, Institute of Solid-State Physics, University of Bremen. I would also thank Dr. Wilken Seemann, a member of this group, since his master´s thesis work was fundamental for the development of this research.

I thank Prof. L. Colombi and Dr. Susan Köppen from the Hybrid Material Interfaces group, University of Bremen, for hosting me in the HMI group and providing me with the necessary computational resources. Furthermore, I thank Ph.D. candidate Eric Macke, for his support and willingness to help me when facing technical problems.

I want to thank Dr. Filippo Balzaretti for his doctoral thesis work, which was an essential antecedent for this research.

I thank Dr. Orlando Hernández from the *Laboratorio de Microscopia* (LaMic-ENES Morelia) for his support in facilitating the use of the SEM characterization equipment. Furthermore, I thank B.Sc. Pablo Vega for his help in generating the SEM micrographs presented in this work.

I thank Lic. Agustín Martínez Morales and Lic. Alejandro Rebollar from the *Departamento de Servicios Escolares*, ENES Morelia for their attention during my graduation process.

Finally, I thank all the members of my committee: Dr. Orlando Hernández Cristóbal, Prof. Dr. Jürgen Gutowski, Prof. Dr. Lucio Colombi Ciacchi, Dr. Susan Köppen and Dr. Alejandra Castro Carranza for their support, feedback, and discussion.

Personal acknowledgements

Firstly, I would like to thank Dr. Alejandra Castro Carranza for pushing me to do my best in every challenge in life. For her guidance, advice, and support during this journey. And, for showing me, together with Dr. Jairo Nolasco, the amazing world of science.

I want to thank Maria von Einem for her infinite patience with me and this project. I was looking for glyphosate adsorption on ZnO, and I found an amazing friend. *¡Muchas gracias, Maria!*

Thank you, Andrés, for sharing your knowledge and experience, and for reminding me that glyphosate is toxic and dangerous.

Many thanks, Prof. Jürgen Gutowski, for your support, disposition, and feedback on this work. It is always a pleasure to learn from you.

Special thanks go for
my friends during the bachelor program, Cristian, Daniel, and Sofia. I learned from you and with you guys, many thanks!
my colleagues at the laboratory; Andrés, Alejandra, Eduardo, Pablo, and Isabel for the good coffee breaks. It was a pleasure to share ideas with you at LAIDEA, *¡Éxito siempre!*
And, to my Mexican friends Alejandro, Myriam and Jocelyn for their advice and support in the last chapter of this adventure.

Finally, I thank my best friend Ivana since the road would not have been so much fun without her. Thank you, sister, for always being there.

Dedicatory

Para mis papás, Bertha y Gregorio por su apoyo, confianza y amor a cada paso de mi vida.

And,
to everyone who has shared knowledge with me.

Related results with this research

- **Manuscript**

Portable semiconductor electronic devices for glyphosate detection: a review and potential perspectives, to be submitted IEEE Transactions on Electronic Devices.

- **Academic Achievements**

“Dr. Gustavo Baz Prada” Social Service 2021 Award
Supervisor: Dra. Alejandra Castro Carranza.

- **Book for children on environmental education**

Green Magic: My land our air, 2021

Authors: P. Abril Villagómez, B.Sc. Cristian E. Ramos Ruiz, Prof. Dr. Annette Ladstätter-Weissenmayer and Dr. Alejandra Castro Carranza.
Illustrators: Mildreth Reyes, Dr. Chantal Garduño and Dr. Maxime Dossin.

Abbreviations

EPSPS	5-enolpyruvylshikimate-3-phosphate
BED	Backscattered electron detection
I-V	Current-voltage
DFT	Density functional theory
EDX	Energy dispersive x-ray
EM	Energy minimization
FET	Field-effect transistor
FF	Force field
GGG	Glyphosate
GROMACS	Groningen Machine for Chemical Simulations
ITO	Indium tin oxide
IARC	International Agency for Research on Cancer
MIS	Metal-insulator-semiconductor
MD	Molecular dynamics
NPT	Number of atoms, pressure and temperature constant.
NVT	Number of atoms, volume and temperature constant.
PBC	Periodic boundary conditions
SEM	Scanning electron microscopy
SED	Secondary electron detection
UV	Ultraviolet
VMD	Visual molecular dynamics
ZnO	Zinc oxide
ZnO-NWs	Zinc oxide nanowires

Index

List of figures

List of tables

1 Motivation

In order to satisfy the global high food demand, agrochemicals have been indiscriminately applied to crops and seeds. Their massive and uncontrolled use has raised environmental and human health concerns [Carvalho, 2017, and Sellare, 2020].

Among commonly used agrochemicals, glyphosate (GGG) is a highly effective broad-spectrum herbicide [Duke, 2008] applied to crops to eradicate grasses and leaves through the inhibition of the critical plant growth enzyme 5-enolpyruvylshikimate-3-phosphate synthase (EPSPS) [H. Greim, 2015]. Glyphosate toxicology has been a highly debated topic over the last decades, some studies inform about its teratogenic [Dallegrave, 2003], mutagenic [Roustan, 2014], and carcinogenic [Mink, 2012] properties. In March 2015, the International Agency for Research on Cancer (IARC) classified it as Group 2A, "probably carcinogenic to humans" [IARC, 2015]. Despite this, it is currently reported as the globally most widely used agrochemical [Valle, 2019]. However, its health cost-benefit ratio questions its use and application.

Glyphosate is a synthetic substance capable of penetrating the soil, leaking into the water, and entering the human body´s vital processes. It has been found in countries with strict environmental regulations, such as Germany, where fourteen of the most famous beers contain herbicides [Guttenberger, 2016]. In Mexico, glyphosate is mainly used for corn, cotton, wheat, and soy crops. In 2017, the International Journal of Environmental Research and Public Health published a study on glyphosate presence in seven agricultural communities in Campeche, México. The research found glyphosate traces in the farmers' and their families' blood, urine, and breastmilk [Rendon-von, 2017]. In 2020, the Mexican government decided to gradually reduce glyphosate until it achieves its total ban in 2024 [Alcántara-de la Cruz R, 2021]. Many European countries also aim at a prohibition of glyphosate, for example, Germany presently plans this for end of 2023.

The existing methods and techniques for detection and quantification of the herbicide include high-performance liquid chromatography (HPLC), liquid chromatography with mass spectrometry (LC-MS), gas chromatography (GC), gas chromatography with mass spectrometry (GC–MS), ion chromatography with mass spectrometry (IC-MS), and capillary electrophoresis (CE). Valle et al. [Valle, 2019] reported a comparative analysis of glyphosate detection among these methods. However, although these techniques are highly selective and sensitive, they require high-cost equipment and qualified staff, making them not accessible to everyone.

Therefore, it is of great interest to develop sensitive, selective, and stable technologies for glyphosate detection and explore its possibilities to make them affordable for individuals and communities. Different efforts for more straightforward glyphosate detection have been reported in the literature. Mainly, electrochemical techniques based on glyphosate-metal complex formation stand out [Zambrano-Intriago, 2021]. Glyphosate possesses a high affinity to form complexes with metal ions, such as copper, cobalt, iron, aluminium, magnesium, and zinc. Caetano et al. reported the best complex stability theoretically with Zn ions [Caetano, 2012].

Metallic oxides have shown strong motives to be applied in electronic devices due to their interesting optoelectronic properties and simple chemical synthesis [Yu, 2016]. Among metallic oxides, zinc oxide (ZnO) has been demonstrated to be one of the most versatile materials, due to its chemical stability, piezoelectric properties, and biological compatibility.

In this work, the fundamentals of the ZnO/GGG interaction have been studied from both a theoretical and an experimental point of view. Firstly, the interaction of GGG with ZnO has been analyzed through molecular dynamics simulations to study its evolution over time. Based on these theoretical foundations, three different device structures have been fabricated, being then optically and electrically characterized to understand the mechanisms occurring at the interfaces to propose a portable, accessible, and sustainable device for glyphosate detection.

The research has been done in cooperation with the Semiconductor Optics group at the Institute of Solid-State Physics (IFP), Faculty 1 Physics/Electrical Engineering, concerning the fundamentals of semiconductor optics and the material ZnO, the Hybrid Material Interfaces (HMI) group, Faculty 4 Production Engineering, concerning theory and simulations, both University of Bremen, and the International Laboratory for Environmental Electronics Devices of ENES Morelia, National University of México (LAIDEA-UNAM), in the frame of the CONACYT project *Ciencia de Frontera* "Study of the electronic interaction between toxic molecules in the environment with organic semiconductors and oxides for the design of sustainable food, air and water sensors".

2 Fundamentals and Background

This section covers the theoretical information needed to understand the results presented throughout this thesis. First, the fundamentals of glyphosate and zinc oxide are presented. Subsequently, the basic principles to understand the theoretical results are described, i.e., the force field methods, molecular dynamics simulations, and an introduction to the GROMACS, VMD and CHARMM-GUI software packages.

For the analysis of the experimental results, the theory on the types of electric contacts is described, as well as the basics of the operation regimes and conditions for which field-effect transistors can be applied as sensor devices.

2.1 Glyphosate

Glyphosate (Figure 2.1) is a non-selective and broad-spectrum organophosphate compound, specifically a phosphonate. It is applied to control broadleaf weeds and grasses by inhibiting the critical plant growth enzyme EPSPS [Greim, 2015]. It is the most widely employed agricultural herbicide worldwide [Woodburn, 2000]. Table 1 resumes relevant GGG physical and chemical properties.

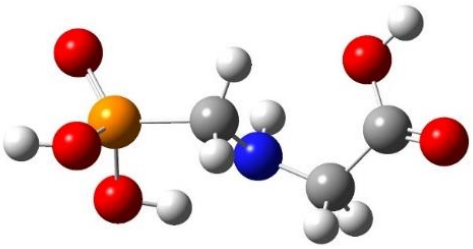

Figure 2.1. Chemical structure of glyphosate at neutral form (pKa = 2)[1].

Table 2.1. Physical and chemical properties of glyphosate. Data from [PubChem, 2022].

General Name	Glyphosate
IUPAC name	N-(phosphonomethyl)glycine
Chemical formula	$C_3H_8NO_5P$
Molecular weight	169.1 g/mol
Solubility in water	12 g/L (at 25 °C)
Log P	-3.4 (at 25 °C)
Density	1.705 g/cm3
Band gap*	6.48 eV
Color/Form	White crystals
Odor	Odorless

Glyphosate is a polar, nonvolatile herbicide that is highly soluble in water and insoluble in organic solvents [Dhamu, 2021]. It possesses neither chromophores nor fluorophore groups, thus complicating its detection by UV-Vis absorbance and fluorescence techniques [da Silva, 2013].

It is a hybrid ion with four dissociation constants; it exhibits different ionic species depending on its pH environment [Vidal, 2015]. Figure 2.2 illustrates these glyphosate dissociation species as a function of pH. Glyphosate is an amphoteric substance [Sánchez Martin, 1999]. Thus, it can react as an acid or base depending on its conditions. Furthermore, the amino, carboxylate and phosphonate groups present in the GGG molecule possess a high ability to form complexes with metallic ions [da Silva, 2013], e.g., Zn^{2+}-GGG.

*Data from a DFT simulation performed by Dr. Yesenia Arredondo and Dr. Claudia Briones-Jurado using the Quantum ESPRESSO software [Seemann, 2018].

[1] pKa measures the strength of an acid and is defined by the negative base ten of the acid dissociation constant (Ka).

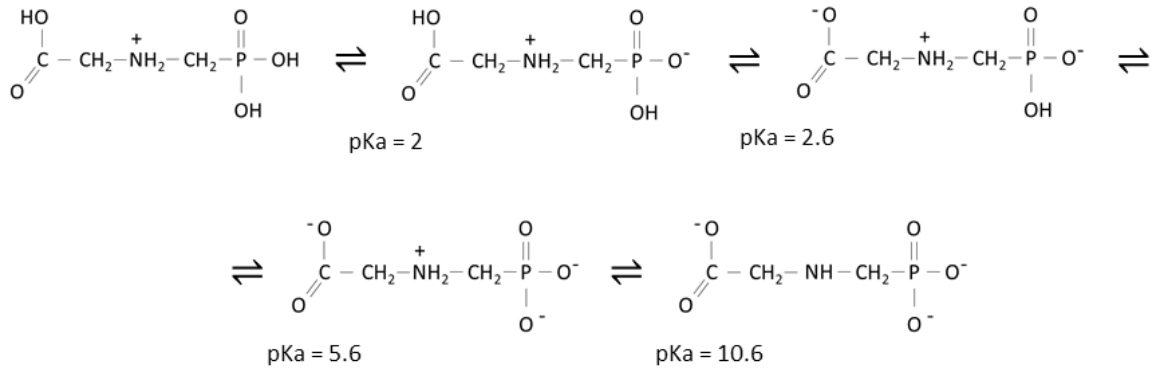

Figure 2.2. Glyphosate as function of pH. Image modified from [Vidal, 2015].

2.2 Zinc oxide

Zinc oxide (ZnO) is one of the most versatile materials, owing to its chemical stability, biologic compatibility [Czyzowska, 2022], photoelectrochemical and photocatalytic properties [Silva, 2021], and relatively low-cost production. It has been applied in multiple devices such as photodetectors [Hsueh, 2007], light emitters [Könenkamp, 2004], and sensors, e.g., piezoelectric field-effect transistor (PE-FET) composed of a ZnO nanowire for force/pressure tracking [Wang, 2006].

ZnO is a usually n-type semiconductor material that crystallizes in two main forms: hexagonal wurtzite and cubic zinc blend. The hexagonal wurtzite-type structure [Klingshirn, 2007] is the most stable. This more common structure exhibits a direct bandgap of 3.37 eV at room temperature [Janotti, 2009], corresponding to an absorbance in the UV region (Figure 2.3).

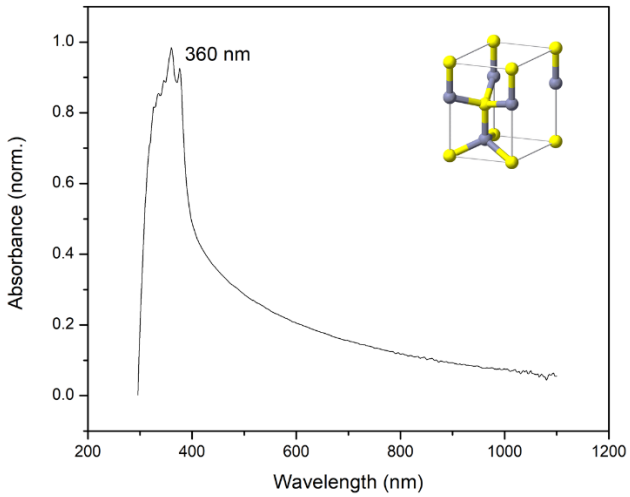

Figure 2.3. UV-Vis absorbance spectra of ZnO. On the top right corner, ZnO hexagonal wurtzite unit cell, Yellow– Zn; Grey–O [Klingshirn, 2007].

2.3 Theoretical

2.3.1 Force Field

In this work, force field methods were used to analyse and study the interaction between ZnO and glyphosate molecules, aiming to settle the theoretical foundation for developing a sensor capable of detecting the herbicide.

A Force Field (FF) is a mathematical expression that describes the dependence of the potential energy of a system based on the coordinates of its particles and a set of parameters [Monticelli, 2013]. These parameters are obtained either from *ab initio* semi-empirical quantum mechanical calculations or by assessing experimental data such as neutron, x-ray and electron diffraction, NMR, infrared, Raman, and neutron spectroscopy [González, 2011].

Quantum mechanics defines a system's most rigorous description [Bueren-Calabuig, 2014]; the *ab initio* methods are based on quantum chemistry. These provide a computational solution of the Schrödinger equation, taking into account electrons in the calculations and making it possible to study properties that depend on the electronic distribution (e.g., electronic energy and electron density) and the reactivity chemistry (e.g., forming and breaking bonds). However, due to computational costs its applicability is restricted to small systems. In contrast, empirical FF-based methods ignore electronic movements and calculate the system's energy based on classic mechanical principles, allowing for computing larger systems.

FF-based methods simulate systems containing hundreds or thousands of atoms over a time of several nanoseconds [Gonzalez, 2011] with a low computational costs, thus, possessing an advantage compared to *ab initio* MD simulations (e.g. DFT).

Many Forces Fields (e.g. CHARMM, AMBER and OPLS) are reported in literature designed to handle different types of systems. Nevertheless, a typical FF expression consists of intramolecular bonded and intermolecular non-bonded interactions (eq. 1) [Balzaretti, 2021]. Equation 1.1 and 1.2 describe the terms considered for each category.

$$V = V_{bonded} + V_{non-bonded} \quad (1)$$

$$V_{bonded} = V_{bonds} + V_{angles} + V_{dihedrals} \quad (1.1)$$

$$V_{non-bonded} = V_{Coulomb} + V_{van\ der\ Waals} \quad (1.2)$$

Bonded interactions

The terms in equation (1.1) refer to intramolecular bonded interactions or local contributions: bonds, angles, and dihedrals. Equation (1.3) expands all the terms considered for each contribution.

$$V_{bonded} = \sum_{bonds} k_{b_{ij}}(R_{ij} - R_0)^2 + \sum_{angles} k_{a_{ijk}}(\theta_{ijk} - \theta_0)^2 + \sum_{dihedrals} k_{d_{ijkl}}\left[1 + \cos(n_{ijkl}\phi_{ijkl} - \phi_0)\right] \quad (1.3)$$

Bonds. The stretching bond term (first term in eq. 1.3) is often represented with a harmonic bond potential. The potential is based on Hook´s law for elastic forces, describing the interaction between atoms. The use of the harmonic function implies that chemical bonds cannot be broken. Therefore, no chemical process can be studied through FF.

The R_0 term represents the equilibrium distance or reference bond length, R_{ij} the distance between the centers of atoms *i* and *j* at a given time, and $k_{b_{ij}}$ the force constant. Figure 2.4 shows these parameters in a schematic representation.

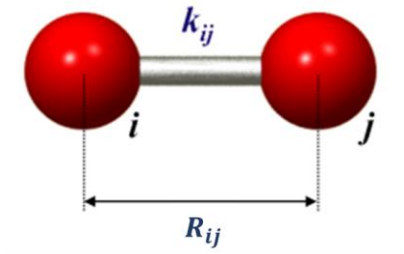

Figure 2.4. Bond formed between two atoms at positions R_i and R_j. Image from [PumMa].

Angles. Between two bonds sharing an atom, an angle is formed. Angle bending is usually represented by a harmonic potential as well (second term in eq. 1.3). $k_{a_{ijk}}$ represents the angle force constant. θ_{ijk} represents the time-dependent angle form for the set of three consecutive atoms *i*, *j* and *k*, whereas θ_0 is the angle at its minimum energy position, namely as reference angle. Figure 2.5 illustrates a schematic representation of these parameters.

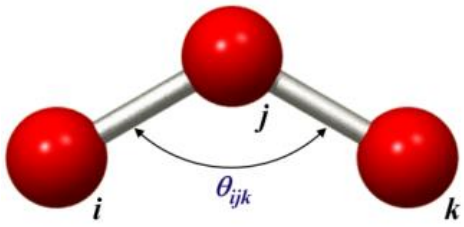

Figure 2.5. Angle formed between three atoms at positions R_i , R_j and R_k. Image from [PumMa].

Dihedrals. Dihedrals are an analogous to the concept of angles in a three-dimensional system. It is defined as the angle between two half-planes (faces) having the same edge as their origin [Balzaretti, 2021].

Dihedrals allow for the description of the torsion of the molecule or a part of it. Two types of torsions exist: proper and improper. Proper torsion is given by torsion occurring in a quartet of consecutively bonded atoms (Figure 2.6a), whereas improper torsion is attributed to four not successively bonded atoms (Figure 2.6b).

(a) (b)

Figure 2.6. Dihedral describing a (a) proper and (b) improper torsion, formed between four atoms at positions R_i , R_j, R_k and R_l. Image from [PumMa].

Usually, the torsional energy is represented by a cosine function (third term in eq. 1.3).

The torsional parameter, $k_{d_{ijkl}}$ is derived from *ab initio* calculations and refined by experimental data such as molecular geometries or vibrational spectra [González, 2011]. Its values are generally bigger than $k_{a_{ijk}}$, indicating that it takes less energy for a bond angle to deviate from its reference value [Monticelli, 2013].

The term ϕ_{ijkl} represent the torsional angle and ϕ_0 the torsional angle at a starting equilibrium position of choice. Finally, multiplicity n_{ijkl} defines the number of energetic minima or maxima between 0 and 2π.

Non-bonded interactions

The non-bonded or intermolecular interactions correspond to electrostatic and van der Waals forces. Equation (1.4) expands these terms of equation (1.2).

$$V_{non-bonded} = \sum_{i \neq j} \frac{1}{4\pi\varepsilon_0 \varepsilon} \frac{q_i q_j}{R_{ij}} + \sum_{i \neq j} 4\gamma_{ij} \left[\left(\frac{\sigma_{ij}}{R_{ij}} \right)^{12} - \left(\frac{\sigma_{ij}}{R_{ij}} \right)^{6} \right] \quad (1.4)$$

Electrostatic. Each atom in the system possesses a partial atomic charge. The first term in eq. 1.4 describes electrostatic interactions between two atoms in the same or a different molecule. Coulomb´s law is used to compute its contribution to the total energy.

q_i and q_j represent the charges of the atoms i and j, respectively, R_{ij} is the distance between atoms i and j, ε_0 is the vacuum permittivity and ε the dielectric constant of the medium. Figure 2.7 shows a schematic representation of these terms.

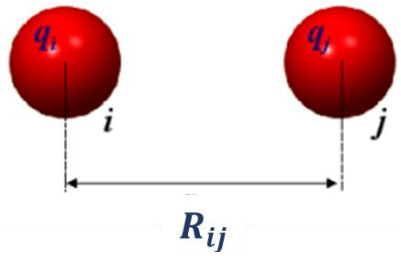

Figure 2.7. Electrostatic interaction between two atoms at positions R_i and R_j, with total charges q_i and q_j, respectively. Image from [PumMa].

Van der Waals. Van der Waals interactions between two atoms arise from the balance between repulsive and attractive forces [González, 2011]. The usual way to describe Van der Waals contribution is given by the 12-6 Lennard-Jones (LJ) potential.

Figure 2.8 illustrates the 12-6 LJ potential for the interaction between two atoms *i* and *j*, in function of their interparticle distance. The 6 term represents the attractive force between dipoles in the atoms, whereas the 12 term is the repulsion force of the electron clouds when they are near each other. The equilibrium position r_m is the distance at which the potential reaches its minimum and the repulsive and attractive forces are equal.

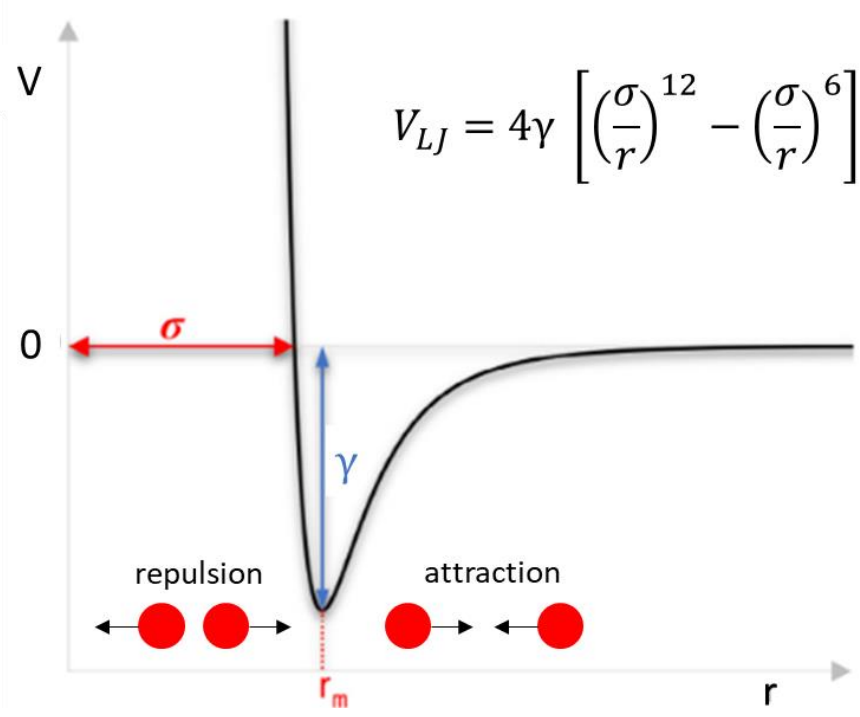

Figure 2.8. The 6–12 LJ potential graph considering potential (V) vs interparticle distance (r). Image modified from [Sikorska, 2020].

The term γ_{ij} corresponds to the dispersion energy (depth of the potential well) and σ_{ij} to the distance where the potential equals cero.

2.3.2 Molecular Dynamics

Molecular dynamics (MD) is a computer simulation method that produces a trajectory i.e., sequential snapshots of a simulated N particle system by integrating Newton´s equations of motion at specific time periods.

Computing requires a set of initial conditions for each atom, a model representing the forces acting between the particles (i.e., a force field), and boundary conditions. Moreover, an energy minimization and thermodynamic equilibration pre-steps are needed. After that, the classical equation of motion needs to be solved:

$$m_i \frac{d^2 R_i}{dt^2} = \vec{F}_i = -\frac{\partial}{\partial R_i} V\left(\vec{R}_1, \vec{R}_{2,\ldots}\ \vec{R}_N\right) \qquad (2)$$

In the above equation, $V\left(\vec{R}_1, \vec{R}_{2,\ldots}\ \vec{R}_N\right)$ is the potential energy and depends on the coordinates of the N particles.

Equation (2) is a second-order nonlinear differential equation. Thus, it has to be solved numerically using an integration algorithm.

Initial conditions

The initial conditions are the initial positions and velocities of each particle in the system. Usually, for disordered systems, the positions can be randomly generated. The initial velocities are attributed randomly from a Maxwellian distribution obtained at the desired temperature [González, 2011].

Boundary conditions

The Periodic Boundary Conditions (PBC) allow for a reproduction of the simulation cell along the three Cartesian directions. This way, the simulation box is surrounded by an infinite number of cells, as shown in Figure 2.9.

PBC are to maintain equilibrium in the system; if one particle leaves the cell, an imaged particle enters from the opposite side to replace it. Nevertheless, only the N atoms inside the main cell are considered for the simulation [Tesson, 2016].

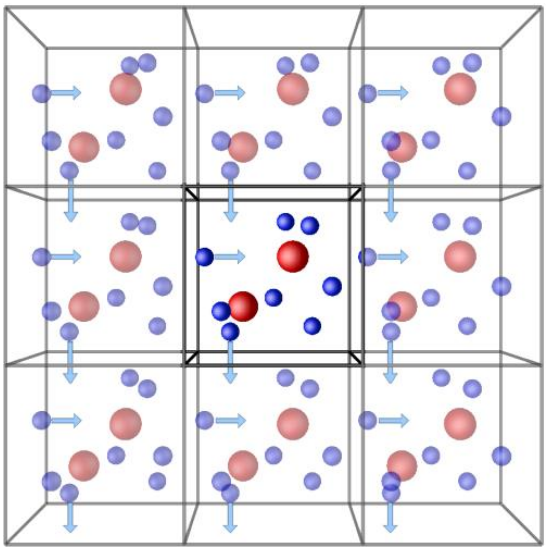

Figure 2.9. Periodic Boundary Conditions [Tesson, 2016].

Energy minimization

An energy minimization (EM) is a pre-step for removing excess energy. EM aims at finding the nearest local energy minimum. However, it is essential to note that this may not be the most stable configuration since the structural minimization stops when facing an energy barrier. EM ensures a reasonable starting structure in terms of geometry and solvent orientation.

Thermodynamic ensembles

When dealing with a chemical system depending on parameters such as temperature and pressure, it is useful to equilibrate them before starting the MD production run. In this way, it is not necessary to be aware of them during the simulation, because they are already in equilibrium.

The lack of control over temperature and pressure fluctuating without a precise value generates integration errors, force fluctuations, and inconsistencies in the forces [Balzaretti, 2021]. To avoid these problems of the system, it is useful to bring it to equilibrium through the use of NVT and NPT thermodynamic ensembles.

> *NVT*. A constant number of atoms, fixed volume, and temperature, called a "canonical ensemble".
> *NPT*. A constant number of atoms, fixed pressure, and temperature. The volume is allowed to change.

Figure 2.10 schematizes the use of thermodynamic ensembles. The NVT purpose is to heat (usually starting from 0 K) the system up and down to a particular temperature; it can be around 300 K (room temperature) or a desired temperature value [Balzaretti, 2021]. NPT

consists of a volumetric compression until a specific pressure or density (usually 1000 kg/m^3) for the solvent is achieved. This can be done by using thermostats and barostats.

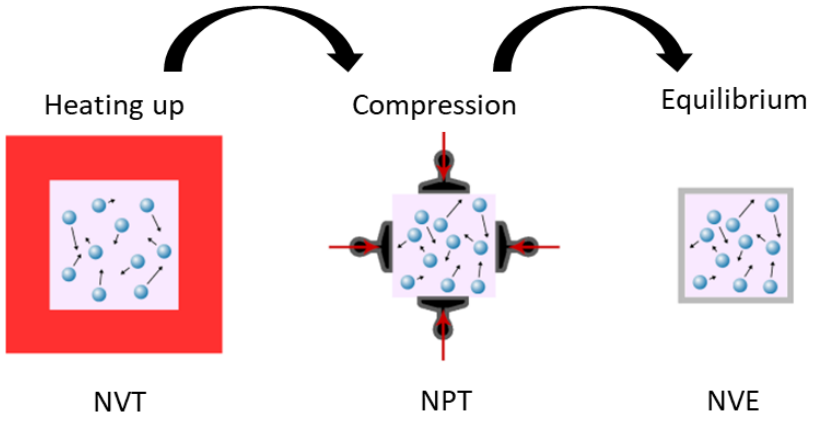

Figure 2.10. Schematic representation of a typical equilibration routine [Balzaretti, 2021].

A thermostat is defined as an algorithm to scale the velocities of particles and control the MD simulation temperature. The main methods for temperature management are velocity rescaling [Bussi, 2007], Berendsen thermostat [Berendsen, 1984], and Nosé-Hoover thermostat [Nosé, 1984].

In real-life a barostat is a device used to maintain constant pressure in a closed chamber .However, in MD the term barostat refers to pressure control algorithms used to regulate the pressure by adjusting the volume of the simulated system [Stueker, 2014].

2.3.3 GROMACS

GROMACS (GROningen MAchine for Chemical Simulations) is a package designed by the University of Groningen, The Netherlands, to perform molecular dynamics [Bekker, 1993]. It was developed initially for biochemical molecules like proteins, lipids, and nucleic acids. Due to its capacity to calculate non-bonded interactions quickly it is also used to compute non-biological systems, i.e., semiconductors and hybrid interfaces [Balzaretti, 2021].

2.3.4 VMD

The Visual Molecule Dynamics (VMD) is a molecular modelling and visualization computer program [Humphrey, 1996] developed by the University of Illinois Urbana-Champaign and mainly used to view and analyze MD simulation results.

2.3.5 CHARMM-GUI

CHARMM-GUI is an interactive website tool employed in molecular modelling communities to build complex systems and prepare their inputs with well-established reproducible simulation protocols. It has been used for molecular simulation packages such as CHARMM, GROMACS, AMBER, GENESIS, Tinker, LAMMPS, Desmond, and OpenMM [Jo, 2008].

2.4 Electronic devices for sensing applications

2.4.1 Metal-semiconductor contacts

Choosing the most appropriate electrode materials is crucial to develop efficient electronic devices.

In general, there are two types of contacts in a metal-semiconductor junction, i.e., Schottky and Ohmic contacts. Since ZnO is used along this work, the specific case of a junction consisting of a metal and an n-type semiconductor is discussed to introduce the reader into both.

Figure 2.11a shows an ideal energy band diagram of an isolated metal and an n-type semiconductor. The parameters ϕ_m and ϕ_s refer to the metal and semiconductor work functions, respectively, while χ corresponds to the electron affinity. Here, $\phi_m > \phi_s$ is assumed; therefore, the Fermi level in the semiconductor (E_F) is above that in the metal. Once both materials are put in contact (Figure 2.11b), E_F aligns energetically to reach the thermal-equilibrium condition, forming therefore a depletion zone at the interface represented by a band bending of the vacuum level (E_{vac}) and, likewise, of the valence and conduction bands of the semiconductor (E_V and E_C, respectively). In other words, electrons from the semiconductor flow into lower energy states in the metal, leaving positively charged donor atoms behind which yield a potential barrier ϕ_{B0} due to the depleted zone at the interface.

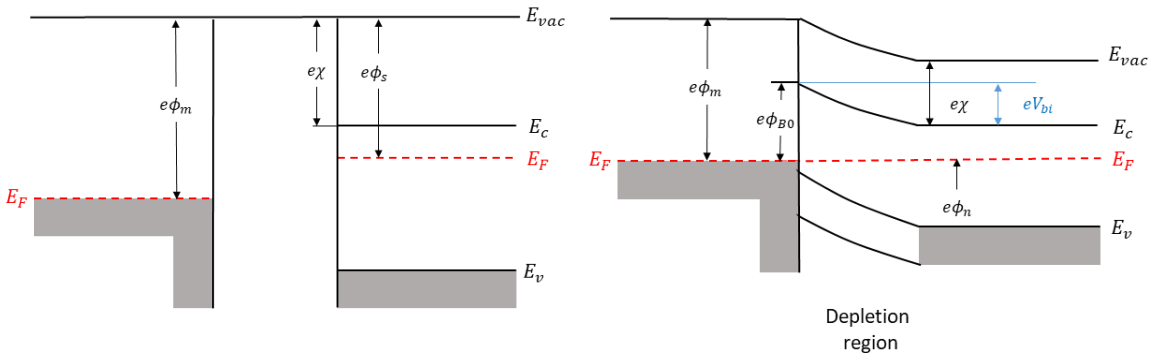

(a) (b)

Figure 2.11. Energy band diagram of an isolated (a) and a contacted (b) metal and an n-semiconductor junction for $\phi_m > \phi_s$.

ϕ_{B0} is known as the Schottky barrier which refers to the potential barrier seen by the electrons in the metal trying to move into the semiconductor [Neamen, 2011]. It is defined as

$$\phi_{B0} = \phi_m - \chi$$

The term V_{bi} in Figure 2.11b corresponds to the build-up potential of the junction, and it is the barrier seen by electrons in the conduction band trying to move towards the metal.

Conversely, in the case where $\phi_m < \phi_s$ the energy band diagrams before and after contact are shown in Figures 2.12a and 2.12b, respectively. Here, instead of a depletion zone, an accumulation region is formed, and therefore, electrons have no potential barrier to overcome. This phenomenon is known as Ohmic contact, i.e., a low-resistance junction that provides conduction in both directions between the metal and the semiconductor.

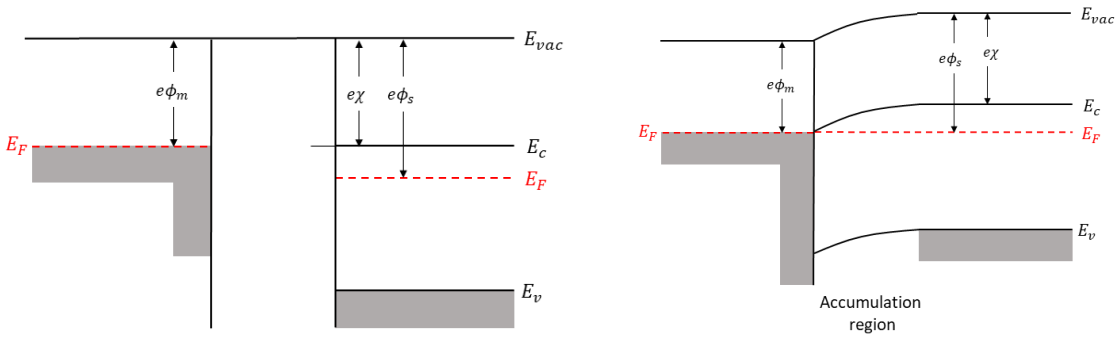

(a) (b)

Figure 2.12. Energy band diagram of an isolated (a) and a contacted (b) of a metal and an n- semiconductor junction where $\phi_m < \phi_s$.

Figure 2.13 illustrates the I-V characteristics for Schottky and Ohmic contacts biased in forward and reverse direction, while Table 2.2 gives the parameters defining them for n and p-type semiconductors. A flat-band condition indicates that neither a depletion nor an accumulation zone are formed in the junction.

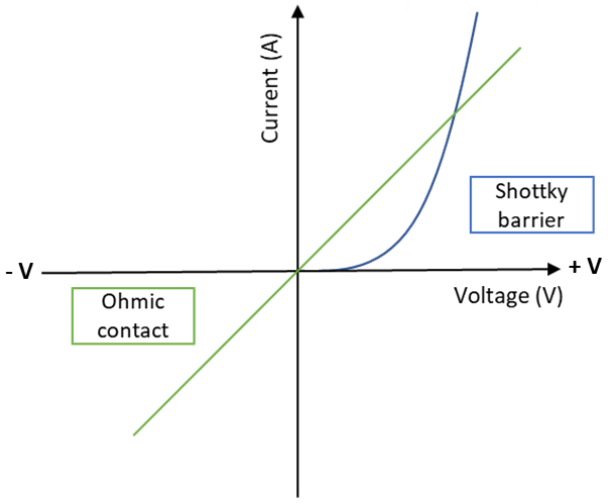

Figure 2.13. Ideal I-V characteristics for Schottky (blue) and Ohmic (green) junctions.

Table 2.2. Ohmic and Schottky contacts for n-type and p-type semiconductors

Contact type	n-type	p-type
Ohmic	$\phi_m < \phi_s$	$\phi_m > \phi_s$
Schottky	$\phi_m > \phi_s$	$\phi_m < \phi_s$
Flat band	$\phi_m = \phi_s$	$\phi_m = \phi_s$

2.4.2 Field-Effect Transistors

A Field-Effect Transistor (FET) is a three-terminal device (G gate, D drain, S source) in which a current flows between source and drain which can be modulated by a gate potential [Castro-Carranza, 2013]. Depending on the architecture, the metal-insulator-semiconductor (MIS) structure, generally formed by a gate electrode (a metal), an insulating layer, and a semiconductor material constitutes the core of the device.

Generally, FETs control the current between drain and source (I_{DS}) via applying tunable V_{GS} between the gate and source electrodes. At V_{GS}=0, source-drain current is suppressed by recombination of source carriers with the majority carriers in the semiconductor, thus forming a barrier. As V_{GS} is applied to the gate, an electric field inside the dielectric layer is formed, which generates a dual-electrical layer which repel the majority carriers thus forming a thin channel for the minority carriers in the semiconductor. Consequently, these charge carriers can be transported in the channel region adjacent to the dielectric layer [Zhao, 2020].

I_{DS} can be plotted in domain of V_{GS} at different values of V_{DS}, or in domain of V_{DS} at different values of V_{GS}. They are called transfer and output characteristics, respectively. Figure 2.14 illustrates both cases.

FETs can work in either linear or saturation regimes, depending on the voltage applied to the electrodes. In Figure 2.14b, the ohmic region represents the linear regime. Once the cut-off condition is achieved, the saturation region is reached, and a commonly constant current value flows from drain to source.

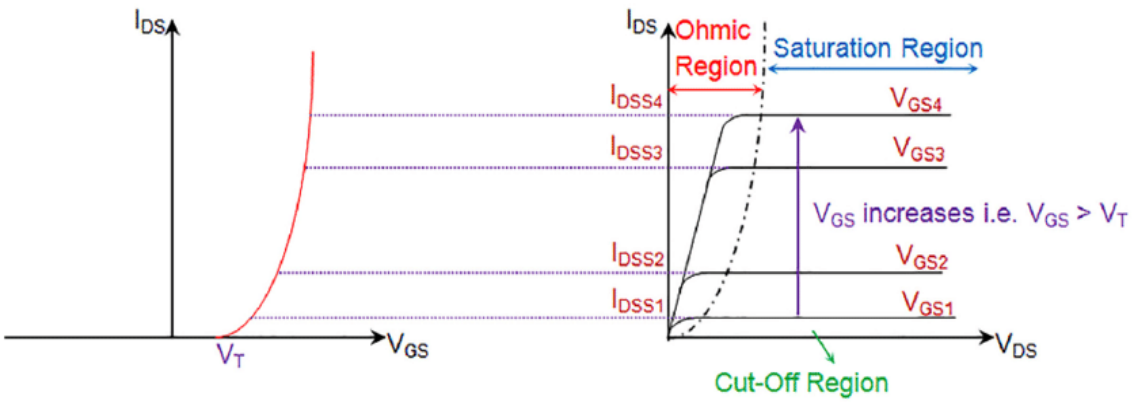

(a) (b)

Figure 2.14. N channel enhancement type FET transfer (a) and output (b) characteristics Reproduced with permission under the Creative Commons license [Kivrak, 2019].

Among the different types of FETs, thin-film transistors (TFTs) are highly suitable due to a lower-cost processing, the versatility to be functionalized by multiple materials, and the easy implementation of soluble semiconductors as active layers. Particularly, by using sensitive linker materials, a coplanar bottom-gate TFT can detect on its exposed channel specific external stimuli and transduce them into electrical signals. Figure 2.15 depicts a schematic n-type TFT whose operation is defined by a majority charge-carrier accumulation in the channel induced by the gate bias (V_{GS}).

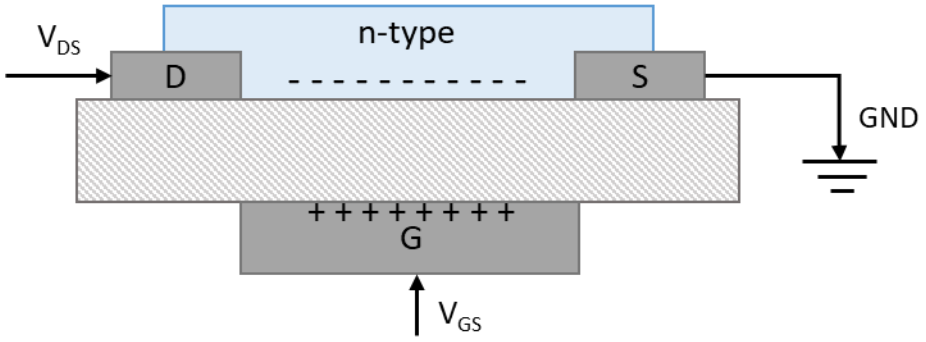

Figure 2.15. A typical coplanar bottom-gate TFT. Metallic electrodes drain (D), source (S) and gate (G) are shown in grey. The insulating material is depicted in grey mesh, and the n-type semiconductor thin film, as the active layer, in blue.

3 State of Art

This section presents an overview of the previously reported studies on portable glyphosate (GGG) detection devices. Particularly focus is put on solid-state sensors, specifically field effect transistors (FETs). Studies that reported ZnO-GGG interaction for degradation or detection are presented as well.

Most of the research effort on sensitive and fast GGG detection focused on electrochemical methods. Specifically, voltammetric techniques have been investigated and developed such as cyclic voltammetry, amperometry, and chronoamperometry. Zambrano-Intriago et al. [Zambrano-Intriago, 2021] published a comprehensive review on electrochemical sensors for glyphosate detection. The modification of electrodes through Molecularly Imprinted Polymers (MIPs), Metal-Organic Frameworks (MOFs), as well as metal and biological elements have been shown to enhance device performance (i.e., selectivity, sensitivity, range of operation, detection limit). Despite of these outstanding performance characteristics, electrochemical sensors possess a limited lifetime due to electrode degradation [Hübert, 2011], making them a non-sustainable technology.

Recently, Ansano et al. have been developing a detection method for GGG based on the competitive complexation between the organic semiconductor poly(3-(5-carboxypentyl)thiophene-2,5-diyl) (P3CPT), copper (II) ions, and the herbicide [Asano, 2020]. The carboxyl group present in P3CPT molecule possesses a high affinity to Cu (II) ions. Thus, GGG competes against P3CPT for the metallic ions present in the solution. This competition is recognized through current flow changes. Asano's group has explored this detection mechanism on different FETs configurations such as WG-OTFT (water-gate organic thin film transistors) [Asano, 2020 and Minami, 2021] and WG-OFET (water-gate organic field effect-transistor) combined with a microfluidic chamber [Asano, 2021]. They reported potential GGG electronic devices with detection limits of 260 and 21.98 μg L^{-1}, respectively. In Table 3.1, FETs devices for GGG detection in water solution as reported in the literature are compared.

Additionally, Caetano et al. studied the interaction of glyphosate with Zn^{2+} , Ca^{2+} , Mg^{2+} , Cu^{2+} , Co^{3+} , Fe^{3+} , Cr^{3+} , and Al^{3+} ions using density functional theory (DFT) modeling methods to evaluate the effects that govern the complexation between GGG and the metallic ions. These results indicated that complexes formed with divalent cations are more stable than those formed with trivalent cations, showing order stability as follows: Zn > Cu > Co > Fe > Cr > Al > Ca >Mg [Caetano, 2012]. In this way, the study of ZnO and GGG exhibits potential interactions that could be used to detect the herbicide.

Table 3.2 summarizes the reported experimental studies on ZnO/GGG interaction either for degradation/removal or detection of the herbicide.

Table 3.1. FETs sensors for GGG detection reported in the literature.

Device	Materials	Mechanism of detection	Detection concentration ($\mu g\ L^{-1}$)	LOD ($\mu g\ L^{-1}$)	Ref.
WG-OFET combined with a microfluidic chamber	P3CPT, Cu^{2+}	Competitive complexation among GGG-Cu^{2+}-P3CPT.	0 - 1,691	21.98	Asano et al., 2021.
WG-OTFT			0 - 50,730	260	Sasaki et al., 2020. Minami et al., 2021.
HGOFET	Photosynthetic cyanobacteria, alginate hydrogel, poly (DPP-DTT)	GGG presence affects bacteria´s photosynthetic activity, transduce into a drop of drain current.	1,691	N/A	Le Gall et al., 2021.
EGFET	AChE/CdS/ ZnO	Inhibition of acetylcholinesterase activity by GGG.	1.6×10^{-7} – 0.0016	6.42×10^{-8}	Yu et al., 2021.

N/A: not available data
WG-OFET: water-gate organic field-effect transistor, WG-OTFT: water-gate organic thin film transistor, HGOFET: hydrogel-gated organic field-effect transistor, EGFET: extended-gate field-effect transistor, AchE: acetylcholinesterase, CdS: cadmium sulfide.

Table 3.2. ZnO/GGG reported experimental studies.

Structure	Degradation /removal	Detection	General description	Ref.
ZnO-NPs	✓		Removal of GGG-based herbicide in aqueous solution using ZnO-NPS. UV-Vis absorption spectra indicated herbicide degradation. An adsorption model for GGG ZnO-NPs surface is proposed.	Páez et al., 2019.
	✓		Photocatalytic degradation of GGG by clustered ZnO-NPs. NPs synthesized by precipitation with low-cost materials.	Sujinnapram et. al., 2021.
ZnO-NCs			Study of the interaction of GGG-NCs under pH-controlled conditions. A model for GGG-ZnO interaction at: $2.6 < pH < 10$ and $pH > 11$ is proposed.	Do Valle et al., 2021.
ZnO-QDs		✓	Use of ZnO-QDs for the detection and degradation of GGG in water. Detection through optical electrochemical techniques.	Sahoo et al., 2018
MWCNTs screen printed electrodes		✓	Electrochemical detection by MWCNTs screen printed electrodes decorated with nano-ZnO. The addition of ZnO layer enhances the electrochemical detection signal for GGG detection.	Habekost et al., 2017.
MIP-PPy ZnO nanorods		✓	Electrochemical detection by MIP-PPy coupled with ZnO nanorods vertically grown on ITO electrode. A ZnO growth process optimization is necessary.	Mazouz et al., 2017.

ZnO-NPs: ZnO nanoparticles, ZnO-NCs: ZnO nanocrystals, ZnO-QDs: ZnO quantum dots, MWCNTs: Multi-walled carbon nanotubes, MIP-PPy: Molecularly imprinted polypyrrole.

For the specific case of the ZnO/GGG interaction, there have been no calculations reported yet. This opens a scientific question to address: is ZnO a potential candidate material for GGG detection? The research performed in this thesis focuses on addressing that task by understanding the processes occurring at the ZnO/GGG interface with the aim to propose a portable, accessible, and sustainable device for GGG detection.

4 Methods

This chapter presents the methods used to study the ZnO-glyphosate system. Firstly, in Chapter 4, the methodology used for the MD calculation is addressed; the ZnO and GGG models employed are introduced and presented as well as a general system overview. Furthermore, it describes the calculation protocols and the data analysis. Afterwards, the experimental methods used to fabricate and characterize the devices are presented.
In Chapter 4.2, the ZnO-NWs fabrication process is described. Moreover, the fabrication processes for the device's structures are given. Finally, the methods used to characterize such devices are briefly introduced: scanning electron microscopy, energy dispersive x-ray spectroscopy, UV-vis spectroscopy and current-voltage characteristics.

4.1 Theoretical setup and system preparation

4.1.1 ZnO and GGG model

The glyphosate structure was provided by Maria von Einem (HMI group, Univ. of Bremen) and parameterized with the CHARMM36 (C36) force field over CHARMM-GUI [Jo, 2008]. Each GGG molecule possesses a partial charge of -2, based on a biological pH environment (pH of ~ 7). Figure 4.1 shows the chemical structure under this condition.

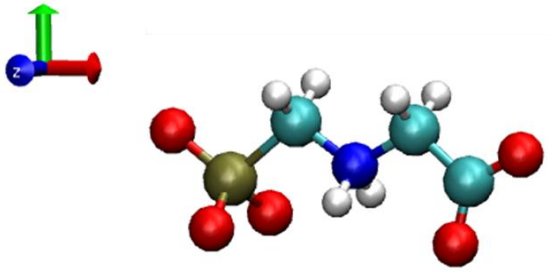

Figure 4.1. Chemical structure of glyphosate at pH ~ 7. Red – O; Blue – N; Cyan – C; Green – P; White – H. The upper left figure represents the Cartesian coordinates' axis: x-red, y-blue, and z-green. Illustrated with VMD [Humphrey, 1996].

The used ZnO bulk was provided by Massimo Delle Piane [Michaelis and Delle Piane, 2021] and consists of xy unit cells of ZnO in xy conformation plus hydroxyl groups for protonation equilibrium. It has a surface size of 2.6346 nm x 2.1193 nm, a volume ≈ 5.58350 nm^3 without considering hydroxyl groups (-OH).

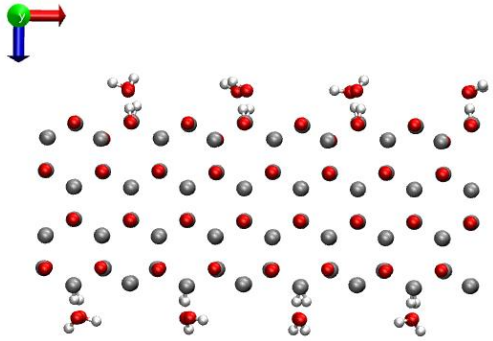

Figure 4.2. Structure of ZnO bulk. Red – O; Grey – Zn; White – H. Illustrated with VMD [Humphrey, 1996].

The system consists of four glyphosate molecules on top of the ZnO slab in a box with dimensions of 2.6346 nm x 2.1193 nm x 12 nm, volume 67.002 nm^3.

MD calculations were performed with the GROMACS version 2021.3 package. The computational settings used for the Force Field simulations are presented below.

4.1.2 System overview

Two different simulation protocols, type A and type B, were used to analyze the system. These planned to have two adsorption mechanisms to analyze, a so-called indirect and direct one, respectively.

Type A

As shown in Figure 4.3 the starting structure considered in this procedure consists of four glyphosate molecules above the ZnO slab. Once the system and the cell are defined and the PBC established, the box is solvated using the transferable intermolecular potential 3P (TIP3P) model, commonly used for water. Since each GGG possesses a charge of -2, eight Na^+ ions were added at random positions to neutralize the charge in the system.

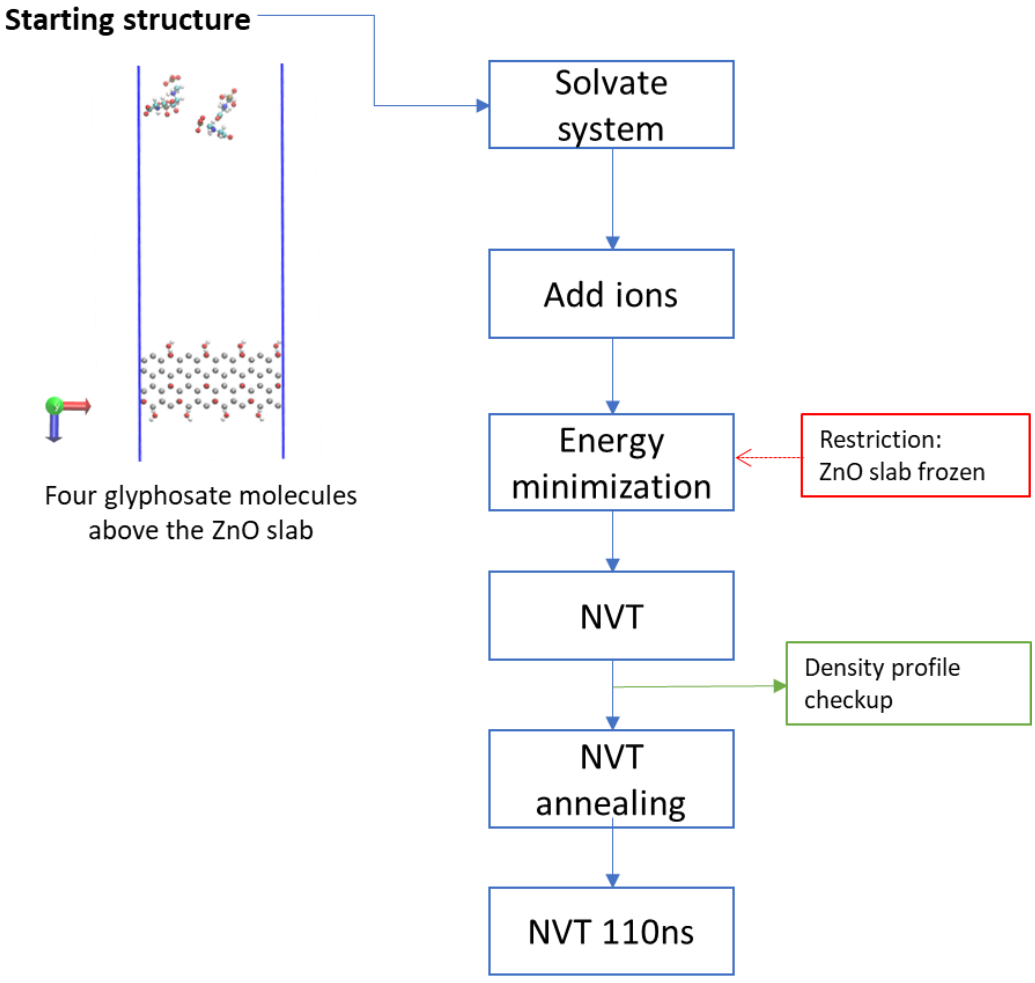

Figure 4.3. Flow diagram procedure type A.

An EM was performed with the aim to remove the excess energy and to ensure to get an optimized structure in terms of geometry and solvent orientation. Here, a restriction of the movement of the ZnO slab is considered by freezing it.

For this protocol, the thermodynamic equilibration has been archived by assumption of an NVT ensemble over 0.3 ns at 300 K using the Berendsen thermostat. An NPT ensemble was not possible to compute due to the ZnO freezing condition. Therefore, a checkup on the density profile of water in the box replaces this part in the standard equilibration procedure; a value close to the real water density value ensures a pressure-temperature equilibration.

To increment the adsorption modes, 10 annealing cycles between 300 and 500 K, each applied for 2 ns, were applied. Finally, the system was calculated molecularly for a 110 ns production run using time steps of 2 fs that was used to evaluate the adsorption modes.

Type B

For type B, the starting structure consisted of four glyphosate molecules above the ZnO slab and eight Na^+ ions below it (see Figure 4.4) to equilibrate the charge to zero in the system.

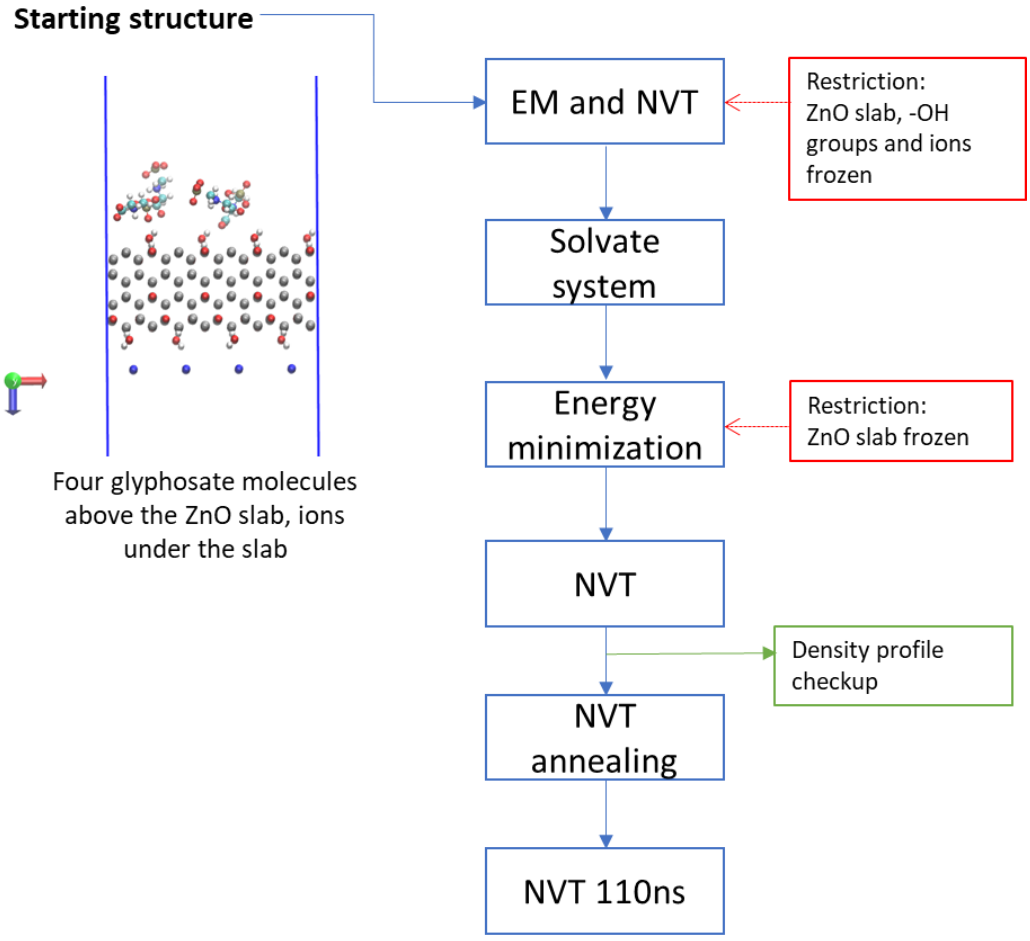

Figure 4.4. Flow diagram procedure type B.

Under vacuum conditions, a first EM after an NVT ensemble (as described in the previous section) were performed under assumption of a movement restriction of the ZnO slab, carboxyl groups, and the ions by freezing them. These previous steps were performed before solvation to directly attach the GGG molecules to the surface and thus to realize the case of directly adsorbed molecules. After that, the system was solvated with the TIP3P water.

Consequently, a second EM was performed with only the ZnO slab restricted in movement.

For the thermodynamic equilibration, an NVT ensemble was calculated over 0.3 ns at 300 K using the Berendsen thermostat. The NPT ensemble was again not possible to compute, hence, it was skipped since the water density checkup allowed it.

Afterwards, the same annealing cycles as described in type A were calculated. Finally, a 110 ns molecular production run using time steps of 2 fs was computed for the adsorption modes' analysis.

For each method, different GGG starting configurations were simulated. These can be seen in Table 4.1.

By using procedure type A, two simulations with GGG molecules randomly rotated were performed, A1 and A2. For the AR (reference simulation), GGG molecules were placed far from the slab.

Table 4.1. Description of the starting configurations used for protocols type A and B.

Type A	
A1	GGG randomly rotated
A2	GGG randomly rotated
AR	GGG far away from the ZnO
Type B	
B1	GGG randomly rotated
B2	GGG randomly rotated
B3	GGG randomly rotated
P-down	GGG rotate 90°
COOH-down	GGG rotate 270°

For the case of procedure type B, production runs B1, B2, and B3 with GGG molecules randomly rotated were performed. Moreover, two simulations with GGG molecules with a starting preference either for the phosphonate group or the carboxyl group to the slab were performed, P-down and COOH-down. Figure 4.5 gives a schematic representation of the P-down and COOH-down starting configurations.

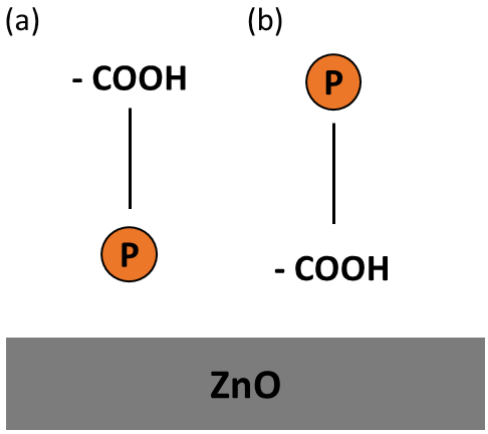

Figure 4.5. Schematic representation of (a) P-down and (b) COOH-down starting configurations.

4.1.3 Calculation protocol

Before starting the MD calculation, the system was equilibrated through an EM and thermodynamic ensembles

Energy minimization

Once the systems were assembled and solvated an EM was performed to ensure an appropriate geometry and no steric clashes. Figures 4.6a and 4.6b show the energy minimization of system types A and B, respectively.

An important aspect to ensure a successful EM is observing a decrement of potential energy through the number of iterations, ideally to a negative value. However, due to the system´s restriction conditions, a negative potential value was not possible to achieve here.

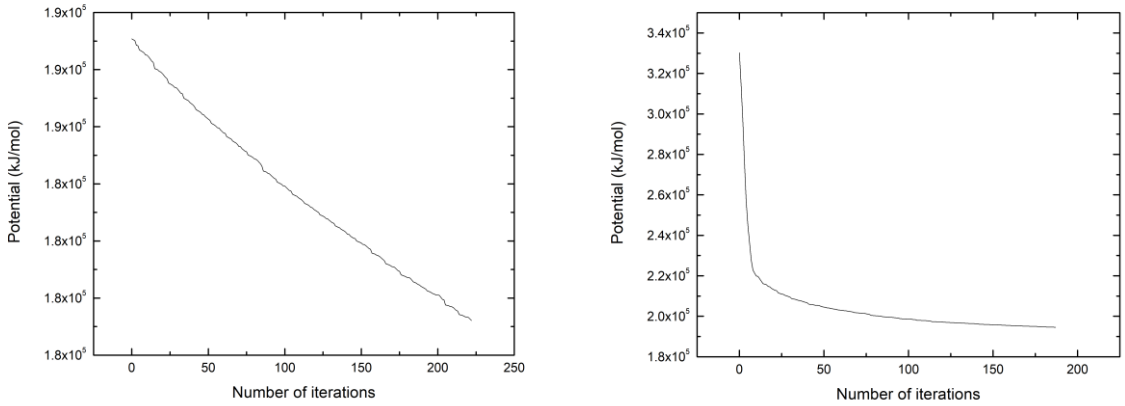

(a) (b)

Figure 4.6. Potential energy over number of iterations for the simulation types (a) A and (b) B.

Equilibration ensembles

NVT. Temperature profiles from type A and B procedures are shown in Figures 4.7a and 4.7b, respectively. A fluctuation over a temperature range of about 15 K can be noticed.

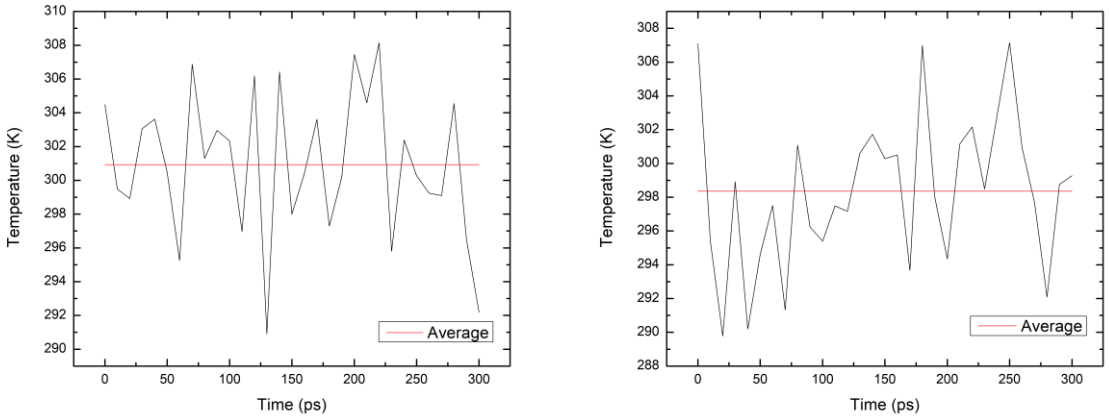

(a) (b)

Figure 4.7. Temperature profile of the simulation type (a) A and (b) B.

NPT. The changing volume ensemble was not possible to compute due to the ZnO slab freezing condition.

In order to ensure a pressure-temperature equilibration, the water density profile for types A and B was calculated after the NVT equilibration step. Figures 4.8a and 4.8b show the solvent density profiles for the simulations A1 and B1, respectively. The overall water density is around 1000 kg/m^3. Thus, the NPT ensemble was skipped.

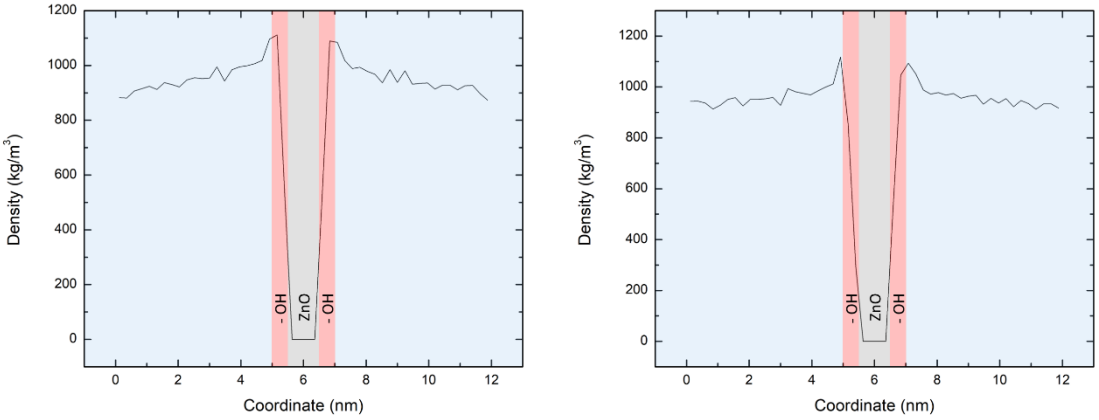

(a) (b)

Figure 4.8. Water density profiles for type A (a) and B (b).

4.1.4 Data analysis

The results were analyzed through a Python script created by Maria von Einem and Filippo Balzaretti based on the angle degree formed between GGG and the slab. Originally, it was used to analyze GGG on a Rutile TiO_2 slab [Balzaretti, 2021].

For the analysis, two vectors were defined, $\vec{a}$ and $\vec{b}$. Vector $\vec{a}$ has an arrow starting point at the phosphorus atom of GGG and an end point at the carbon atom from the carboxyl group in the molecule, while the $\vec{b}$ vector is defined by the x-y plane where the ZnO slab lies in (see Figure 4.9).

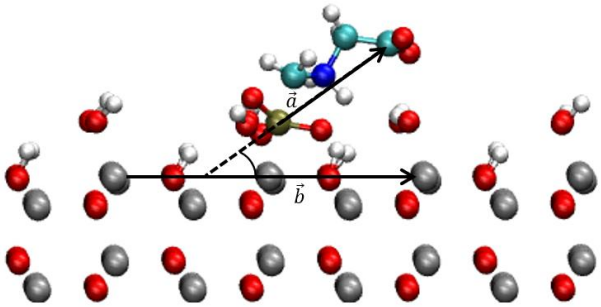

Figure 4.9. Schematic representation of vector $\vec{a}$ and $\vec{b}$ in the system.

Based on the angle formed by these two vectors in the 3D plane, two different adsorption modes are considered as proposed by Balzaretti et al. [Balzaretti, 2021] for GGG on TiO_2, a bidentated and a monodentated configuration, respectively. The bidentated configuration consists of both ends of the molecule, i.e., the phosphate and the carboxylic groups being absorbed onto the slab surface, either in the x direction (Bid-X) or the y direction (Bid-Y). The monodentated configuration depends on the absorption of either the phosphate group (P) end or the carboxylic group (C) end onto the surface, being called P-vertical (P-ver.) and C-vertical (C-ver.), respectively. When the central amino group in the GGG molecule also contributes to the adsorption modes, these are called P-step and C-step, correspondingly. Figure 4.10 illustrates these configurations.

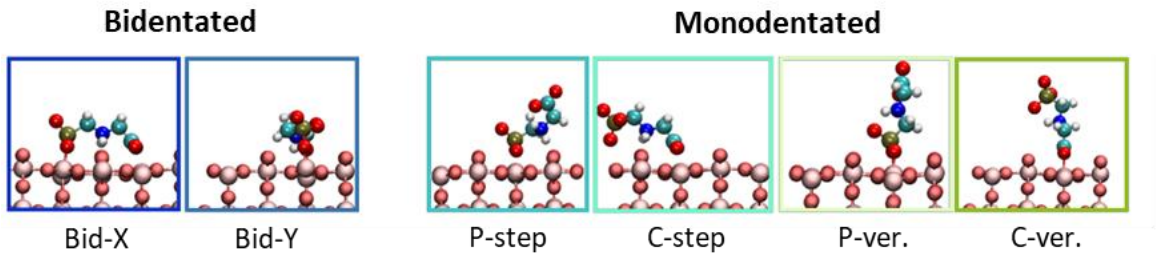

Figure 4.10. Adsorption configurations sorted by bidentated and monodentated modes are illustrated from left to right: Bid-X, Bid-Y, P-step, C-step, P-ver., and C-ver. Adapted/Reproduced based on the Creative Commons conditions [Balzaretti, 2021].

To define the type of absorption configuration, the following protocol designed by Maria von Einem was employed:

1. Assurance of the surface absorption.
   To determine if GGG is being adsorbed or not, the parameter *d* was defined by taking the distance from the P or C2 atoms to the closest atom in the slab, either zinc or oxygen.
   If *d* is lower than 3.5 Å, GGG is considered as adsorbed.

2. Identification of adsorption type: bidentate, step or vertical.
   For this purpose, the angle formed between vectors $\vec{a}$ and $\vec{b}$ to the z-axis ($\measuredangle \gamma$) is divided into 30, 60, and 90°, as illustrated in Figure 4.11a.
   Depending on which of these segments the measured angle lies, it is classified as bidentate ($0^o \leq \measuredangle \gamma \leq 30^o$), step ($30^o \leq \measuredangle \gamma \leq 60^o$), or vertical ($60^o \leq \measuredangle \gamma \leq 90^o$) adsorption.

3. If bidentate, definition of type: Bid-X or Bid-Y.
   To establish Bid-X or Bid-Y adsorption, the angle formed between the xy plane was segmented into two equal parts (see Figure 4.11b).
   If the measured angle lies in the first segment ($0^o \leq \measuredangle \alpha \leq 45^o$) the adsorption is classified as Bid-X, in the other case ($45^o \leq \measuredangle \alpha \leq 90^o$) as Bid-Y.

4. If step or vertical, definition of type: C or P.
   They are defined by measuring their distance to the surface.
   If the distance from the C2 atom to the ZnO slab is larger than the distance from the P atom, the absorption is classified as P-ver, in the other case as C-ver.

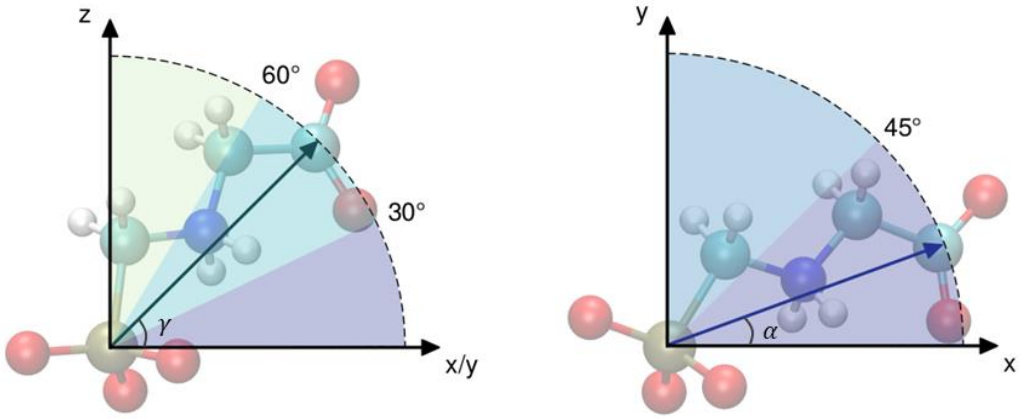

(a) (b)

Figure 4.11. Schematic representation of angles to classify the GGG adsorption configuration. Images created by Maria von Einem (reproduced with permission).

4.2 Experimental methods

4.2.1 ZnO-NWs sample fabrication

ZnO nanowires (ZnO-NWs) were synthesized using the wet-chemical deposition method reported by Guo et al. [Guo, 2005]. The nanowire-array layers are deposited on ITO substrates in two steps, first, the seed layer deposition, and second, the growth process itself.

For the seed layer, a solution of 1.3 g of zinc acetate dihydrate (Sigma-Aldrich) and 10 ml of ethanol is prepared and mixed. After 20 minutes, three drops of diethanolamine as a stabilizer are slowly added. Meanwhile, the ITO substrates are cut (1.5 x 1.5 cm approximately) and cleaned in an ultrasonic bath at 50 W with deionized water, acetone, and isopropanol for cycles of 10 minutes, respectively.

The solution is deposited on the substrates by *spin coating* at 10 V (6000 rpm) for 40 s using an electric-motor spinner of LAIDEA. Afterwards, the substrates are annealed at 500 °C for 2 hours using a Prendo MF-3R oven.

Two solutions of 9.6 g of potassium hydroxide and 6 g of zinc nitrate hexahydrate (both of Sigma-Aldrich) are prepared for the growth process. Once both solutions are completely dissolved and transparent, the potassium hydroxide blend is poured quickly into the zinc nitrate solution, making sure that the combined exothermic solution becomes completely transparent again. Subsequently, it is mixed for 20 minutes and placed into a chemical bath using glass beakers, as shown in Figure 4.12. The samples coated with the seed layer are placed upside-down into the solution by using a holder. Subsequently, both the beaker containing the samples and the bigger one for the bath are covered with aluminum foil.

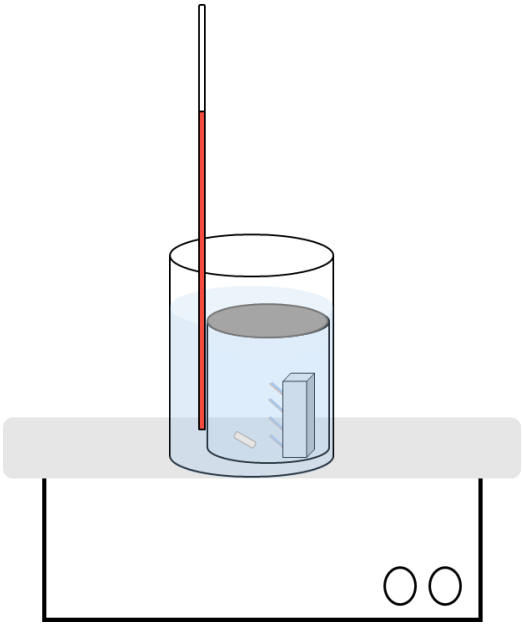

Figure 4.12. Schematic representation of the chemical bath for the ZnO-NWs growth process.

The heating is carried out under constant stirring until reaching 80 °C for 20 minutes. Finally, the samples are taken out of the beaker, cleaned with deionized water, and dried.

4.2.2 Glyphosate layers

Glyphosate was purchased from Sigma-Aldrich Chemical Co.

Three different GGG solutions were prepared in D.I. water and deposited on the nanostructures by *spin coating* at 7.6 V (5000 rpm) for 45 s using the electric-motor spinner of LAIDEA.

In this work, the same concentrations as having been reported by Seemann [Seemann, 2018] are used to homogenize results and complement the discussion. The concentrations are given in Table 4.2.

Table 4.2. Glyphosate concentrations in mass fractions ("percentage of weight") using D. I. water as solvent.

Label	GGG concentration
i	1.50 wt%
ii	1.24 wt%
iii	1.01 wt%

4.2.3 Device fabrication

Structure I

The first device architecture consists of a metal-semiconductor heterojunction based on nanostructured ZnO layers deposited on ITO as described in the previous section. For our analysis, samples with two different seed-layer conditions are fabricated on 1 mm glass substrates in order to optimize the ZnO thickness. Two samples with this structure were fabricated, Structure Ia with a seed-layer concentration of 130 g/l, and Structure Ib with a lower concentration, i.e., 65 g/l.

After the seed layer deposition, the samples are annealed at 500 °C for 2 hours. Gold electrodes were thermally evaporated on the ZnO surface using a shadow mask and a Denton Desk V evaporator at 40 A for 130 s. Figure 4.13 illustrates a schematic representation of such a structure.

Figure 4.13. Device I schematic representation. The difference between Structure Ia and Ib lies in the concentration of the ZnO deposited layer.

Structure II

Device structure II consists of ZnO-NWs grown on ITO substrates as described in section 4.2.1., both plain and functionalized with glyphosate layers on the surface. Figure 4.14 shows a schematic representation of its architecture, while Table 4.3 describes its functionalization with the herbicide.

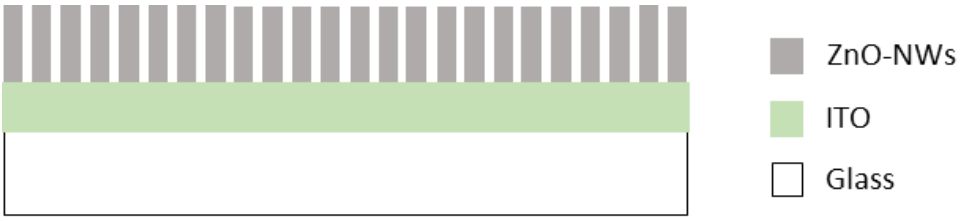

Figure 4.14. Schematic representation of Structure II.

Table 4.3. Devices structure II, plain and functionalized with glyphosate layers on the surface. Glyphosate concentrations in mass fractions ("percentage of weight") using D. I. water as solvent.

Label	Description of the device
ZN	Plain ZnO-NWs
ZGi	ZnO-NWs with 1.50 wt%
ZGii	ZnO-NWs with 1.24 wt%
ZGiii	ZnO-NWs with 1.01 wt%

Structure III

Structure III consists of a prefabricated TFT purchased from Fraunhofer IPMS (Dresden, Germany). The structure comprises a heavily n-doped silicon wafer as a common gate electrode with a 230 nm thick thermally grown SiO_2 dielectric layer and 16 transistors per substrate. The source and drain contacts are interdigitated structures (10 nm ITO, 60 nm Au) with channel lengths L = 10 and 20 μm, respectively, and a channel width W = 1 cm. All the transistors in the substrate have a coplanar bottom-gate contact configuration with upper source and drain electrodes.

Structure III is submitted to a cleaning process in an ultrasonic bath at 50 W with deionized acetone and isopropanol for cycles of 10 minutes, respectively. Afterwards, a 65 g/l solution of the seed-layer previously described is deposited on the structure by *spin coating* at 10 V (6000 rpm) for 45 s. Finally, the device is annealed at 500 ℃ for 2 hours. Figure 4.15 illustrates the structure of device III.

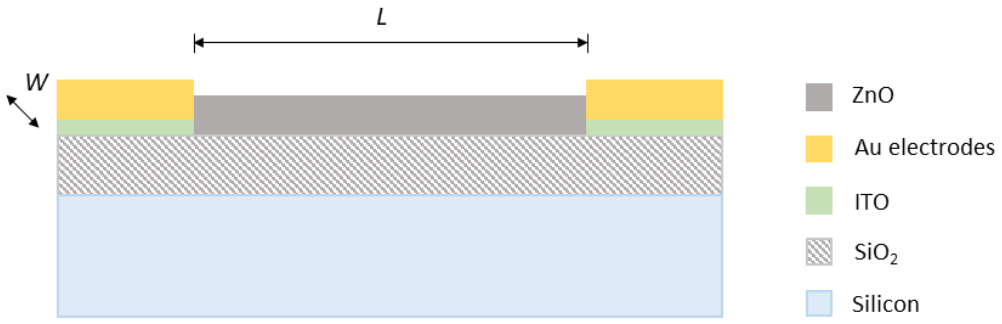

Figure 4.15. Device III schematic representation.

A glyphosate solution in D.I water with a concentration of 1.01 wt% is deposited on the device by *spin coating* at 7.6 V (5000 rpm) for 45 s. Afterwards, the device is annealed at 80 °C for 10 minutes to get rid of the water.

4.2.4 Characterization techniques

The techniques used to study the ZnO/GGG interface are scanning electron microscopy, energy dispersive x-ray spectroscopy, UV-Vis spectrometry, and current-voltage characteristics.

4.2.4.1 Scanning electron microscopy

Scanning electron microscopy (SEM) is a structural characterization technique that employs an electron beam for sample surface imaging. The image formation depends on the acquisition of signals produced from sample-electron beam interactions [Zhou, 2007].

Figure 4.16 shows a schematic representation of a SEM column. Electrons are emitted from a filament, later bundled, and accelerated by a cathode and an anode [Seemann, 2018]. The electron beam is focused on the sample surface by a set of electromagnetic lenses in the column.

Depending on the position of the electron beam, two types of electrons are typically detected: Backscattering electrons (BSe) and secondary electrons (SE), providing different kinds of information. BSe originates from elastic scattering, whereas SE comes from inelastic scattering.

BSe can help to analyse variation in the sample's composition since the number of BSe detected is proportional to the atomic number. This dependence is useful to differentiate between faces, SE are surface sensitive. Therefore, they can be used to analyze the topology of the sample [Zhou, 2007].

The SEM technique is used to determine the thickness of the layers presented in Structures I and III. For Structure II, SEM gave information on the topography and morphology of the nanostructures grown and their changes in the presence of the different GGG concentrations.

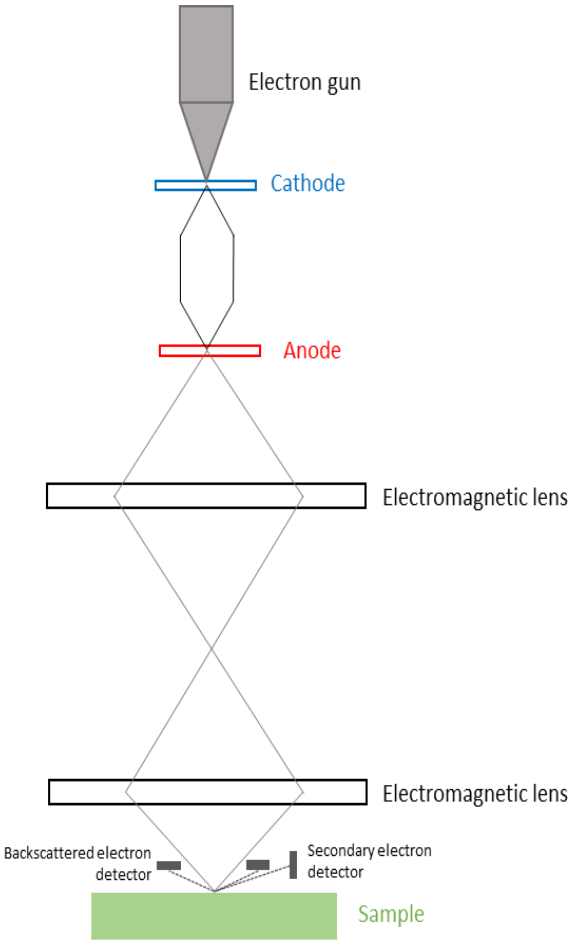

Figure 4.16. Schematic representation of a scanning electron microscope.

The SEM images presented in this work are taken at the Microscopy Laboratory (LaMic) of ENES Morelia using the JSM-IT300 scanning electron microscope.

4.2.4.2 Energy dispersive x-ray spectroscopy

Energy dispersive x-ray spectroscopy (EDX) is an analytical technique used for elemental analysis and chemical composition determination [Torres-Rivero, 2020].

EDX is based on the generation of characteristic x-rays. Characteristic x-rays are emitted when an external high-energy electron collides with an inner shell electron, being both ejected and leaving a vacancy in the shell of the atom. This vacancy is filled by an outer shell electron and accompanied by a loss of energy, emitted as an x-ray photon of characteristic transition energy for this process.

For each characteristic x-ray emitted, an element is associated. Chemical elements are identified from a specific energy peak and its content by its integrated intensity. In this work, EDX was used to identify and quantify the elements in the different device structures.

4.2.4.3 UV-Vis spectroscopy

UV-Vis is a spectroscopic technique employed to quantitatively measure the light absorbance of a sample by measuring the intensity of light that passes through the sample with respect to the intensity of light passing a reference sample or blank.

Figure 4.17 illustrates the principal components of a UV-Vis spectrophotometer. A light beam is expanded from the visible to the UV range by a dispersion device. An exit slit is used to separate monochromatic beam out of the spectrum with an initial intensity I_o, passing then through the sample, and a detector measures a final intensity I.

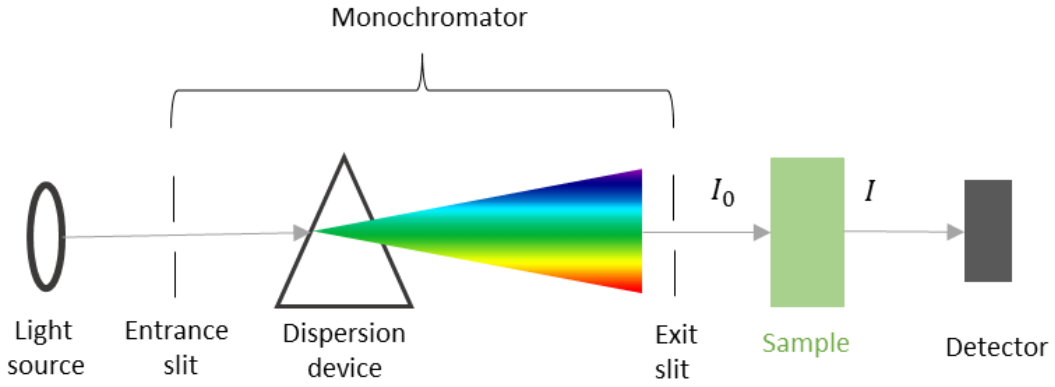

Figure 4.17. Schematic representation of a UV-Vis spectrometer.

The absorbance (A) is calculated by equation (1).

$$A = log\ \frac{I_0}{I} \qquad (1)$$

In this work, UV-Vis spectroscopy is used to monitor the absorbance changes on ZnO-NWs by adding the previously mentioned GGG concentrations.

The absorption spectra are obtained in the 300-1110 nm range using the Thermo Scientific Genesys 10S – UV-Vis spectrophotometer of the National Laboratory for Ecological Analysis and Synthesis (LANASE), ENES Morelia.

4.2.4.4 Current-voltage (I-V) characteristics

The I-V characteristics is a graphical method used to represent the connection between the voltage applied across an electrical device and the current flowing through it. It is useful to analyze the charge transport mechanisms, and to extract information about the built-in potential barriers formed at the interfaces.

I-V characteristics of Structure I are measured using the SMU 2400 from Keithley Instruments of LAIDEA in a reverse and forward sweep from -6 V to 6 V. This enables the determination of the type and quality of the contact formed between gold and ZnO. Figure 4.18 illustrates the arrangement of the measurement.

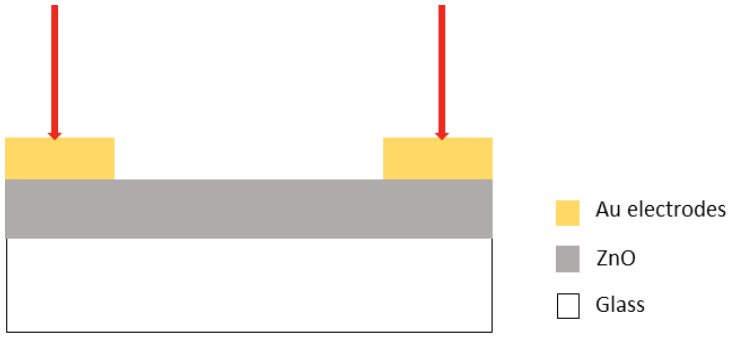

Figure 4.18. Schematic representation of the electrical connection for Structure I. Tips are shown in red.

The devices on ITO corresponding to Structure II were also measured under the same conditions. Herein, the ITO substrate was used as common bottom contact, whereas silver ink coupled with a mask to prevent the embedding effect is used as top contact (see Figures 4.19a and 4.19b).

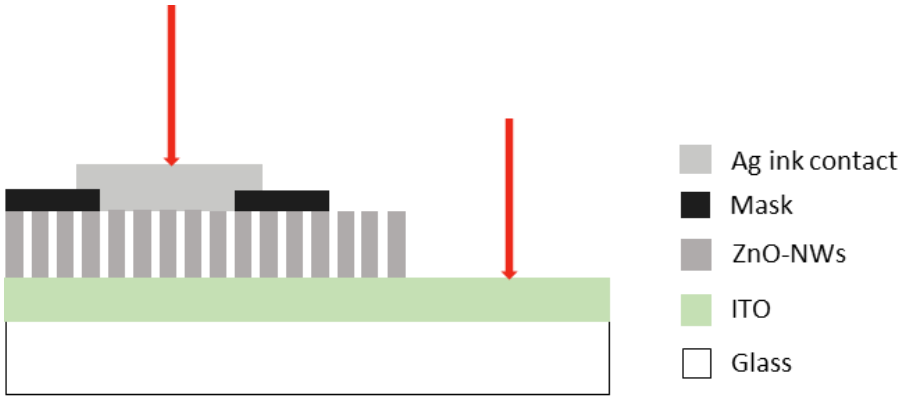

Figure 4.19a. Schematic representation of the electrical connection for device ZN.

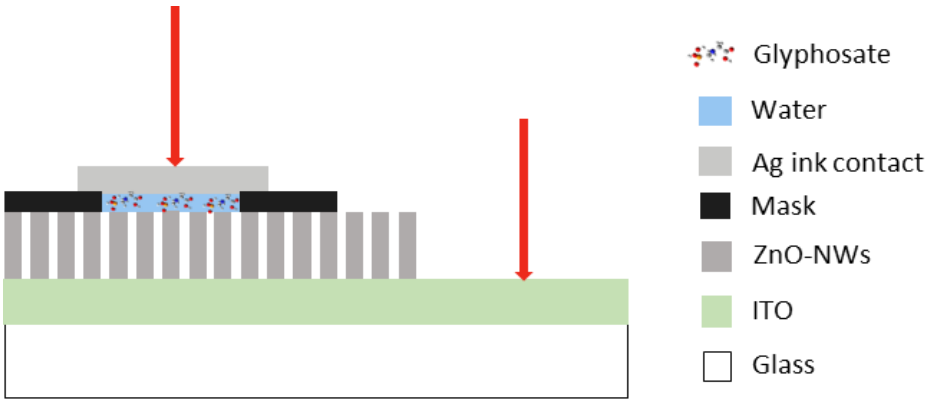

Figure 4.19b. Schematic representation of the electrical connection for devices ZGi, ZGii and ZGiii.

Finally, the prefabricated device corresponding to Structure III is analyzed electrically. The transistor characteristics are measured as illustrated in Figure 4.20. A gate voltage (V_{GS}) from -4 to +4 V is applied to induce a channel current in the semiconductor through the field effect, while a source-drain voltage (V_{DS}) from -4 to +4 V was applied to the channel.

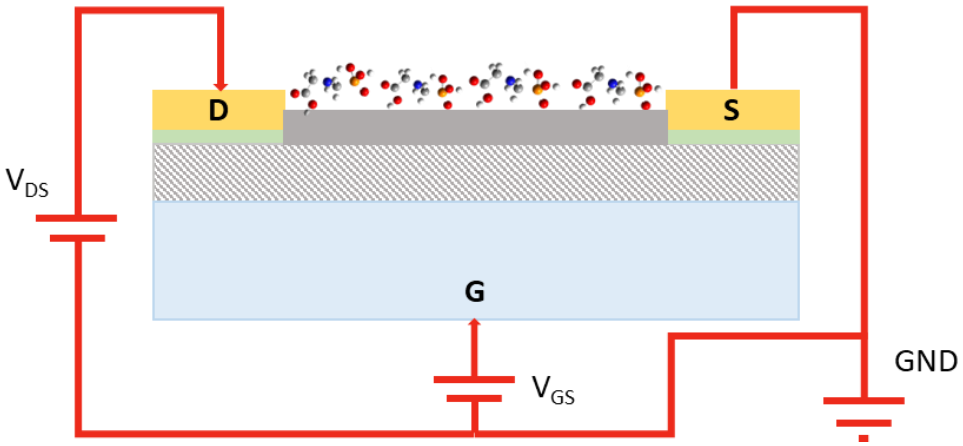

Figure 4.20. Schematic representation of the electrical polarization for the device Structure III.

5 Results and Discussion

In this chapter, the obtained results are presented and discussed. The first section presents the theoretical calculations which have been made in cooperation with the HMI-group, Uni-Bremen, particularly along the Molecular Dynamics research line of Dr. Susan Köppen, under direct supervision of PhD. candidate Maria von Einem. This section presents the discussion of water on ZnO, as well as the adsorption configurations for GGG on the semiconductor, i.e., direct and indirect. Furthermore, an energetic discussion of the GGG/ZnO system is given.

Section 5.2 deals with the experimental results. The findings of three different device structures are presented and discussed. For Structures I, SEM and current-voltage techniques were used to determine the layer thicknesses and the electric contact type, respectively.

Devices with a larger surface detection area, i.e., Structure II were submitted to a morphological and chemical determination analysis through SEM and EDX spectroscopy. Moreover, optically by UV-Vis spectroscopy and electrically by I-V characteristics.

Structure III was studied through SEM-EDX to estimate the layer thickness and the device's composition. Finally, electrically to determine the device response with and without glyphosate.

5.1 Theoretical calculations

5.1.1 Water on ZnO

Simulation AR, i.e. reference simulation (see Table 4.1), was performed to analyze the attachment of water molecules on the ZnO slab. The adsorption could be observed using the VMD tool to show molecules at a certain distance from the slab.

Considering that the water molecule has a diameter of about 2.7 Å, three lengths of 4, 6 and 8 A are chosen as different distances from the slab to analyze their interaction dynamics for a running time. Figures 5.1, 5.2 and 5.3 show snapshots from the MD production run at time zero (t = 0 ns) and different from zero (t ≠ 0 ns).

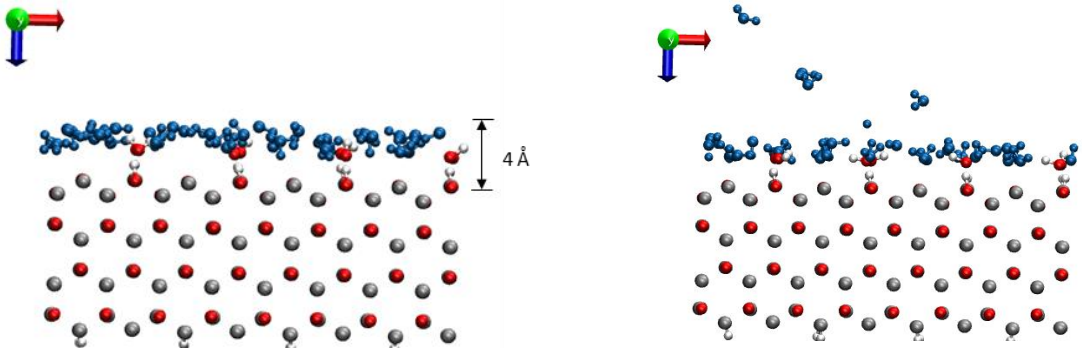

(a) (b)

Figure 5.1. Snapshots of the AR simulation showing a 4 Å distance from the water molecules (blue) to the ZnO slab (a) at the beginning of the simulation t = 0 ns, and (b) their distribution at t ≠ 0 ns.

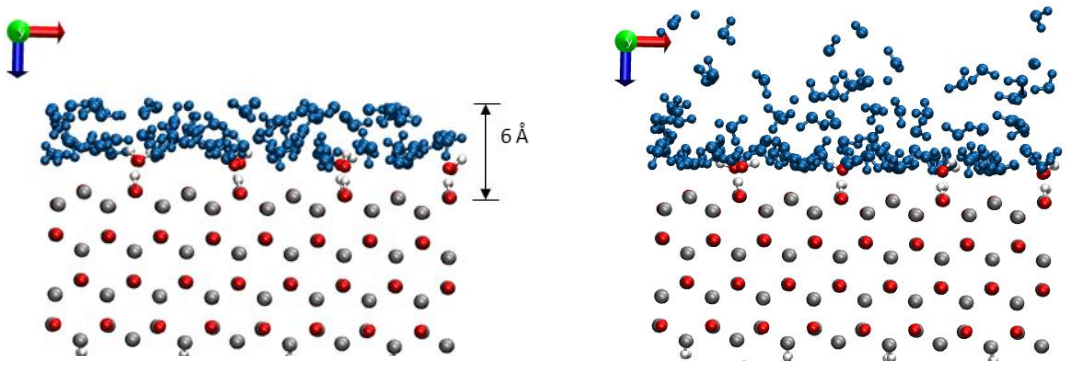

(a) (b)

Figure 5.2. Snapshots of the AR simulation showing a 6 Å distance from the water molecules (blue) to the ZnO slab (a) at the beginning of the simulation t = 0 ns, and (b) their distribution at t ≠ 0 ns.

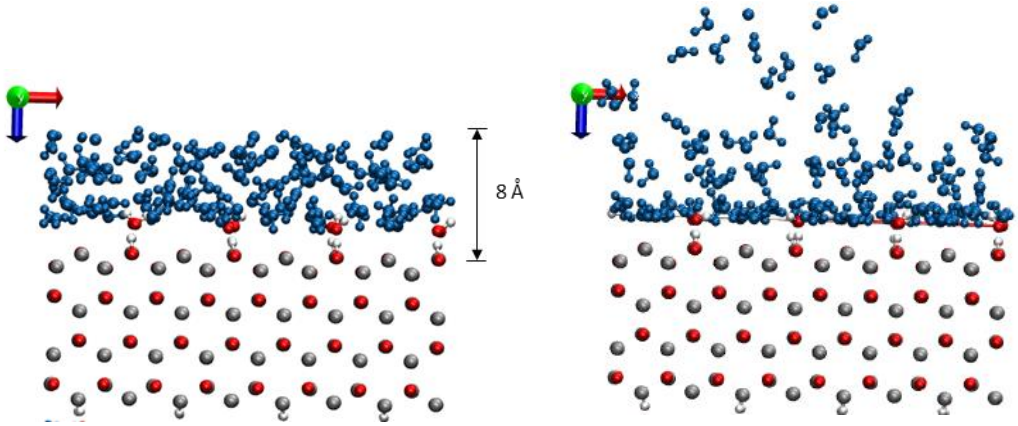

(a) (b)

Figure 5.3. Snapshots of the AR simulation showing a 8 Å distance from the water molecules (blue) to the ZnO slab (a) at the beginning of the simulation t = 0 ns, and (b) their distribution at t ≠ 0 ns.

As the MD simulation starts running, some of the water molecules within these set distances move away from them as depicted in Figures 5.1-3(b). Nevertheless, from the snapshots, it can still be observed a strongly adsorbed water layer to the surface. This result suggests that water molecules adhere strongly to the ZnO slab in our system, thus representing a barrier for the GGG molecules, which they must overcome to be adsorbed on the semiconductor surface.

To understand how water is attached to the ZnO surface, we analyzed the water atoms density, i.e., oxygen (OW) and hydrogen (HW1 and HW2) atoms through the cell, see Figure 5.4. As illustrated in the zoom-in figure, the analysis is focused near the semiconductor surface, approximately one diameter of a water molecule. At this distance, three zones were studied.

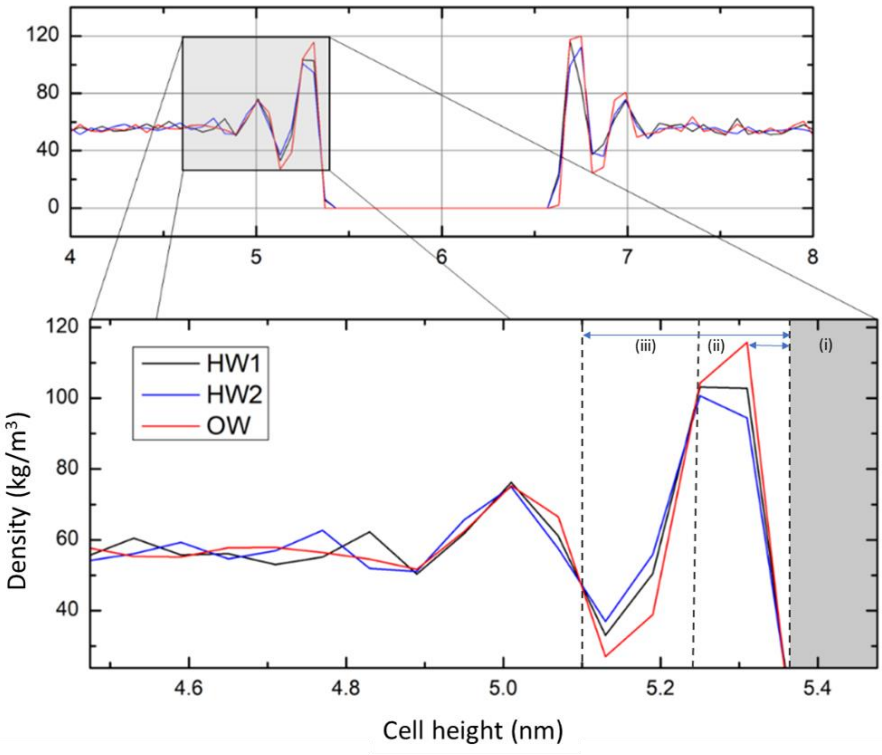

Figure 5.4. Density profile of the oxygen (OW) and hydrogen (HW1 and HW2) atoms of water over the cell height. Elaborated with data from the AR molecular dynamics simulation.

For zone (i) no H_2O molecules were found since the ZnO slab lies at this height of the cell. At zone (ii), the maximum density value corresponds to the oxygen atoms, OW (red line), followed by the hydrogens HW1 and HW2, respectively. Moreover, at approximately 5.3 nm, the density values decrease, but the tendency $\rho_{OW} > \rho_{HW1} > \rho_{HW2}$ persists. Such a decrement can be attributed to the presence of the carboxyl groups belonging to the ZnO slab. Conversely, for zone (iii), such a density order is inverted, and the highest density values correspond to the hydrogens.

These findings suggest that the oxygen atoms, rather than the hydrogen ones, are closer to the ZnO surface which yields the suggestion of geometry attachment as depicted in Figure 5.5, similar to the previously reported by Große Holthaus et al [Große Holthaus, 2012] for water on ZnO $(1\bar{2}10)$. There, through DFT calculations it was found that water molecules form hydrogen bonds with OH groups attached on ZnO.

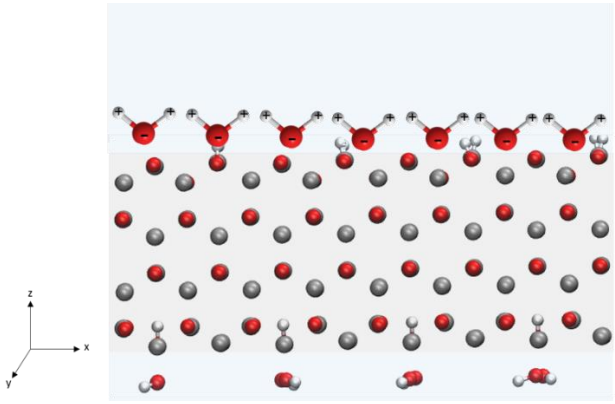

Figure 5.5. Schematic representation of water molecules attached to ZnO slab.

5.1.2 Adsorption configurations

In this section, the absorption of GGG on ZnO is discussed. From the two simulation protocols presented in section 4.1.2, two different adsorption configurations were obtained. Procedure type A corresponds to an indirect adsorption while procedure type B to a direct adsorption.

Indirect adsorption

As mentioned in section 5.1.1, the water molecules' strong attachment to the ZnO slab presents a barrier for GGG to be adsorbed directly to the slab. A consistent result was obtained when simulations A1 and A2 (GGG molecules randomly rotated) were performed.

Figure 5.6 shows a snapshot of A1 simulation with a water layer thickness of 4 Å, for which it is notable how the GGG molecules cannot directly access the surface. However, despite this shielding, the GGG molecules feel attracted to the semiconductor´s surface, thus becoming adhered to this first water layer on the slab.

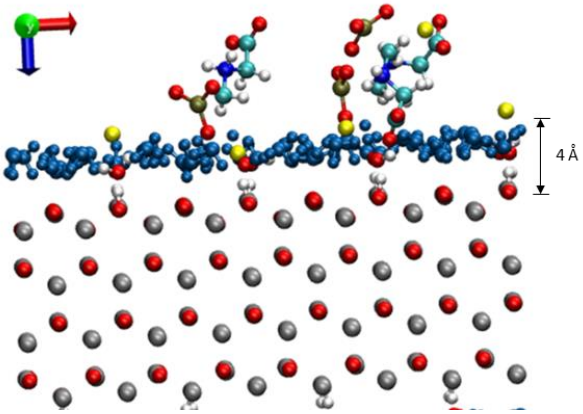

Figure 5.6. Snapshot from A1 simulation after a 110 ns production showing GGG and a 4 Å water layer thickness. Yellow – Na^+, the same color coding for the atoms as in Figures 4.1 and 4.2 is applied

Furthermore, the Na^+ ions added to neutralize the total charge of the system (details in section 4.1.2), depicted as yellow balls in the figure are close to the surface, intend to penetrate this H_2O layer. This behavior could be attributed to two phenomena: The diffusion of ions in solution, specifically for the case of Na^+ in water, a diffusion coefficient value of 1.334 x 10^9 m^2/s is reported in the literature [Samson, 2003]. And the positively charged sodium atoms, which tend to neutralize themselves by coupling to an electronegatively charged oxygen atom, for instance, from the water layer attached to the ZnO surface.

Additionally, for the indirect adsorption procedure, GGG clustering was observed (see Figure 5.7), since the protonation state of GGG at pH~7 is 2- and this charge is localized at the phosphonate and carboxylic groups, the Na+ ions tend to be closer to these functional groups.

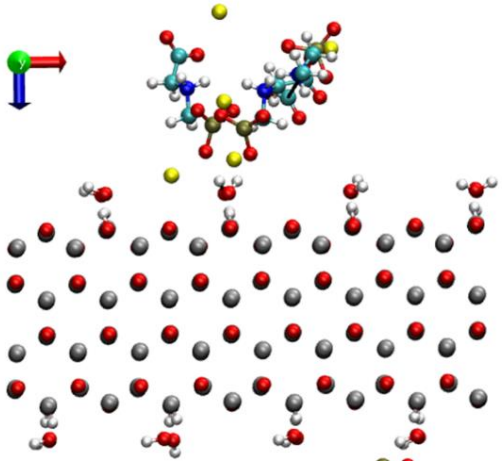

Figure 5.7. Snapshot from A2 simulation after a 110 ns production showing GGG clustering. Water molecules were hidden to focus the reader's attention on GGG molecules and Na^+ ions.

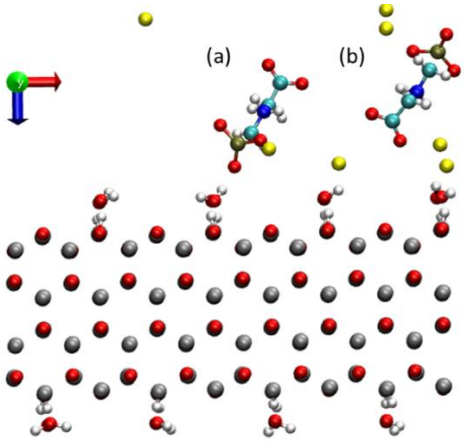

Figure 5.8. Snapshots from A2 simulation after a 110 ns production. A propensity from the carboxyl and phosphate groups to attach on ZnO is noted. Water molecules were hidden.

Although it cannot be considered as adsorption, since the glyphosate molecules are located at a distance of at least 3.5 Å, we can observe in Figure 5.8 two interesting "indirect adsorption modes".
Figure 5.8 (a) shows the GGG phosphonate side proximate to the surface. Clearly, the phosphonate group of the GGG feels more attracted to the ZnO slab than the carboxyl group (Figure 5.8b). We can attribute this preferential behavior to the charge density in the molecule, at a 7 pH environment GGG has a -2 net charge (see Figure 2.2) located at the phosphonate and carboxylic groups

Direct adsorption

For procedure B, direct adsorption of GGG on ZnO was possible to obtain and classify though the procedure presented in section 4.1.4.

The results demonstrate that the bidentate configuration dominates in the system. Both cases, Bid-X and Bid-Y, were found during the MD simulations. Figure 5.9 shows a top view of the B1 system after a 110 ns MD simulation. From this position, we noticed how two molecules are attached in the x-direction, whereas the other two prefer the y-direction. Figure 5.10 shows the bidentated configurations from a side view.

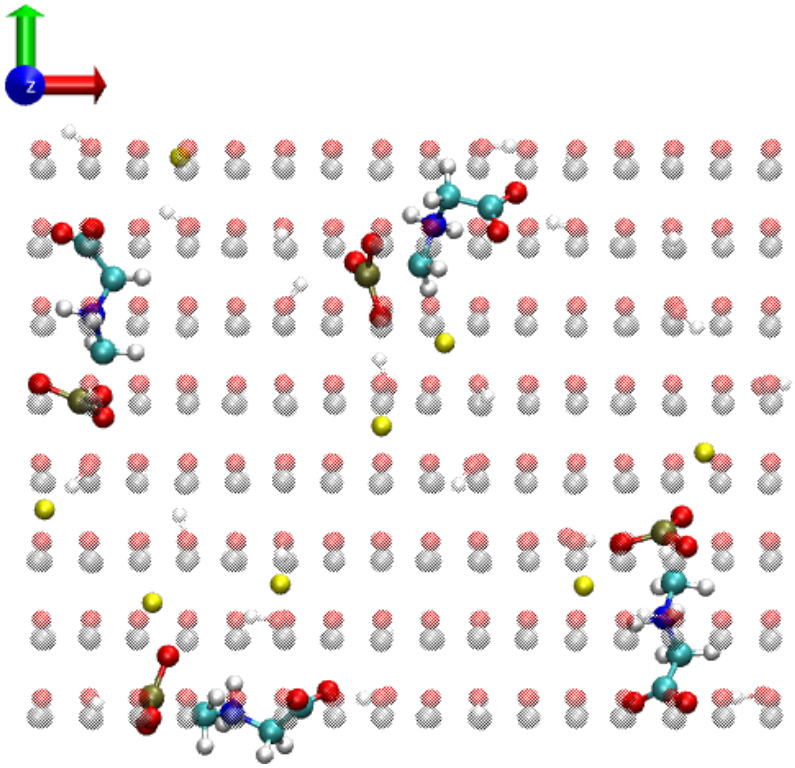

Figure 5.9. Snapshot top view of simulation B1 after 110 ns.

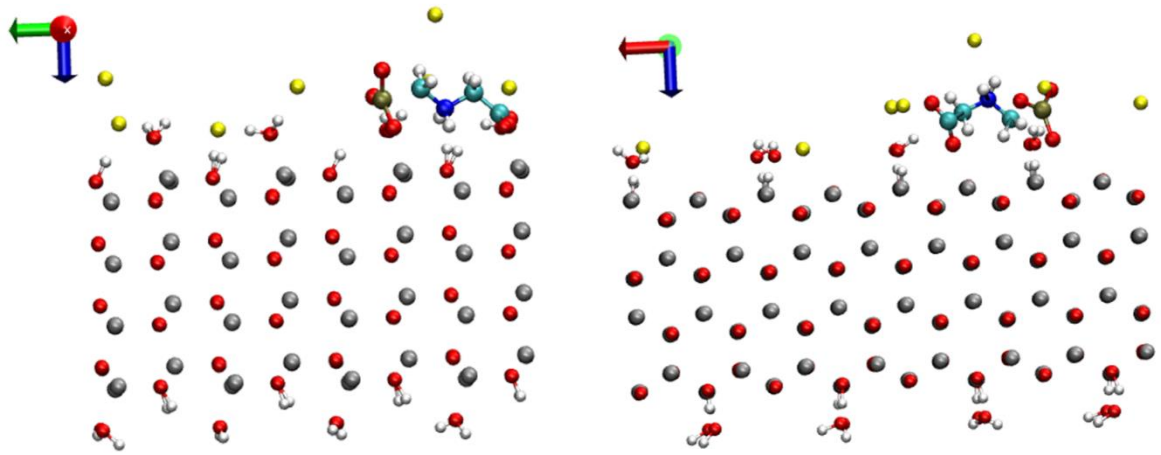

(a) (b)

Figure 5.10. Snapshots of B1 simulation after 110 ns MD simulation, Bid-X (a) and Bid-Y (b) adsorption configurations. Water molecules and the other GGG molecules were hidden on purpose to focus the reader's attention on just one GGG molecule.

In Figures 5.11-5.13, the distribution for the adsorption modes presented in section 4.1.4 for the four GGG molecules (a), and its time evolution over a 110 ns production run (b) are plotted for B1, B2 and B3, respectively.

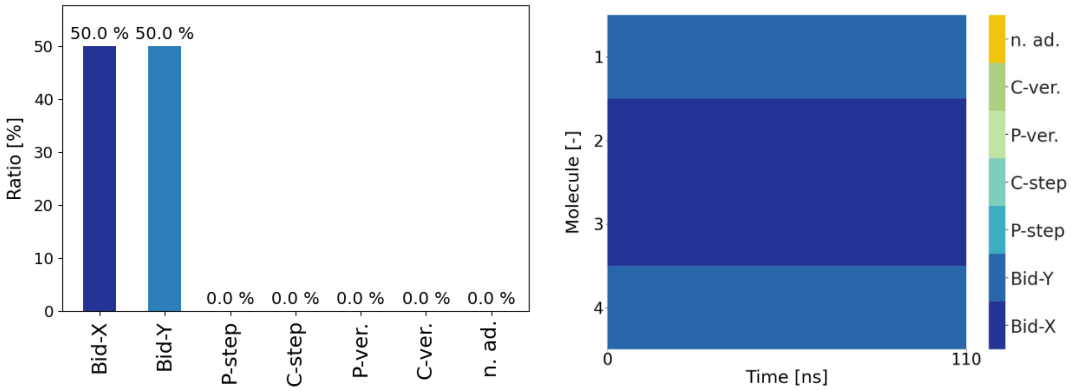

(a) (b)

Figure 5.11. Distribution (a) and time evolution (b) of the adsorption modes for simulation B1. Evaluated from 4 GGG molecules for a simulation time of 110 ns.

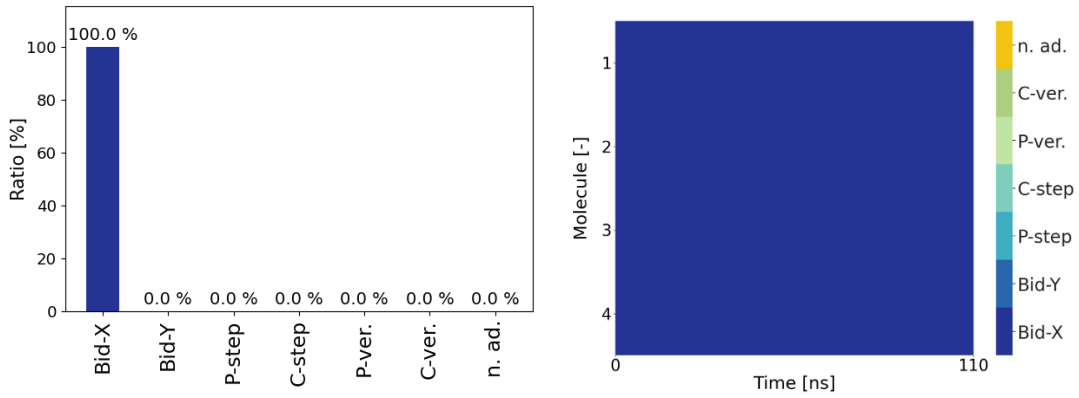

(a) (b)

Figure 5.12. Distribution (a) and time evolution (b) of the adsorption modes for simulations B2. Evaluated from 4 GGG molecules for a simulation time of 110 ns.

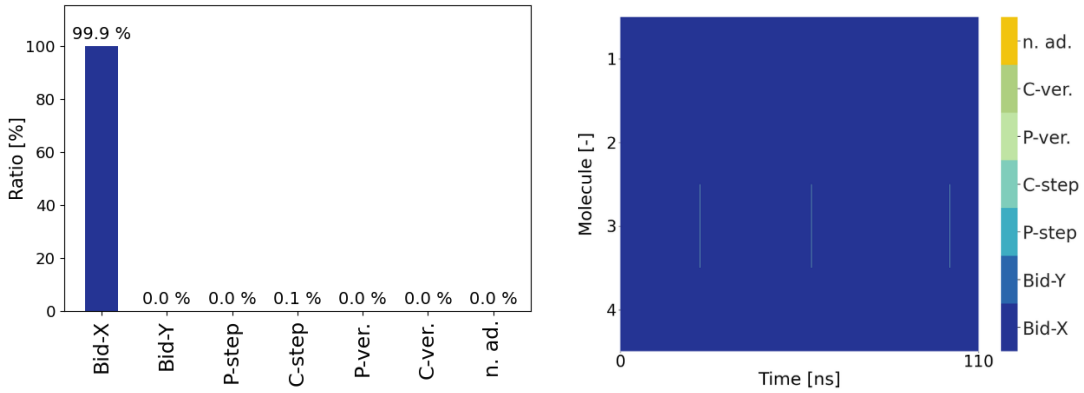

(a) (b)

Figure 5.13. Distribution (a) and time evolution (b) of the adsorption modes for simulation B3. Evaluated from 4 GGG molecules for a simulation time of 110 ns.

These results show two important aspects. One, Bid-X configuration dominates for direct adsorption. Two, once the GGG molecules are attached to the ZnO, they maintain an equilibrated position over time.

Similar results were found for simulations with preferent starting configurations, i.e., P-down and COOH-down. For the P-down simulation with the phosphate group closer to the slab, Bid-X was the preferred and stable configuration (see Figure 5.14). On the contrary, for simulation where the carboxyl group was settled closer to the slab, Bid-Y adsorbance of two molecules was observed at the beginning of the simulation (see Figure 5.15). Nevertheless, after approximately 25 ns, this configuration tends to change to the Bid-X.

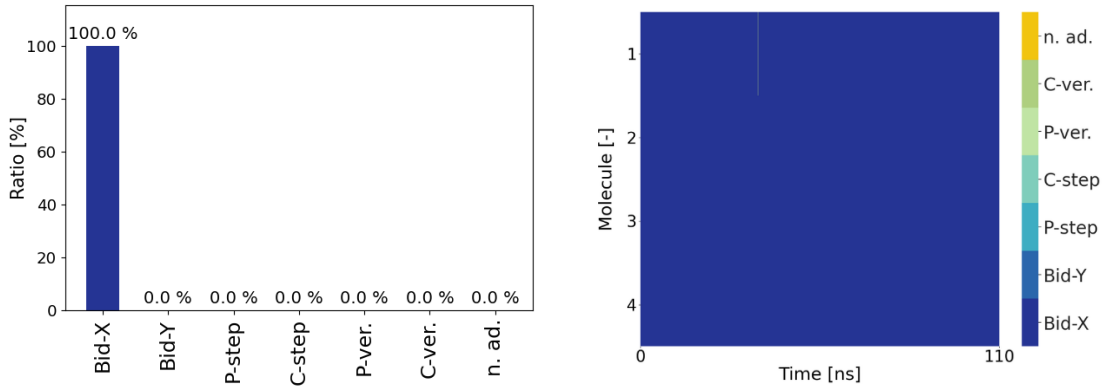

(a) (b)

Figure 5.14. Distribution (a) and time evolution (b) of the adsorption modes for simulation P-down. Evaluated from 4 GGG molecules for a simulation time of 110 ns.

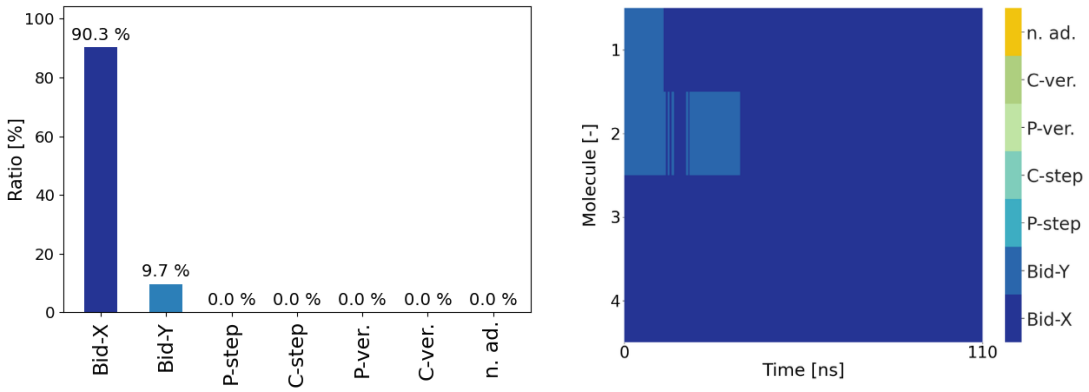

(a) (b)

Figure 5.15. Distribution (a) and time evolution (b) of the adsorption modes for simulation COOH-down. Evaluated from 4 GGG molecules for a simulation time of 110 ns.

The MD simulations for procedure type B suggest that glyphosate adsorbs on the semiconductor surface, and that the preferent adsorption mechanism for our system is the Bid-X. A similar result was reported by Balzaretti [Balzaretti, 2021] for GGG on a TiO_2 rutile-(110) surface. For their system, GGG showed high adsorption in the bidentated perpendicular mode, which can be compared to our Bid-X configuration.

5.1.3 Energetic discussion of GGG on ZnO

Giving an assertive definition of energy has been one of the most debated topics in physics. The Britanica encyclopedia define it as "the capacity of doing work" [Britannica, 2021], a non-precise definition. Nevertheless, as a matter of fact, energy is conserved in closed systems.

Energy in a closed system is the contribution from various sources, e.g., velocity and position of the particles. Mathematically, we can express it in the following way:

$$\Delta E = K + V = 0 \tag{1}$$

$$\Delta E = \frac{1}{2}mv^2 + mgh \tag{1.1}$$

where the term K in eq. (1) corresponds to the kinetic energy, defined as half of an object´s mass (m) multiplied by the velocity squared (v). As it is clearly seen, the kinetic energy contribution is always a positive value. The latest term stands for the potential energy.
As aforementioned, a force field describes the potential energy for a system. By using GROMACS tools it was possible to compute the total (ΔE) and potential energies (V) over time of the whole system. In our case, conformed with four GGG molecules, ZnO slab, eight Na^+ ions and water.

For the calculation protocols followed in this work, i.e., direct and indirect, we obtained higher total energy values for indirect rather than for direct adsorption (see Figure 5.16), with a difference of 6.41 eV approximately. This can be explained by the fact that the direct procedure comprehends a double energy minimization. Since type A atoms are less restricted in movement, therefore the whole system would possess a higher value of total energy.

Furthermore, the potential energies over time were also obtained. Figure 5.17 shows a similar tendency of higher values for the indirect adsorption. Here, the low value of the potential energy for the indirect adsorption indicates that between A and B protocols, B is the most stable. Such a difference was calculated to be 7.13 eV approximately.

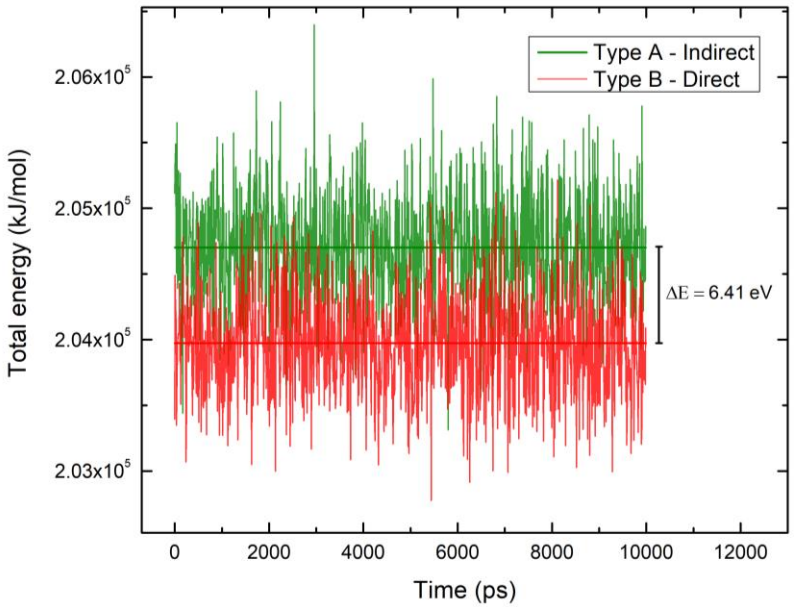

Figure 5.16. Evolution of the total energy in MD simulations of direct and indirect adsorptions. ΔE is the difference in total energy of the system between procedures A and B.

By following equation (1.1), the contributions of V and K were calculated for each protocol. The resulting energy differences are reported in Table 5.1. It can be observed how the contributions of both potential and kinetic energies have similar values for the two protocols. The main energy contribution in the systems is attributed to be potential, and only a small fraction to be kinetic (~ 7%).

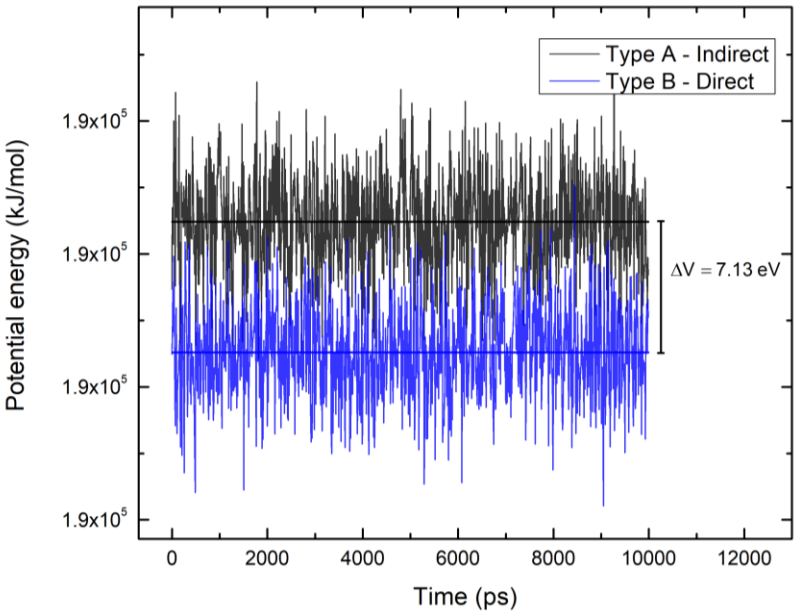

Figure 5.17. Evolution of the potential energy in MD simulations of direct and indirect adsorptions. ΔV is the difference in total energy of the system between procedures A and B.

Table 5.1. Energetic contribution for one simulation of procedure type A and B.

Energy (kJ/mol)	Type A	%		Type B	%
Total	204,596.8 ∓ 5.7			203,977.9 ∓ 1.1	
Potential	189,870.2 ∓ 5.6	92.80%		189,182.1 ∓ 1.1	92.75%
Kinetic	14,726.56 ∓ 0.36	7.20%		14,795.80 ∓ 0.53	7.25%

In Figure 5.18, the results obtained from the MD simulations are summarized.

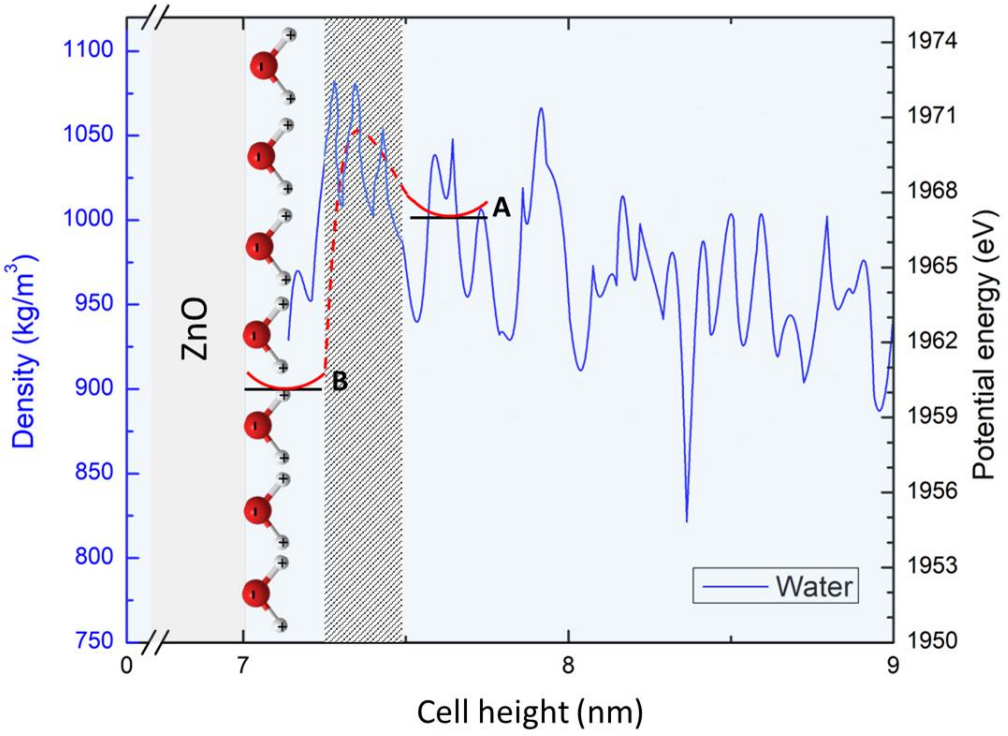

Figure 5.18. Schematic representation of potential energy for protocols A and B. Water density profile over the cell height from AR simulation.

The water density profile over the cell height shows a strong attachment of water molecules to the ZnO slab, representing an obstacle for the GGG molecules to reach the semiconductor surface. Furthermore, by focusing on this first hydrating layer, and based on our analysis, a geometry attachment of the H_2O molecules is depicted.

Moreover, the figure illustrates the potential energy values obtained for the indirect (type A) and direct (B) protocols. The energy value for the indirect procedure leads us to conclude two important points: (i) The direct adsorption (type B) is the most favorable procedure; and

(ii) the energetic difference in between is of 7 eV. Notice that with the calculation methodology followed in this work it is not possible to determine how such a difference in energy behaves (red dashed line in Figure 5.18). However, we should understand this value as a contribution of all the atoms in the system, i.e., in our case, the four GGG molecules, water molecules, eight Na^+ ions and the ZnO surface.
Further investigation needs to be done to complement our results with the use of other computational techniques. E.g., with the nudged elastic band (NBE) technique it is possible to evaluate the energy barrier of a reaction by inputting two stable configurations [Henkelman, 2000]; and with DFT calculations to determine if chemical reaction, for example, degradation effects.

5.2 Experimental results

5.2.1 Structure I

SEM and I-V characteristics were used to determine the layer thickness and the type of electric contacts observed for the devices of the Structure I type (details of structure see 4.2.3).

5.2.1.1 SEM

To estimate the layer´s thicknesses through SEM, Structures I were placed parallelly to the electron beam as shown in Figure 5.19. Although, this is not a common set up to analyze samples in this equipment, due to the nature of our thin layers and type of materials used, the glass substrate got overcharged on the surface preventing the visibility of the image. To address it, a grating and a tape made of copper were connected to the samples to discharge them.

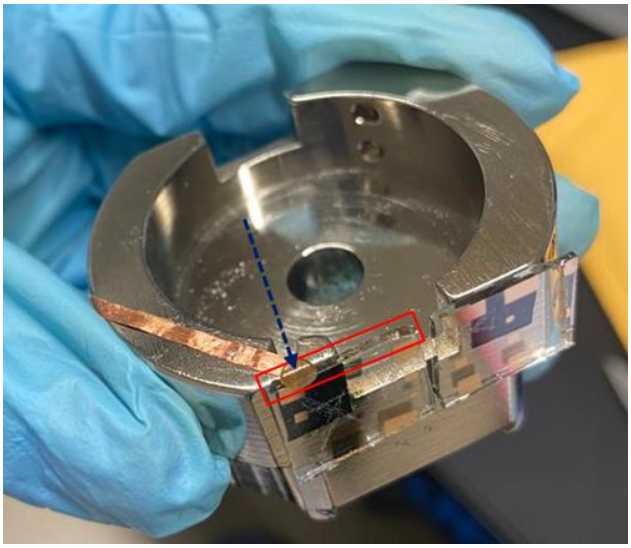

Figure 5.19 Special sample holder preparation for SEM to characterize Structure I. The sample holder is placed parallelly to the electron beam (blue arrow). The analyzed section of the sample is outlined in red.

Figure 5.20 shows an SEM micrograph of device Structure Ia, i.e., with a seed-layer concentration of 130 g/l. The approximate thicknesses found to amount to 64 nm for ZnO, and to 27 nm for the Au contact layers. For Structure Ib, i.e., with a seed-layer concentration of 65 g/l, the thickness for ZnO was found to be 33 nm while being 31 nm for Au (see Figure 5.21).

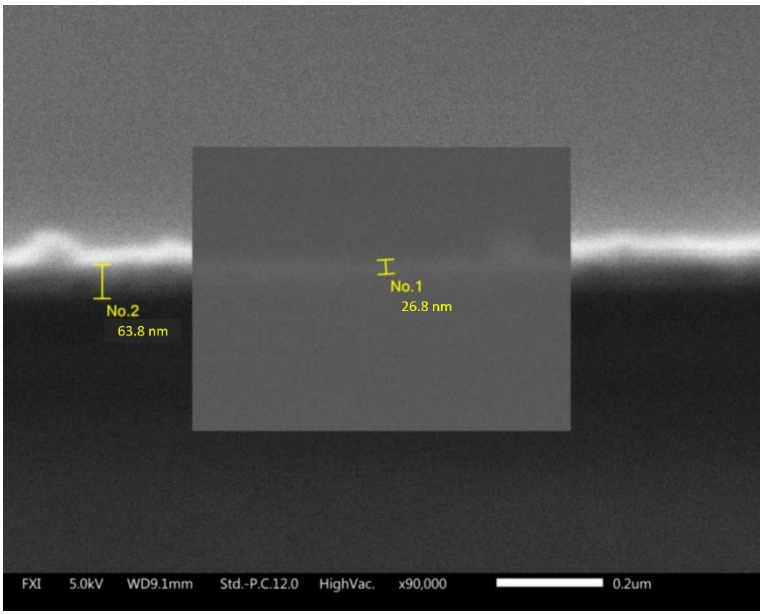

Figure 5.20. SEM measurement of the Structure Ia device. The yellow bars indicate the thickness of each layer, No. 1 for Au, and No. 2 for ZnO.

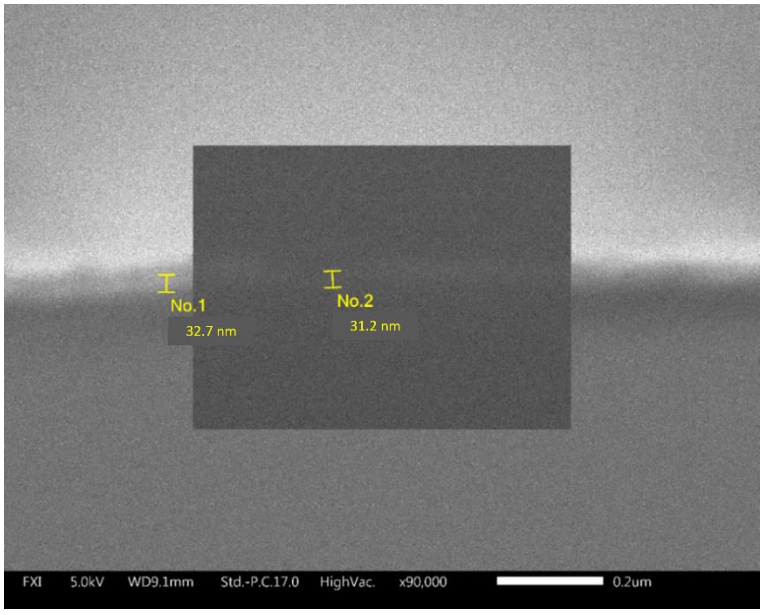

Figure 5.21. SEM measurement of the Structure Ib device. The yellow bars indicate the thickness of each layer, No. 1 for Au, and No. 2 for ZnO.

For the development of electronic devices, the determination of layer thickness is an important parameter to understand the device's electrical transport type, mechanism, and stability. We observed that under the same fabrication conditions, it is possible to decrease the ZnO thickness by halving the seed layer's concentration. Despite its obviousness, the definition of this procedure is an important result for LAIDEA-UNAM in the development of ZnO thin-films for low-cost devices, particularly TFTs for sensing applications. However, to better estimate the thickness-concentration relationship, more specialized techniques that allow for the analysis of surfaces on a nanometric scale are proposed to be applied, for instance, atomic force microscopy (AFM).

5.2.1.2 I-V characteristics

I-V measurements under forward and reverse bias were recorded to analyze the type of electric contact formed at the ZnO/Au interface.

Since ZnO is a natural n-type semiconductor with an E_F of around -4 eV depending on the fabrication process [Bley, 2016], and Au has a work function of -5.1 eV [Ofuonye, 2014], the case of $\phi_m > \phi_s$ is expected, i.e., a Schottky junction. However, an ohmic behaviour was observed for this device as shown in Figure 5.22, indicating that $E_{F_{ZnO}}$ for our process is more negative, resembling more to that of bulk ZnO (-5.2 eV) [Tada, 2000]. Notice that different values for $E_{F_{ZnO}}$ have been reported in literature, from -3.9 eV for pc-ZnO nanolayers fabricated by pulsed-laser deposition [Sharma, 2015], up to -5.57 eV for ZnO QDs synthetized by hydrolysis [Ghosh, 2012].

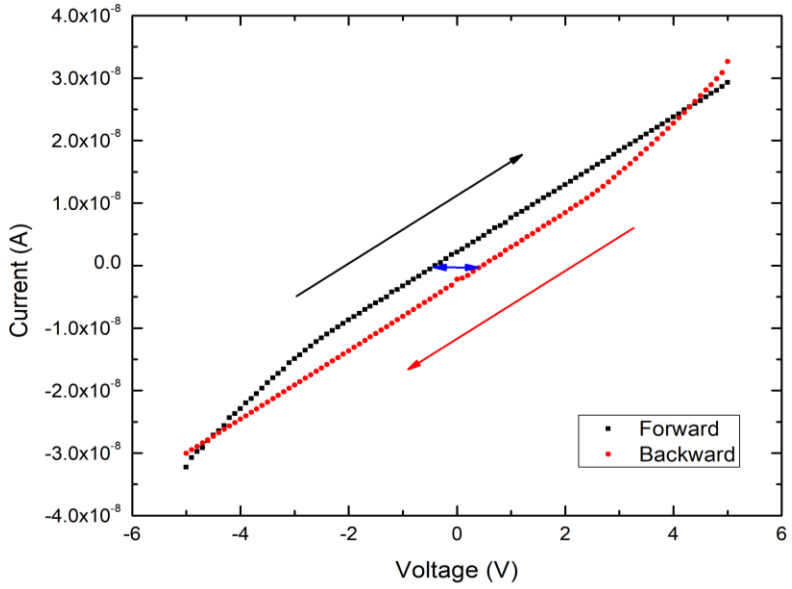

Figure 5.22. I-V characteristics in forward and reverse of device Structure I.

In the I-V characteristics of Structure I, a hysteresis effect can be observed, described by a shift of 0.82 V at the abscissa for the current recorded in backward direction (from positive to negative bias) with respect to the initial sweep in forward (from negative to positive bias).

This effect has been observed in materials, particularly in bulk or nanostructured ZnO, grown by different techniques [Li, 2013]. It is well known that the oxygen chemisorption at the ZnO surface causes a depletion layer and an upward band bending by capturing electrons in a region near the surface, which causes a shift in the current [Liao, 2007]. In other words, such a shift is due to the modification of the work function of the ZnO array caused by the oxygen atom vacancy filling occurring mainly at the surface [Bao, 2015].

5.2.2 Structure II

In devices based on Structure II, ZnO NWs were grown on ITO as previously described in section 4.2.1 with the aim to increment the surface area of the devices, i.e., the detection area for the sensors.

The devices were analyzed through SEM, EDX, UV-Vis and electrically (I-V). SEM coupled with EDX allowed for a morphological analysis as well as for the determination and quantification of their chemical composition, respectively. Through UV-Vis spectroscopy the absorbance of plain ZnO-NW samples as well as that of those functionalized with GGG was analyzed.

5.2.2.1 SEM

The dimensions of the ZnO-NW arrays for devices presented in Table 4.3 were estimated using SEM. Values between 120-180 nm in diameter, ~ 4 μm in height, and an aspect ratios of ~ 25 were found.
Figures 5.23a,b and 5.23c show Device ZN nanowires from a top and front view, respectively. A NW high density and a uniform growth can be seen in the micrographs.

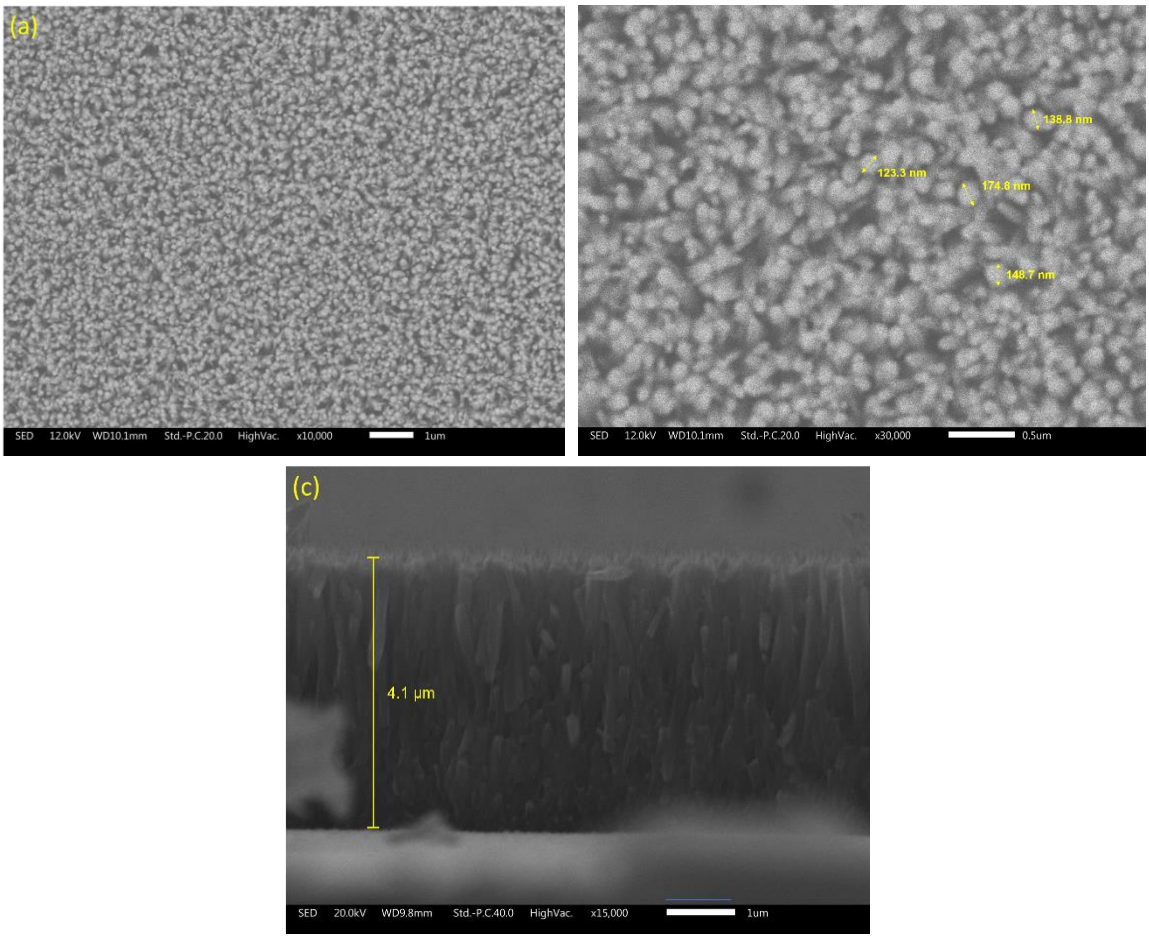

Figure 5.23. SEM measurements in SED mode of Device ZN from a top (a), (b) and front view (c). The yellow bars in (b) indicate the approximately NW diameters.

Due to the insulating properties of the herbicide [Seemann, 2018], the functionalized samples (i.e. ZGi, ZGii and ZGiii) had to be coated with a gold layer of 18 nm approximately for the SEM analysis. The detailed description of the samples is listed in Table 4.2.

The surface of device ZGi is shown in Figure 5.24 through a SEM micrograph. Superposed, a grain with approximate dimensions of 32 x 27 μm^2 was found. To verify its composition, different spots (shown as blue crosses in the figure) were analyzed by EDX. Spots 1 and 2 located on the surface of the grain indicate the presence of nitrogen, phosphate, and carbon atoms which belong to the chemical composition of the herbicide. This suggests that the bulky grains observed on the surface of the sample correspond to non-dissolved GGG clusters. For spots 3 and 4 outside the grains, mass fractions of zinc and oxygen were found most probably caused during the nanowire's growth process. Table 5.2 lists the composition found for each spot.

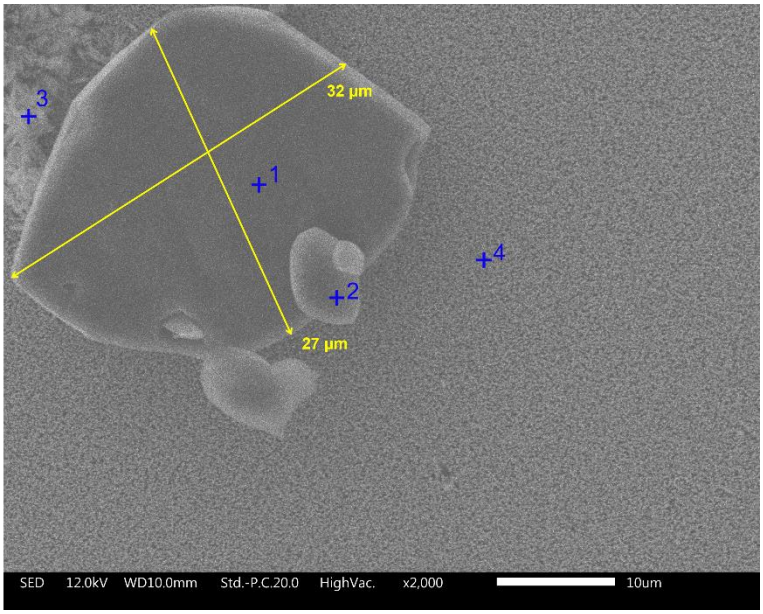

Figure 5.24. SEM measurements in SED mode of sample ZGi, position of the analyzed spots by EDX are indicated in blue crosses.

Table 5.2. Results of the composition analysis of the positions shown in Figure 5.24. Results are given as mass fractions.

Analyzed spot	**Found composition (wt %)**				
	Zn	O	P	C	N
1	-	43.8	23.5	23.4	9.3
2	2.6	43	22.2	23.8	8.3
3	83.9	16.1	-	-	-
4	85.3	14.7	-	-	-

For device structure ZGii, with a lower concentration of GGG, a similar result was found. SEM images showed grains of the herbicide but with smaller dimensions (see Figure 5.25). EDX at spots 1 and 2 indicate the presence of elements belonging to the chemical composition of GGG in similar proportions as listed in Table 5.3. Interestingly, spots 3 and 4, in neighbor grains, do not show GGG traces. Instead, we found indications which suggest them to be composed of ZnO (see Table 5.3). This result might be attributed to two scenarios due to the size of the grains: (i) that the larger atomic mass of zinc leading to a strong EDX signal weakens the EDX signal of phosphorous and nitrogen, thus, showing the ZnO

composition only; or (ii) that during the spin coating of the GGG solution on the ZnO NW arrays, the grains rotated in a way that traces of the nanostructures got stuck on their surface.

Spot 5 shows the presence of Zn, O, P, and Au. Gold is attributed to the layer coated on the surface for SEM analysis, while P suggests the presence of glyphosate. Notice that EDX can just detect phosphorous from GGG because it is the heaviest atom of this molecule. Zinc and oxygen seem to have weakened the signals of carbon and nitrogen. Table 5.3 reports the composition analysis of sample ZGii for spots marked as blue crosses in Figure 5.25.

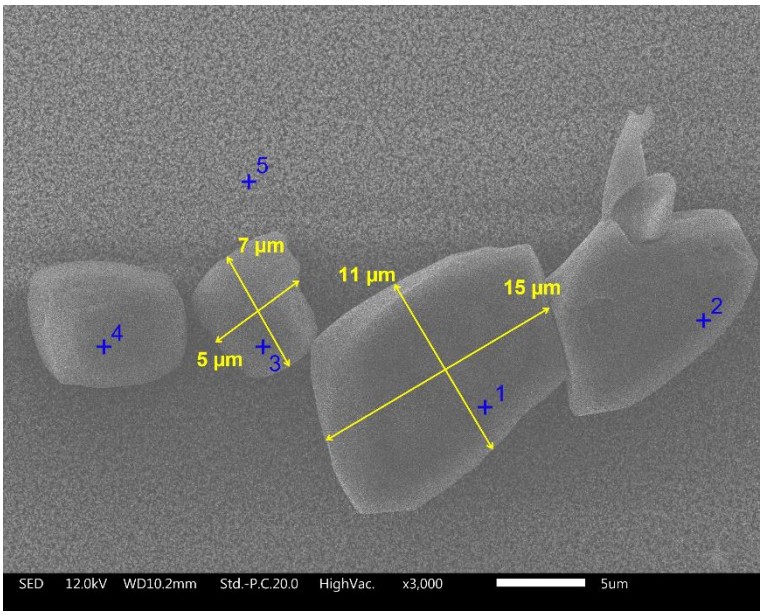

Figure 5.25. SEM measurements in SED mode of sample ZGii, position of the analyzed spots by EDX are indicated in blue crosses.

Table 5.3. Results of the composition analysis of the positions shown in Figure 5.25. Results are given as mass fractions.

Analyzed spot	**Found composition (wt. %)**					
	Zn	O	P	C	N	Au
1		43.7	22.2	23.8	10.3	-
2	1.1	43.3	20.9	24.8	9.9	-
3	84.7	15.3	-	-	-	-
4	83.9	16.1	-	-	-	-
5	72.8	15	1.0	-	-	11.1

For the device structure ZGiii with the lowest GGG concentration, a nonhomogeneous layer on the ZnO-NW array was found, see Figures 5.26a-b. Through an EDX analysis of the specific positions indicated as blue crosses in Figure 5.26b, the presence of P, C, and N was detected, as listed in Table 5.4. This result demonstrates that GGG films (with a lower wt%) cover and embed the ZnO-NW arrays, and therefore, functionalize them.

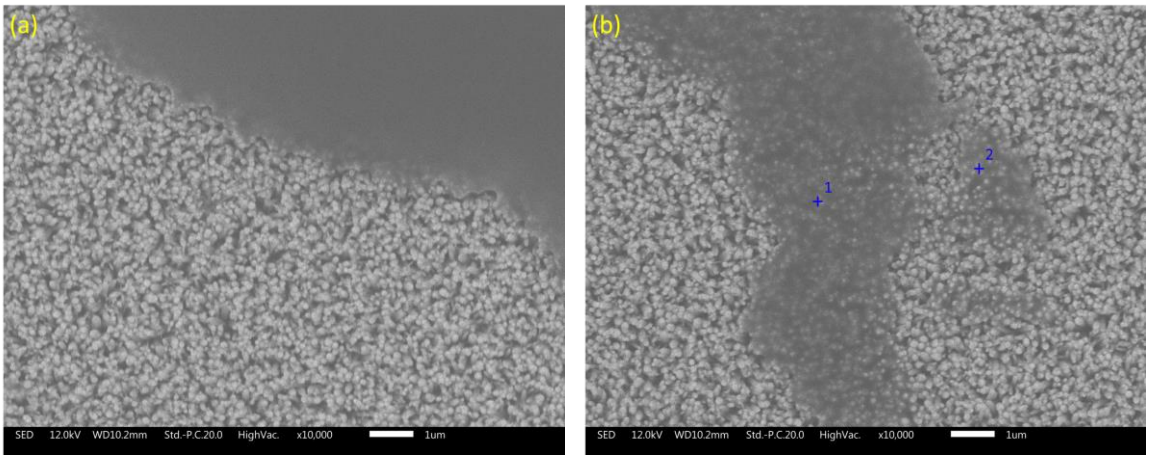

Figure 5.26. SEM measurements in SED mode of sample ZGiii (a). Position of the spots analyzed by EDX indicated by blue crosses (b).

Table 5.4. Results of the composition analysis of the positions shown in Figure 5.26b. Results are given as mass fractions.

Analyzed spot	**Found composition (wt %)**				
	Zn	O	P	C	N
1	83.8	14.5	0.4	1.1	0.1
2	83.4	14.8	0.6	1.2	-

5.2.2.2 UV-Vis spectroscopy

The absorbance spectra of both pure ZnO NWs and ZnO NWs coated with GGG (devices ZN and ZGi-iii, respectively) were measured on the day of deposition and three days after.

Figure 5.27 shows the absorbance spectrum of the plain ZnO NW array sample measured on the day of growth (thick black line). ZnO's main characteristic absorbance peak can be observed in the UV region, around 365 nm, as reported for bulk [Sun, 2011].

To verify our result, absorbance is compared to other deposition methods reported in the literature, where a maximum peak for the characteristic region of ZnO has been reported as 355 nm and 359 nm, for thin films fabricated by metal-organic vapor phase epitaxial growth (MOVPE) [Park, 2001] and pulsed-laser deposition (PLD) [Nasser, 2021], respectively, the latter being process which is highly controlled. For nanoparticles with diameters in the range of 30-90 nm synthesized by a sol-gel method, the absorption characteristic peak of ZnO is reported at 378 nm. These ranges are in good agreement with the absorbance spectrum of our samples, which shows a second peak at 378 nm, exactly as for the mentioned nanoparticles. However, this is a low energy value for the band edge. Thus, it cannot be attributed to the nanoparticles, but to the development of shallow levels inside the band gap due to the presence of impurities in the lattice [Pudukudy, 2015].

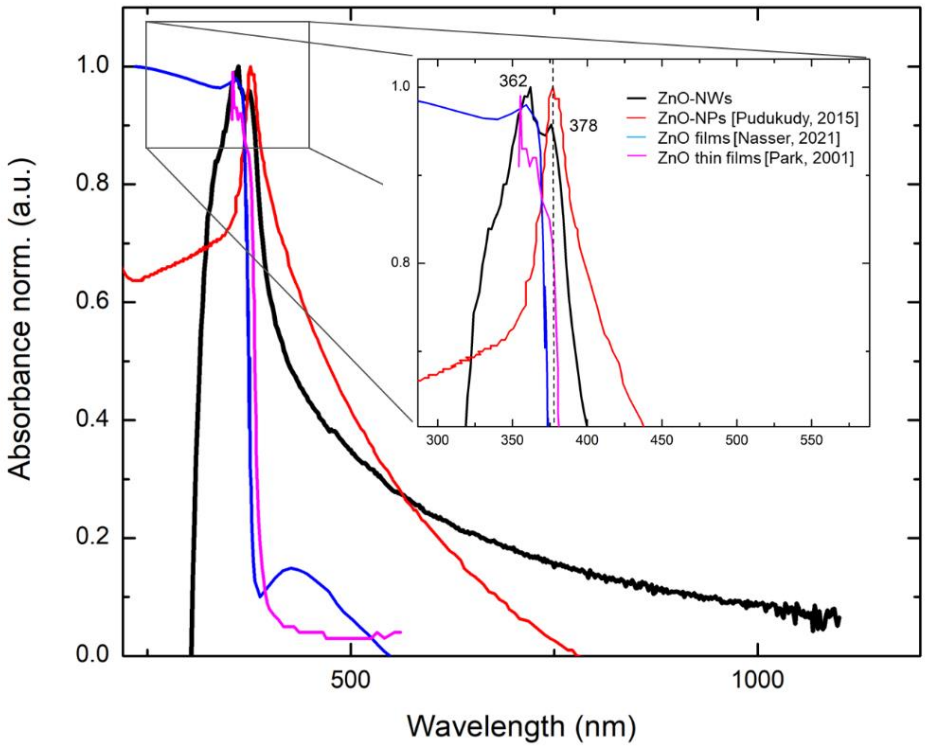

Figure 5.27. Comparison of the absorbance spectrum of our ZnO-NWs (thick black line) with spectra reported for and ZnO nanoparticles (red line), ZnO films fabricated by PLD (blue line), and thin films fabricated by MOVPE (pink line).

The fresh devices of nanowire arrays coated with GGG (ZGi-iii) were also measured. Again, the characteristic ZnO absorbance peak is present in the UV region for all the devices as shown in Figure 5.28a, and the presence of GGG on ZnO is mainly observed to affect the spectra in the range from 400 nm onwards, particularly up to 800 nm. To verify the absorbance effect of GGG in the samples, a close-up plot was obtained by subtracting the spectrum of plain ZnO-NWs from those of the functionalized samples, see Figure 5.28b. A similar behavior is observed for samples i and ii with higher concentrations, which can be

related to the presence of grains on the surface of both Devices ZGi and ZGii. For Device ZGiii a much stronger and completely deviating change of the absorbance is observed which can be attributed to the action of a closed GGG film on the nanowires.

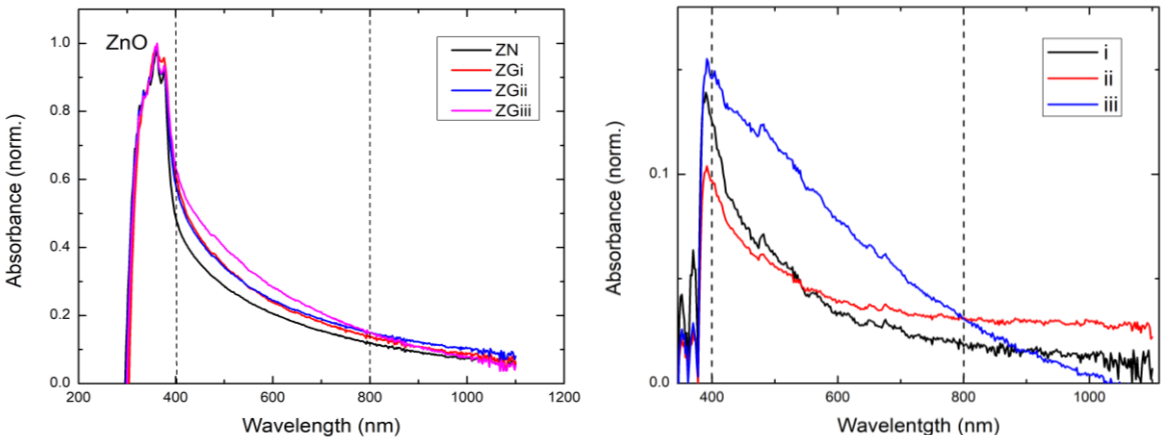

(a) (b)

Figure 5.28. (a) Absorbance spectra of both plain ZnO-NWs and coated with glyphosate under different concentrations on day 1. (b) Absorbance spectra of i-iii GGG concentrations on ZnO-NWs.

After three days, the absorbance of devices ZN and ZGi-iii shows a decrease in the visible region, Figure 5.29. A similar behavior was reported by Páez et al. for ZnO-NPs and glyphosate solutions; they observed a reduction in its absorbance spectra, which indicates a decrease in the concentration of the herbicide and, therefore, glyphosate´s degradation. Furthermore, the authors mentioned that GGG adsorption on the nanoparticles suggested to be the most important removal mechanism of the agrochemical [Páez, 2019]. Based on this, our results could indicate the herbicide degradation on our ZnO NW arrays.

To further verify the three-day degradation effect, the integrated area of the absorbance spectra has been calculated in the range from 400 to 1000 nm where the decrease is significant, Figure 5.30.

Due to the nature of ZnO, atom vacancies on the surface are left after its growth process, which creates surface states that easily attach OH radicals and environmental molecules. Its presence modifies the optical characteristics of ZnO, explaining the degradation effect of ZnO itself; the difference in the integrated area after three days, observed for Device ZN. Notice that for samples where GGG was deposited, the degradation effect is more evident, particularly for Device ZGiii, i.e., that with glyphosate in lower concentration and films layer on the nanowires. This result suggests the potential application of ZnO for GGG degradation in water. Further investigation needs to be done to verify the extend of ZnO as a degradant agent of GGG. The study of this phenomenon is out of the scope of this research; however, it is indeed a crucial aspect to be considered for the development of a sensor since this result reflects a potential of this structures not only to detect GGG but also to degrade it .

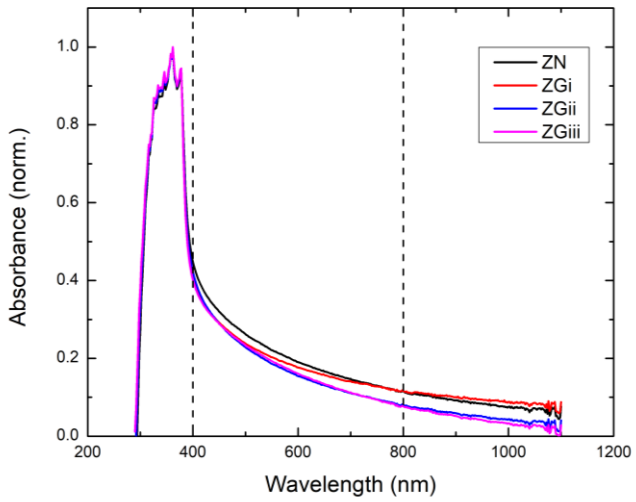

Figure 5.29. Absorbance spectra of both plain ZnO-NWs and coated with glyphosate under different concentrations on day 3.

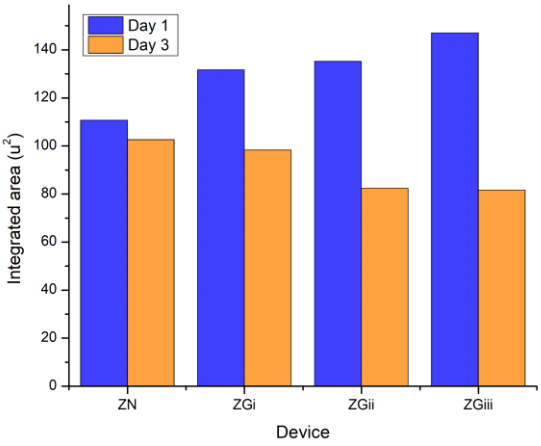

Figure 5.30. Degradation of GGG by ZnO. Integrated area over 400-1000 nm from Figures 5.28a and 5.27.

5.2.2.3 I-V characteristics

Figure 5.31 shows the current-voltage characteristics of the devices ZN, ZGi, ZGii, and ZGiii measured as described in section 4.2.4.4, using silver ink as the top contact.

ZnO with a bandgap energy of 3.37 eV is contacted with ITO (ϕ_{ITO}= 5.1 eV) on the bottom and with Ag on the top which has a work function of 4.73 eV [Dweydari, 1975]. Our results shown in Fig. 5.31a for plain NW ZnO are consistent with previous reports [Bley, 2016, Castro, 2021 and Manzo, 2021]. Both metal contacts follow the condition $\phi_m > \phi_s$, forming therefore a Schottky barrier. This behavior is also observed for device ZGi (Fig, 5.31b) with the highest herbicide concentration but when polarized in forward (black line) only. The presence of the potential barrier dominating the device for positive bias can be identified

visually by the flat region between 1 and 2.41 V, attributed the ZnO-ITO interface. For negative bias, the curvy shape of the current indicates an ohmic behavior, which is also observed in the backwards direction for the positive voltages, from 0 to 4 V. This means that the Schottky diode is lost for the sweep backwards, while a high tunneling of charge seems to be occurring in reverse (negative bias) which leads to a quasi ohmic behavior with a hysteresis window of 1.7 V, larger than that for the plain ZnO NW devices. As the glyphosate concentration decreases, the width of the hysteresis window gets reduced, and the Schottky barrier fades away making the I-V characteristics of the devices more ohmic, as seen in Figure 5.31c. For the devices with the lowest herbicide concentration, i.e., the ones with GGG layers, the hysteresis decreases noticeably, and the devices are purely ohmic, Figure 5.31d. A similar behavior has been already observed for ZnO NW arrays passivated with insulating polymers, particularly with polystyrene [Bley, 2016]. It was demonstrated that layers with lower GGG concentrations lead to a more passivated surface than those with higher concentrations. It was observed that thicker layers are not suitable to passivate nanostructured surfaces since they may induce an accumulation of mobile charges and, therefore, increase the window of hysteresis current.

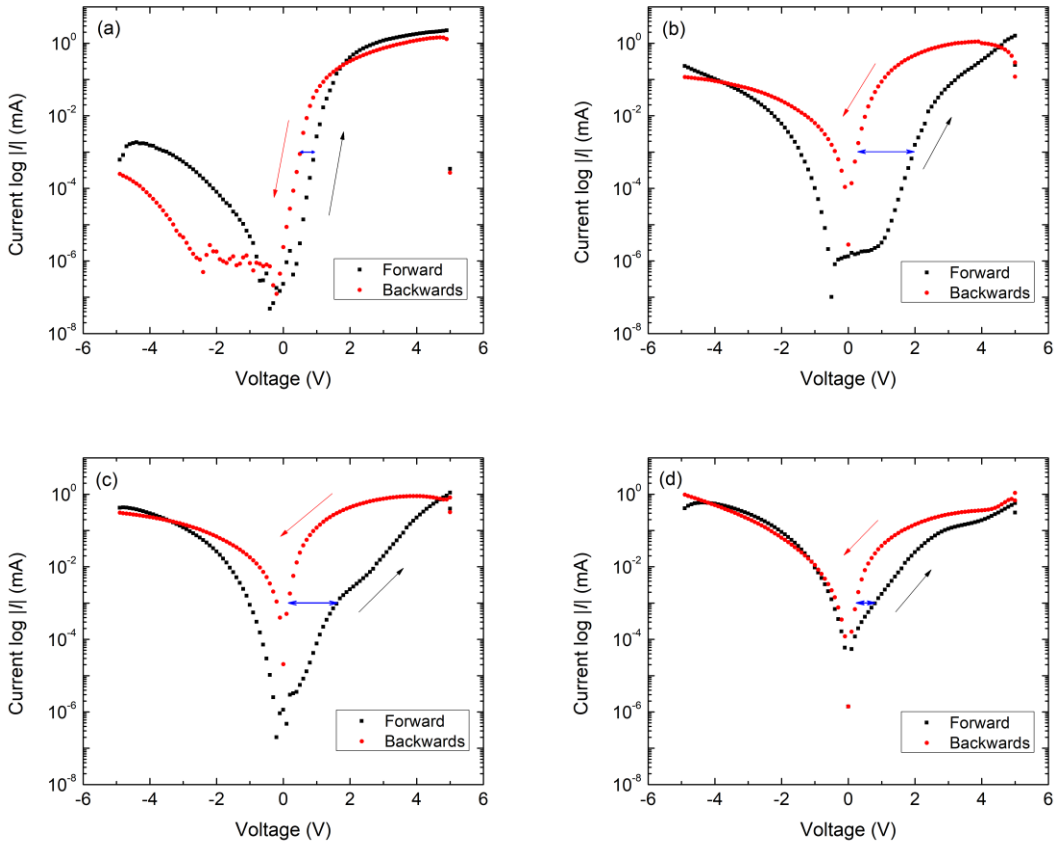

Figure 5.31. I-V characteristics of devices ZN (a), ZGi (b), ZGii (c), and ZGiii (d). The Blue arrows indicate the hysteresis effect.

Based on these previous observations, and considering that glyphosate showed insulating properties [Seemann, 2018], we could demonstrate experimentally with our present results that glyphosate indeed attaches on the ZnO surface as predicted theoretically by the MD simulations discussed in section 5.1. The I-V characteristics of the ZnO NWs show evidence of the glyphosate adsorption through a passivating effect of the nanostructures. Such a passivation is observed through the decrease of the hysteresis window size and the trend towards ohmic behavior of the ZnO-ITO interface, as similarly observed previously for polystyrene thin layers [Bley, 2016].

5.2.3 Structure III

5.2.3.1 SEM and EDX spectroscopy

Structure III was analyzed vertically, as depicted in Figure 5.19, through SEM to estimate the thickness of the ZnO layer.

The prefabricated transistor structure consists of 10 nm of Au and 270 nm of SiO_2. For the active layer, a ZnO seed layer with a concentration of 65 g/l was spin-coated under 600 rpms to obtain a 50 nm film as shown in the micrograph Figure 5.32.

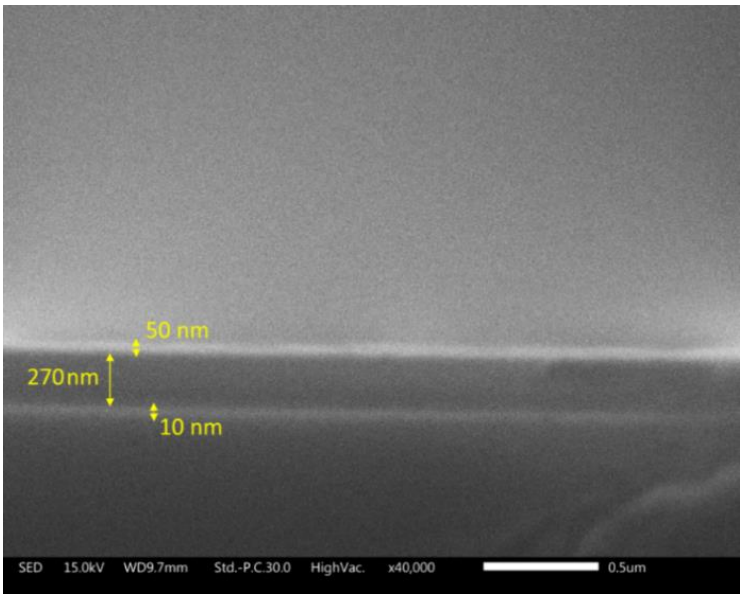

Figure 5.32. SEM measurement in SED mode of the Structure III device. The yellow size bars indicate the thickness of each layer. Au 10 nm, SiO_2 270 nm and ZnO 50 nm.

To verify the effect of glyphosate on Structure III, three drops of solution iii (1.01 wt%) were deposited by *spin coating* at 7.6 V (5000 rpms) for 45 s. Afterwards, the sample was annealed at 80 °C for 10 minutes to get rid of the water. Figure 5.33 shows the micrographs of the ZnO transistors without (a, b) and with GGG (c, d) . The latter micrographs are shown in SED mode, since secondary electrons are useful for the inspection of the sample´s surface topography. Here, the herbicide can be visualized as an opaque and non-homogeneous layer

covering the devices, including the electrodes and the conductive channel, Figure 5.33c and 5.33d.

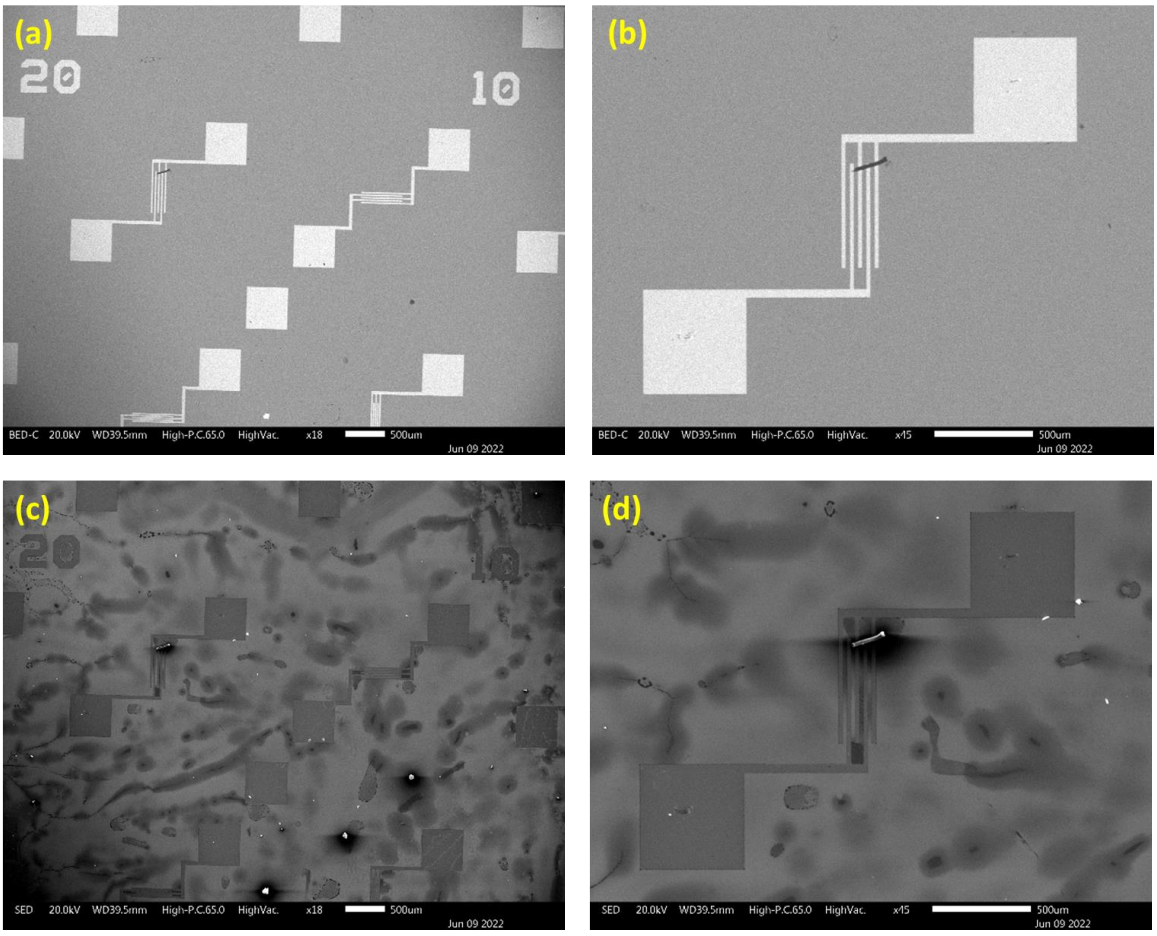

Figure 5.33. SEM measurements of devices in Structure III with 50 nm ZnO films as active layer: plain (a, b) and with glyphosate (c, d).

A zoom-in of the transistor channel is obtained by SEM (Figure 5.34) in order to analyze and determine the element composition of such a non-homogeneous layer. Figure 5.34a shows a SEM micrograph in BSE mode, necessary to subsequently carry out the composition analysis in EDX. Sections 1 and 3, the brightest and thus more conductive areas, correspond to the Au electrodes. Section 2, where the ZnO layer is deposited along the channel, looks less bright. Notice that the GGG deposited layer is not clearly seen by the micrograph due to its insulating properties.

The EDX analysis is performed considering the main elements of our system i.e., carbon, nitrogen, oxygen, silicon, phosphorus, gold and zinc. Figure 5.35b shows the color composition image generated, where each element is represented by different colors, Figures 5.35a-g.

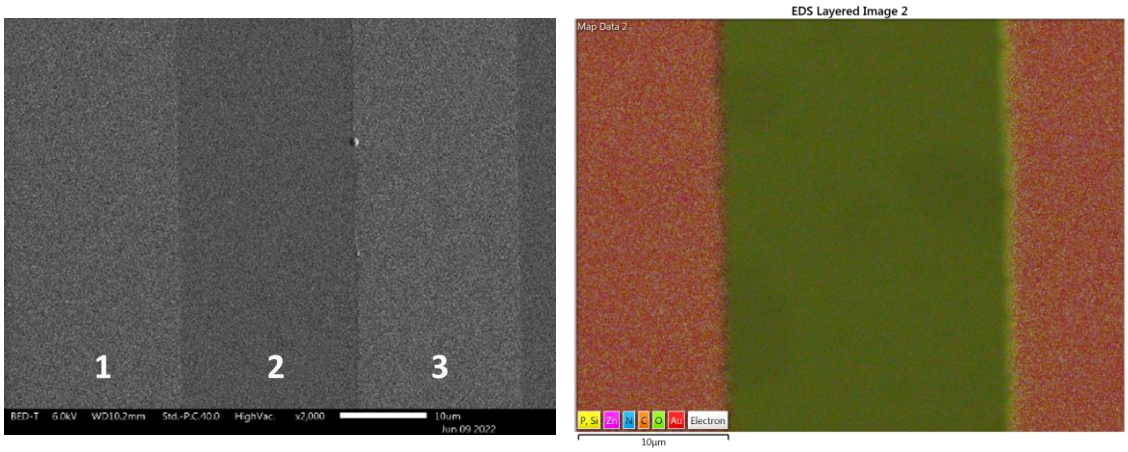

(a) (b)

Figure 5.34. SEM micrograph of Structure III in BED mode (a) and EDX mapping (b).

Gold is mainly observed in sections 1 and 3, Figure 5.36a. Conversely, silicon and oxygen in section 2, corresponding to the SiO_2/Si substrate (Figures 5.36b and c).

Zinc seems to be distributed uniformly on the three sections as shown in Figure 5.36d, confirming two important aspects: (i) The deposition technique covers the conductive channel with ZnO effectively and uniformly; and (ii) the electrodes are also coated in this process. The latter being an important consideration for the electrical analysis presented in the next section, 5.2.3.2.

Interestingly, carbon, nitrogen and particularly phosphorus were detected over the entire surface of the sample, confirming the presence of glyphosate, dispersed homogenously on the contacts and along the channel, Figures 5.36e-g.

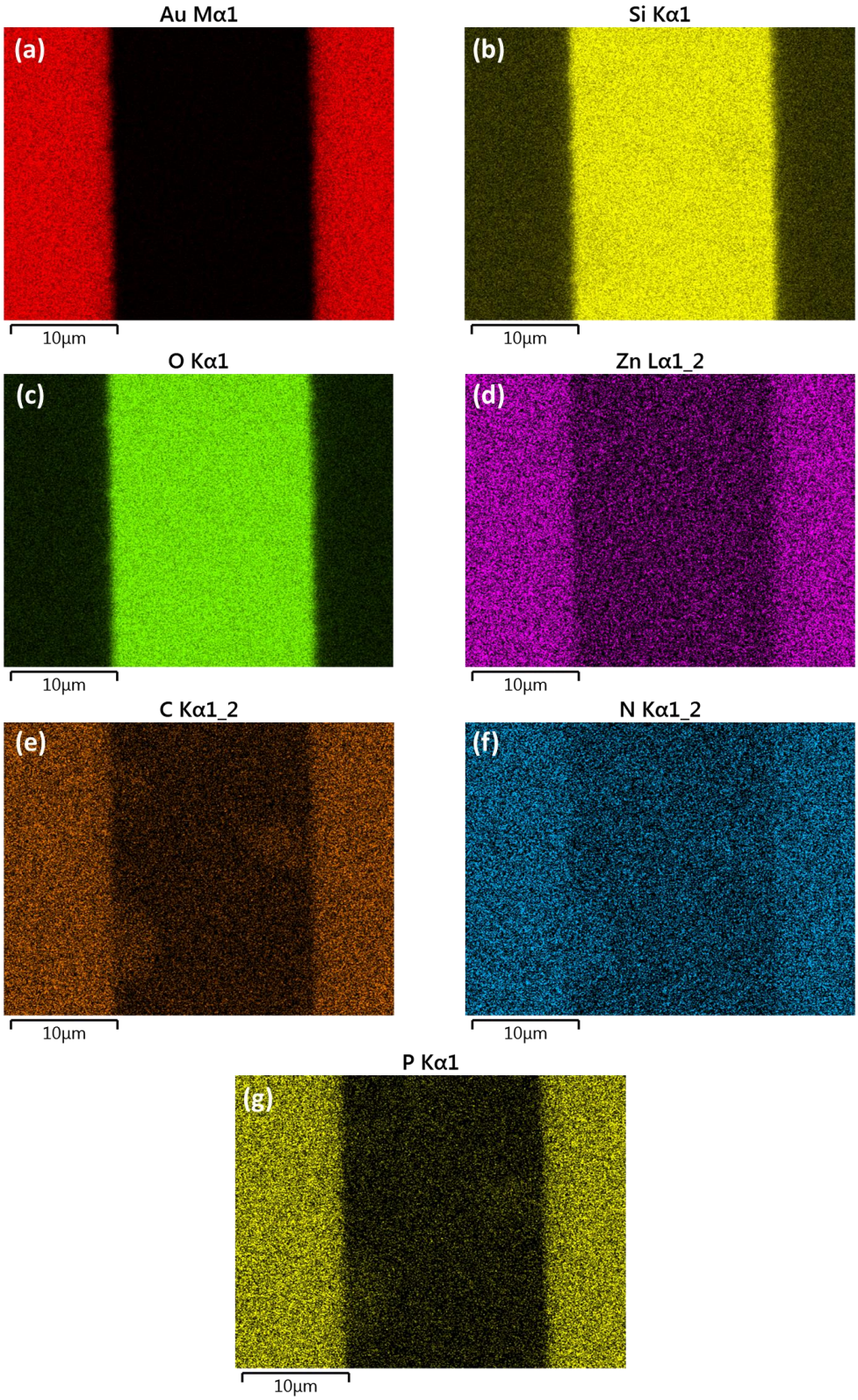

Figure 5.35. EDX analysis by color composition of gold (a), silicon (b), oxygen (c), zinc (d), carbon (e), nitrogen (f) and phosphorous (g).

5.2.3.2 I-V characteristics

To study the field effect of glyphosate on ZnO transistors, the electrical characteristics of Structure III were measured with and without GGG. The transistor output characteristics were measured as previously described in section 4.2.4.4.

For plain Structure III devices, i.e., ZnO TFTs without any glyphosate, the output characteristics are shown in Figure 5.36 where the field effect can be observed in the drain current (I_{DS}) under different gate bias (V_{GS}). Notice that such a field effect is ohmic, indicating that for the V_{DS} sweep range from 0 to 5 V only the linear condition of the devices can be visualized. Although the saturation regime of the transistors is not observed in this low-voltage range for V_{DS}, we decided to focus on these values for both testing purposes and the goal to implement our results in the development of a low-power sensor.

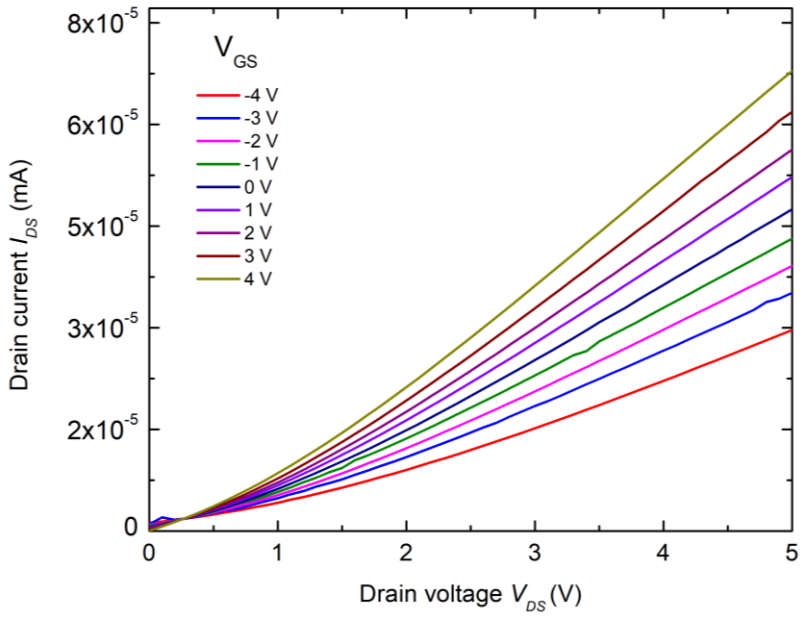

Figure 5.36. Output characteristics in linear regime of Structure III devices without glyphosate, under different gate bias V_{GS}.

To evaluate the effect of the herbicide on the ZnO transistors, the output characteristics of Structure III devices functionalized with GGG (Figure 5.37) are compared to the plain ones. A passivation effect can be clearly observed by the noticeably decrease of the current. For V_{GS} voltages from 0 to 4 V, I_{DS} decreases from 10^{-5} to 10^{-7} mA, as observed in the zoom-in inset of Figure 5.37.

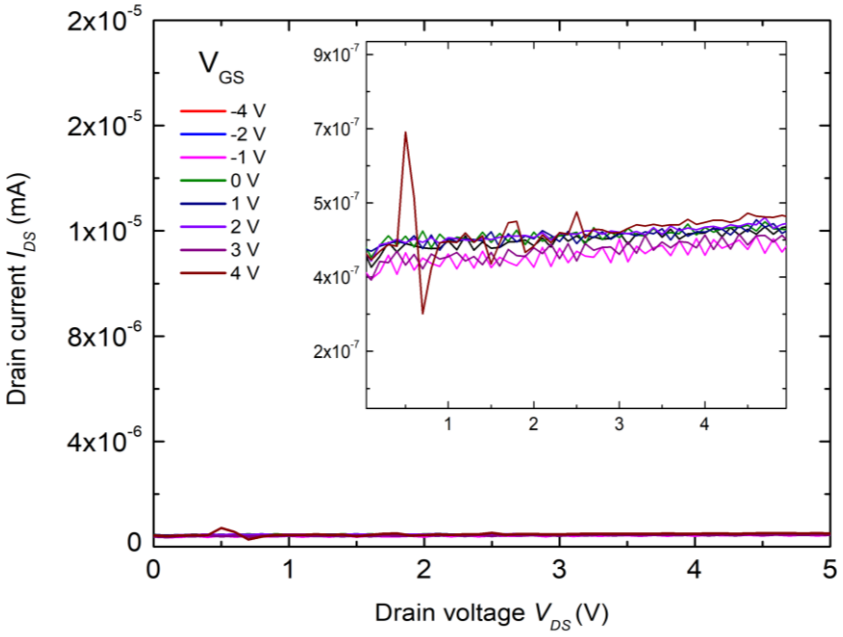

Figure 5.37. Output characteristics of structure III with 1.01 wt% of GGG deposited by *spin coating* at 7.6 V for 45. Annealing at 80 °C for 10 minutes.

In conclusion, it has been observed experimentally that glyphosate affects the field effect current for structure III. The interaction of GGG deposited as film modifies the conductivity of the transistors based on ZnO, annulling the field effect along the channel which is attributed to a passivation effect. Further investigation needs to be done in terms of response of the devices at higher V_{DS} values, selectivity and sensitivity, by quantifying the exact amount of glyphosate at which the channel can be passivated, and in this way, to propose a reliable device for its detection.

6 Conclusions and Outlook

In this work, ZnO is studied and evaluated as a potential semiconductor material for the development of a low-cost sensor for the in-situ detection of glyphosate. Specifically, by means of a field-effect mechanism through a thin film transistor structure.

For this purpose, the GGG/ZnO system is studied from both a theoretical and an experimental scope. To establish the theoretical foundation for the development of the device, the interaction between the herbicide and ZnO is studied through molecular dynamics simulations performed in GROMACS. Two different simulation protocols were used to analyze the system: type A and type B, corresponding to indirect and direct adsorption mechanisms, respectively. Based on our results, with a calculated energetic difference of 7.1 eV in between them, defined mainly by a lower value for the indirect procedure, we conclude that the type B protocol is the most favorable procedure.

To analyze the direct adsorption configurations of glyphosate on ZnO, the methodology to study the GGG/TiO_2 system (developed by the Hybrid Material Interfaces (HMI) group, University of Bremen) was implemented. Among the five different simulations performed in this work, the bidentated configuration consisting of both ends of the molecule with the phosphate and the carboxylic groups being attached onto the ZnO slab surface, showed to be the dominant adsorption mechanism for the GGG/ZnO system.

Our simulations led us to conclude that the energy interaction of GGG on ZnO is favorable. Nevertheless, we also found that water molecules strongly attach to the ZnO surface due to the hydroxyl group, therefore presenting a difficulty for GGG molecules to be adsorbed directly onto the semiconductor surface.

According to these theoretical findings, three different structures of hybrid organic-inorganic devices based on ZnO were fabricated at LAIDEA UNAM, ENES Morelia. Additionally, they were characterized and modeled, morphologically, optically, and electrically.

Respectively, the three structures consisted of:

I. ZnO layers, of approximately 60 nm, deposited on a glass substrate, and top Au contacts with a thickness of 30 nm deposited by thermal evaporation, which showed an ohmic behavior.

II. ZnO-NWs grown on ITO substrates by wet-chemical deposition, and subsequently coated with three different GGG concentrations, i.e., 1.50, 1.24 and 1.01 wt%, respectively. The samples were characterized by SEM, UV-VIS and I-V. SEM micrographs showed that 1.50 wt% and 1.24 wt% concentrations did not dissolve and instead formed grains of herbicide on the semiconductor surface. In contrast, the lowest concentration, i.e., 1.01 wt%, formed a non-homogeneous layer on the ZnO-NW arrays. UV-Vis absorbance spectra showed that the nanowires covered by 1.01 wt% concentrations increase their absorption in the 400 nm range onwards, suggesting a passivation-like effect due to the GGG coating layer. Moreover, the absorbance of the devices was analyzed on day one of GGG deposition and three days after, where a degradation effect is noticed, proportional to the passivating effect. This result is

consistent with reports in literature of possible degradation of GGG by ZnO. However, further investigation needs to be done to study and demonstrate this phenomenon.
Regarding the passivation effect of the ZnO surface by GGG, electrical characterization results support that the layer with 1.01 wt% GGG leads to a more passivated ZnO surface than those with higher concentrations. This could be observed by the reduction of the hysteresis current window, related to the decrease of mobile charge due to passivation of surface defects.

III. Prefabricated transistor structure of silicon, SiO_2 and Au electrodes. A 50 nm ZnO active layer was deposited on the transistor. I-V characteristics with and without the herbicide were measured. For plain ZnO devices, the transistor showed a field effect. After GGG deposition, a passivation effect is observed and confirmed through the decrease of the current by two orders of magnitude, i.e., from 10^{-5} to 10^{-7} mA, and the noticeable decrease/annulation of the field effect in the transistor.

Based on this, we can finally conclude that our experimental results on the attachment of GGG on ZnO surface are in good agreement with our theoretical findings. Therefore, in this work it has been demonstrated that the GGG/ZnO system is potential for the development of sensors for glyphosate detection. Further investigations should be carried out to test selectivity and sensitivity, i.e., analysis with lower GGG concentrations.

7 References

Alcántara-de la Cruz, R., Cruz-Hipolito, H. E., Domínguez-Valenzuela, J. A., & De Prado, R. (2021). Glyphosate ban in Mexico: potential impacts on agriculture and weed management. *Pest Management Science*, 77(9), 3820-3831.

Asano, K., Sasaki, Y., Minamiki, T., & Minami, T. (2020). Sensitive Detection of Glyphosate by a Water-Gated Organic Transistor. *ECS Transactions*, 98(12), 41.

Balzaretti, F. (2021). Adsorption and degradation of eater pollutants on TiO_2 [Doctoral thesis, University of Bremen] https://media.suub.uni-bremen.de/handle/elib/5872

Balzaretti, F., von Einem, M., Gerhards, L., Dononelli, W., Stauch, T., Klüner, T., & Köppen, S. (2021). Charge-Transfer Promoted Fixation of Glyphosate on TiO_2-a Multiscale Approach. *ChemRxiv*. Cambridge: Cambridge Open Engage; 2021.

Bao, Q., Liu, X., Xia, Y., Gao, F., Kauffmann, L. D., Margeat, O., ... & Fahlman, M. (2014). Effects of ultraviolet soaking on surface electronic structures of solution processed ZnO nanoparticle films in polymer solar cells. *Journal of Materials Chemistry A*, 2(41), 17676-17682.

Bekker, H., Berendsen, H. J. C., Dijkstra, E. J., Achterop, S., Vondrumen, R., VANDERSPOEL, D., ... & Renardus, M. K. R. (1993). Gromacs-a parallel computer for molecular-dynamics simulations. *In 4th International Conference on Computational Physics* (PC 92) (pp. 252-256). World Scientific Publishing.

Berendsen, H. J., Postma, J. V., Van Gunsteren, W. F., DiNola, A. R. H. J., & Haak, J. R. (1984). Molecular dynamics with coupling to an external bath. *The Journal of chemical physics*, 81(8), 3684-3690.

Bley, S., Rückmann, M., Castro-Carranza, A., Meierhofer, F., Mädler, L., Voss, T., & Gutowski, J. (2016). Structural and optical characterization of hybrid ZnO/polymer core-shell nanowires fabricated by oxidative chemical vapour deposition. *physica status solidi* (c), 13(7-9), 614-617.

Britannica, The Editors of Encyclopaedia. "energy". Encyclopedia Britannica, 18 Oct. 2022, https://www.britannica.com/science/energy. Accessed 28 October 2022.

Bueren-Calabuig, J. A., Pierdominici-Sottile, G., & Roitberg, A. E. (2014). Unraveling the Differences of the Hydrolytic Activity of Trypanosoma cruzi trans-Sialidase and Trypanosoma rangeli Sialidase: A Quantum Mechanics–Molecular Mechanics Modeling Study. *The Journal of Physical Chemistry B*, 118(22), 5807-5816.

Bussi, G., Donadio, D., & Parrinello, M. (2007). Canonical sampling through velocity rescaling. *The Journal of chemical physics*, 126(1), 014101.

Caetano, M. S., Ramalho, T. C., Botrel, D. F., da Cunha, E. F., & de Mello, W. C. (2012). Understanding the inactivation process of organophosphorus herbicides: A DFT study of glyphosate metallic complexes with Zn^{2+}, Ca^{2+}, Mg^{2+}, Cu^{2+}, Co^{2+}, Fe^{2+}, Cr^{2+}, and Al^{2+}. *International Journal of Quantum Chemistry*, 112(15), 2752-2762.

Carvalho, F. P. (2017). Mining industry and sustainable development: time for change. *Food and Energy security*, 6(2), 61-77.

Castro, A (2021). Estudio de los mecanismos de transporte y recombinación de carga en celdas solares orgánicas nanoestructuradas [Tesis de licenciatura, Universidad

Nacional Autónoma de México, Escuela Nacional de Estudios Superiores (Unidad Morelia)] http://132.248.9.195/ptd2021/agosto/0813983/Index.html

Castro-Carranza, A. (2013). UMEM-based capacitance model for organic field effect transistors: Development and implementation [Doctoral thesis. Universitat Rovira I Virgili] https://www.tesisenred.net/handle/10803/111164

Czyżowska, A., Barbasz, A., Rudolphi-Szydło, E., & Dyba, B. (2022). The cell membrane as the barrier in the defense against nanoxenobiotics: Zinc oxide nanoparticles interactions with native and model membrane of melanoma cells. *Journal of Applied Toxicology*, 42(2), 334-341.

da Silva, E. R., Segato, T. P., Coltro, W. K., Lima, R. S., Carrilho, E., & Mazo, L. H. (2013). Determination of glyphosate and AMPA on polyester-toner electrophoresis microchip with contactless conductivity detection. *Electrophoresis*, 34(14), 2107-2111.

Dallegrave, E., Mantese, F. D., Coelho, R. S., Pereira, J. D., Dalsenter, P. R., & Langeloh, A. (2003). The teratogenic potential of the herbicide glyphosate-Roundup® in Wistar rats. *Toxicology letters*, 142(1-2), 45-52.

Dhamu, V. N., Poudyal, D. C., Muthukumar, S., & Prasad, S. (2021). A Highly Sensitive Electrochemical Sensor System to Detect and Distinguish between Glyphosate and Glufosinate. *Journal of The Electrochemical Society*, 168(5), 057531.

do Valle, A. L., Silva, A. C. A., Melo, F. C., Fernandes, G. D. L., de Oliveira, G. S., Dantas, N. O., ... & Goulart Filho, L. R. (2021). Glyphosate: ZnO Nanocrystal Interaction Controlled by pH Changes. *IEEE Sensors Journal*, 21(18), 19731-19739.

Duke, S. O., & Powles, S. B. (2008). Glyphosate: a once-in-a-century herbicide. *Pest Management Science: formerly Pesticide Science*, 64(4), 319-325.

Dweydari, A. W., & Mee, C. H. B. (1975). Work function measurements on (100) and (110) surfaces of silver. *physica status solidi* (a), 27(1), 223-230.

Ghosh, S., Goudar, V. S., Padmalekha, K. G., Bhat, S. V., Indi, S. S., & Vasan, H. N. (2012). ZnO/Ag nanohybrid: synthesis, characterization, synergistic antibacterial activity and its mechanism. *Rsc Advances*, 2(3), 930-940.

González, M. A. (2011). Force fields and molecular dynamics simulations. *École thématique de la Société Française de la Neutronique*, 12, 169-200.

Greim, H., Saltmiras, D., Mostert, V., & Strupp, C. (2015). Evaluation of carcinogenic potential of the herbicide glyphosate, drawing on tumor incidence data from fourteen chronic/carcinogenicity rodent studies. *Critical reviews in toxicology*, 45(3), 185-208.

Große Holthaus, S., Köppen, S., Frauenheim, T., & Colombi Ciacchi, L. (2012). Atomistic Simulations of the ZnO $(12\bar{1}0)$/Water Interface: A Comparison between First-Principles, Tight-Binding, and Empirical Methods. *Journal of Chemical Theory and Computation*, 8(11), 4517-4526.

Guo, M., Diao, P., & Cai, S. (2005). Hydrothermal growth of well-aligned ZnO nanorod arrays: Dependence of morphology and alignment ordering upon preparing conditions. *Journal of solid state Chemistry*, 178(6), 1864-1873.

Guttenberger, S., & Bär, K. (2016). Gebraut nach dem deutschen Reinheitsgebot. Hopfen und Malz verloren? Glyphosat-Rückstände im deutschen Bier [Brewed according to the German Purity Law. Hops and malt lost? Glyphosate residues in German beer]. Umweltinstitut München [Munich Environmental Institute].

Habekost, A. (2017). Rapid and sensitive spectroelectrochemical and electrochemical detection of glyphosate and AMPA with screen-printed electrodes. *Talanta*, 162, 583-588.

Henkelman, G., & Jónsson, H. (2000). Improved tangent estimate in the nudged elastic band method for finding minimum energy paths and saddle points. *The Journal of chemical physics*, 113(22), 9978-9985.

Hsueh, T. J., Hsu, C. L., Chang, S. J., Lin, Y. R., Chang, S. P., Chiou, Y. Z., ... & Chen, I. C. (2007). Crabwise ZnO nanowire UV photodetector prepared on ZnO: Ga/glass template. *IEEE transactions on nanotechnology*, 6(6), 595-600.

Hübert, T., Boon-Brett, L., Black, G., & Banach, U. (2011). Hydrogen sensors–a review. *Sensors and Actuators B: Chemical*, 157(2), 329-352.

Hübert, T., Boon-Brett, L., Black, G., & Banach, U. (2011). Hydrogen sensors–a review. *Sensors and Actuators B: Chemical*, 157(2), 329-352.

Humphrey, W., Dalke, A., & Schulten, K. (1996). VMD: visual molecular dynamics. *Journal of molecular graphics*, 14(1), 33-38.

International Agency for Research on Cancer. Agents classified by the IARC monographs, volumes 112-10. Available from: https://monographs.iarc.who.int/wp-content/uploads/2018/06/mono112-10.pdf

Janotti, A., & Van de Walle, C. G. (2009). Fundamentals of zinc oxide as a semiconductor. *Reports on progress in physics*, 72(12), 126501.

Jo, S., Kim, T., Iyer, V. G., & Im, W. (2008). CHARMM-GUI: a web-based graphical user interface for CHARMM. *Journal of computational chemistry*, 29(11), 1859-1865.

Kim, S., Chen, J., Cheng, T., Gindulyte, A., He, J., He, S., Li, Q., Shoemaker, B. A., Thiessen, P. A., Yu, B., Zaslavsky, L., Zhang, J., & Bolton, E. E. (2019). PubChem in 2021: new data content and improved web interfaces. *Nucleic Acids Res*., 49(D1), D1388–D1395.

Kıvrak, S., Özer, T., Oğuz, Y., & Erken, E. B. (2020). Battery management system implementation with the passive control method using MOSFET as a load. *Measurement and Control*, 53(1-2), 205-213.

Klingshirn, C. (2007). ZnO: From basics towards applications. *physica status solidi* (b), 244(9), 3027-3073.

Le Gall, J., Vasilijević, S., Battaglini, N., Mattana, G., Noël, V., Brayner, R., & Piro, B. (2021). Algae-functionalized hydrogel-gated organic field-effect transistor. Application to the detection of herbicides. *Electrochimica Acta*, 372, 137881.

Li, Z., Zhong, W., Li, X., Zeng, H., Wang, G., Wang, W., ... & Zhang, Y. (2013). Strong room-temperature ferromagnetism of pure ZnO nanostructure arrays via colloidal template. *Journal of Materials Chemistry C*, 1(41), 6807-6812.

Liao, Z. M., Liu, K. J., Zhang, J. M., Xu, J., & Yu, D. P. (2007). Effect of surface states on electron transport in individual ZnO nanowires. *Physics Letters A*, 367(3), 207-210.

Manzo, J.A (2021). Síntesis y modelado de nanopilares de óxido de zinc para su aplicación optimizada en celdas solares y sensores de bajo costo [Tesis de licenciatura, Universidad Nacional Autónoma de México, Escuela Nacional de Estudios Superiores (Unidad Morelia)] http://132.248.9.195/ptd2022/agosto/0828938/Index.html

Mazouz, Z., Rahali, S., Fourati, N., Zerrouki, C., Aloui, N., Seydou, M., ... & Kalfat, R. (2017). Highly Selective Polypyrrole MIP-Based Gravimetric and Electrochemical Sensors for Picomolar Detection of Glyphosate. *Sensors*, 17, 2586.

Michaelis, M., Delle Piane, M., Rothenstein, D., Perry, C. C., & Colombi Ciacchi, L. (2021). Lessons from a Challenging System: Accurate Adsorption Free Energies at the Amino Acid/ZnO Interface. *Journal of Chemical Theory and Computation*, 17(7), 4420-4434.

Minami, T., Tang, W., & Asano, K. (2021). Chemical sensing based on water-gated polythiophene thin-film transistors. *Polymer Journal*, 53(12), 1315-1323.

Mink, P. J., Mandel, J. S., Sceurman, B. K., & Lundin, J. I. (2012). Epidemiologic studies of glyphosate and cancer: a review. *Regulatory Toxicology and Pharmacology*, 63(3), 440-452.

Monticelli, L., & Tieleman, D. P. (2013). Force fields for classical molecular dynamics. *Biomolecular simulations*, 197-213.

Nasser, R., Song, J. M., & Elhouichet, H. (2021). Epitaxial growth and properties study of p-type doped ZnO: Sb by PLD. *Superlattices and Microstructures*, 155, 106908.

Neamen, D. A. (2012). Semiconductor physics and devices: Basic principles (4th ed.). McGraw-Hill.

Nosé, S. (1984). A molecular dynamics method for simulations in the canonical ensemble. *Molecular physics*, 52(2), 255-268.

Ofuonye, B., Lee, J., Yan, M., Sun, C., Zuo, J. M., & Adesida, I. (2014). Electrical and microstructural properties of thermally annealed Ni/Au and Ni/Pt/Au Schottky contacts on AlGaN/GaN heterostructures. *Semiconductor science and technology*, 29(9), 095005.

Páez, M. R., Ochoa-Muñoz, Y., & Rodriguez-Páez, J. E. (2019). Efficient removal of a glyphosate-based herbicide from water using ZnO nanoparticles (ZnO-NPs). *Biocatalysis and Agricultural Biotechnology*, 22, 101434.

Park, W. I., An, S. J., Yi, G. C., & Jang, H. M. (2001). Metal-organic vapor phase epitaxial growth of high-quality ZnO films on Al2O3 (00· 1*). Journal of Materials Research*, 16(5), 1358-1362.

Pudukudy, M., & Yaakob, Z. (2015). Facile synthesis of quasi spherical ZnO nanoparticles with excellent photocatalytic activity. *Journal of Cluster Science*, 26(4), 1187-1201.

Rendón-von Osten, J., & Dzul-Caamal, R. (2017). Glyphosate residues in groundwater, drinking water and urine of subsistence farmers from intensive agriculture localities: a survey in Hopelchén, Campeche, Mexico. *International journal of environmental research and public health*, 14(6), 595.

Roustan, A., Aye, M., De Meo, M., & Di Giorgio, C. (2014). Genotoxicity of mixtures of glyphosate and atrazine and their environmental transformation products before and after photoactivation. *Chemosphere*, 108, 93-100.

Samson, E., Marchand, J., & Snyder, K. A. (2003). Calculation of ionic diffusion coefficients on the basis of migration test results. *Materials and structures*, 36(3), 156-165.

Sanchez Martín, M. J., Villa, M. V., & Sanchez-Camazano, M. (1999). Glyphosate-hydrotalcite interaction as influenced by pH. *Clays and Clay Minerals*, 47(6), 777-783.

Sasaki, Y., Asano, K., Minamiki, T., Zhang, Z., Takizawa, S. Y., Kubota, R., & Minami, T. (2020). A Water-Gated Organic Thin-Film Transistor for Glyphosate Detection: A Comparative Study with Fluorescence Sensing. *Chemistry–A European Journal*, 26(64), 14525-14529.

Seemann, W. (2018). A fundamental characterization of glyphosate for sensing applications [Master thesis, University of Bremen]

Sellare, J., Meemken, E. M., & Qaim, M. (2020). Fairtrade, agrochemical input use, and effects on human health and the environment. *Ecological economics*, 176, 106718.

Sharma, A., Franklin, J. B., Singh, B., Andersson, G. G., & Lewis, D. A. (2015). Electronic and chemical properties of ZnO in inverted organic photovoltaic devices. *Organic Electronics*, 24, 131-136.

Sikorska, C., & Gaston, N. (2020). Modified Lennard-Jones potentials for nanoscale atoms. *Journal of Computational Chemistry*, 41(22), 1985-2000.

Silva, J. P., Vieira, E. M., Gwozdz, K., Kaim, A., Goncalves, L. M., MacManus-Driscoll, J. L., ... & Pereira, M. (2021). High-performance self-powered photodetectors achieved through the pyro-phototronic effect in Si/SnOx/ZnO heterojunctions. *Nano Energy*, 89, 106347.

Stueker, O., Ortega, V. A., Goss, G. G., & Stepanova, M. (2014). Understanding interactions of functionalized nanoparticles with proteins: a case study on lactate dehydrogenase. *Small*, 10(10), 2006-2021.

Sujinnapram, S., Nilphai, S., Moungsrijun, S., Krobthong, S., & Wongrerkdee, S. (2021). Clustered zno nanoparticles synthesized via precipitation for photocatalytic degradation of methyl orange and glyphosate. *Digest Journal of Nanomaterials and Biostructures*, 16(1), 317-329.

Sun, J. H., Dong, S. Y., Feng, J. L., Yin, X. J., & Zhao, X. C. (2011). Enhanced sunlight photocatalytic performance of Sn-doped ZnO for Methylene Blue degradation. *Journal of Molecular Catalysis A: Chemical*, 335(1-2), 145-150.

Tada, H., Teranishi, K., Inubushi, Y. I., & Ito, S. (2000). Ag nanocluster loading effect on TiO2 photocatalytic reduction of bis (2-dipyridyl) disulfide to 2-mercaptopyridine by H2O. *Langmuir*, 16(7), 3304-3309.

Tesson, S., Salanne, M., Rotenberg, B., Tazi, S., & Marry, V. (2016). Classical polarizable force field for clays: Pyrophyllite and talc. *The Journal of Physical Chemistry C*, 120(7), 3749-3758.

PumMa website. http://cbio.bmt.tue.nl/pumma/index.php.

Torres-Rivero, K., Bastos-Arrieta, J., Fiol, N., & Florido, A. (2021). Metal and metal oxide nanoparticles: An integrated perspective of the green synthesis methods by natural products and waste valorization: applications and challenges. *Comprehensive Analytical Chemistry*, 94, 433-469.

Valle, A. L., Mello, F. C. C., Alves-Balvedi, R. P., Rodrigues, L. P., & Goulart, L. R. (2019). Glyphosate detection: methods, needs and challenges. *Environmental chemistry letters*, 17(1), 291-317.

Vidal, E., Negro, A., Cassano, A., & Zalazar, C. (2015). Simplified reaction kinetics, models and experiments for glyphosate degradation in water by the UV/H2O2 process. *Photochemical & Photobiological Sciences*, 14(2), 366-377.

Wang, X., Zhou, J., Song, J., Liu, J., Xu, N., & Wang, Z. L. (2006). Piezoelectric field effect transistor and nanoforce sensor based on a single ZnO nanowire. *Nano letters*, 6(12), 2768-2772.

Woodburn, A. T. (2000). Glyphosate: production, pricing and use worldwide. *Pest Management Science: formerly Pesticide Science*, 56(4), 309-312.

Yu, J., Lin, J., & Li, J. (2021). A photoelectrochemical sensor based on an acetylcholinesterase-CdS/ZnO-modified extended-gate field-effect transistor for glyphosate detection. *Analyst*, 146(14), 4595-4604.

Yu, X., Marks, T. J., & Facchetti, A. (2016). Metal oxides for optoelectronic applications. *Nature materials*, 15(4), 383-396.

Zambrano-Intriago, L. A., Amorim, C. G., Rodríguez-Díaz, J. M., Araújo, A. N., & Montenegro, M. C. (2021). Challenges in the design of electrochemical sensor for glyphosate-based on new materials and biological recognition. *Science of the Total Environment*, 793, 148496.

Zhao, M., Chen, Y., Wang, K., Zhang, Z., Streit, J. K., Fagan, J. A., ... & Sun, W. (2020). DNA-directed nanofabrication of high-performance carbon nanotube field-effect transistors. *Science*, 368(6493), 878-881

Zhou, W., & Wang, Z. L. (Eds.). (2007). Scanning microscopy for nanotechnology: techniques and applications. *Springer science & business media*.